

# Tools for the measurement of stress and strain fields in soft tissue

**Citation for published version (APA):**

Peters, G. W. M. (1987). *Tools for the measurement of stress and strain fields in soft tissue: application to the elbow joint*. [Phd Thesis 4 Research NOT TU/e / Graduation NOT TU/e], Maastricht University]. Rijksuniversiteit Limburg. [https://cris.maastrichtuniversity.nl/portal/en/publications/tools-for-the-measurement-of-stress-and-strain-fields-in-soft-tissue--application-to-the-elbow-joint\(fa4ae928-94e8-48bc-8da3-0f08f8e014f1\).html](https://cris.maastrichtuniversity.nl/portal/en/publications/tools-for-the-measurement-of-stress-and-strain-fields-in-soft-tissue--application-to-the-elbow-joint(fa4ae928-94e8-48bc-8da3-0f08f8e014f1).html)

**Document status and date:**

Published: 20/11/1987

**Document Version:**

Publisher's PDF, also known as Version of Record (includes final page, issue and volume numbers)

**Please check the document version of this publication:**

- A submitted manuscript is the version of the article upon submission and before peer-review. There can be important differences between the submitted version and the official published version of record. People interested in the research are advised to contact the author for the final version of the publication, or visit the DOI to the publisher's website.
- The final author version and the galley proof are versions of the publication after peer review.
- The final published version features the final layout of the paper including the volume, issue and page numbers.

[Link to publication](#)

**General rights**

Copyright and moral rights for the publications made accessible in the public portal are retained by the authors and/or other copyright owners and it is a condition of accessing publications that users recognise and abide by the legal requirements associated with these rights.

- Users may download and print one copy of any publication from the public portal for the purpose of private study or research.
- You may not further distribute the material or use it for any profit-making activity or commercial gain
- You may freely distribute the URL identifying the publication in the public portal.

If the publication is distributed under the terms of Article 25fa of the Dutch Copyright Act, indicated by the "Taverne" license above, please follow below link for the End User Agreement:

[www.tue.nl/taverne](http://www.tue.nl/taverne)

**Take down policy**

If you believe that this document breaches copyright please contact us at:

[openaccess@tue.nl](mailto:openaccess@tue.nl)

providing details and we will investigate your claim.

**TOOLS FOR THE MEASUREMENT OF  
STRESS AND STRAIN FIELDS  
IN SOFT TISSUE**

application to the elbow joint

Gerrit Peters

**TOOLS FOR THE MEASUREMENT OF  
STRESS AND STRAIN FIELDS  
IN SOFT TISSUE**

application to the elbow joint

**PROEFSCHRIFT**

ter verkrijging van de graad van doctor  
aan de Rijksuniversiteit Limburg te Maastricht,  
op gezag van de Rector Magnificus, Prof. Dr. F.I.M. Bonke,  
volgens het besluit van het College van Dekanen,  
in het openbaar te verdedigen op vrijdag 20 november 1987  
om 14.00 uur

door

**GERARDUS WILHELMUS MARIA PETERS**

geboren op 3 maart 1953 te Veghel

Promotores : Prof. Dr. Ir. J. D. Janssen  
Prof. Dr. J. Drukker

Co-promotor : Dr. Ir. G. W. J. Oomens

Referenten : Prof. Dr. A. Huson  
Dr. Ir. T. Arts

Dit onderzoek werd uitgevoerd in het kader van een  
samenwerkingsverband tussen de Rijksuniversiteit Limburg te  
Maastricht en de Technische Universiteit Eindhoven.

Typewerk : Lia Neervoort

## CONTENTS

Abstract

Notation

### 1 INTRODUCTION

- 1.1 Problem definition
- 1.2 Anatomy of the collagenous connective tissue structures on the lateral side of the elbow joint
- 1.3 Purpose and scope of the present study

### 2 FORCE MEASUREMENT

- 2.1 Introduction
- 2.2 Redesign of the buckle transducer
- 2.3 A mechanical model of the buckle transducer
- 2.4 Test measurements

### 3 STRAIN MEASUREMENT

- 3.1 Introduction
- 3.2 Reconstruction of spatial marker coordinates
  - 3.2.1 Theory of the central projection
  - 3.2.2 A theoretical model for the reconstruction of spatial marker coordinates
- 3.3 Strain estimation from measured marker coordinates
  - 3.3.1 Estimation of deformation quantities
  - 3.3.2 Strain distributions on curved surfaces
- 3.4 Marker identification
  - 3.4.1 Introduction
  - 3.4.2 Marker identification for different pictures
  - 3.4.3 Marker identification for different states of the deformation
- 3.5 Error analysis
  - 3.5.1 Calibration and correction of systematic errors
  - 3.5.2 Statistical properties of the deformation gradient tensor  $F$  and the Green-Lagrange strain tensor  $E$

### 4 STRAIN DISTRIBUTION MEASUREMENT: THE EXPERIMENTAL SET-UP

- 4.1 Introduction
- 4.2 The experimental set-up
  - 4.2.1 The optical system
  - 4.2.2 Data processing
  - 4.2.3 Aspects of accuracy
- 4.3 Test measurements

## 5 LOAD TRANSMISSION BY COLLAGENOUS CONNECTIVE TISSUES

5.1 Introduction

5.2 General aspects concerning the experimental procedure

5.3 Results

5.3.1 Anisotropy

5.3.2 Inhomogeneity

5.3.3 Biaxial testing

5.3.4 In situ strain measurements

## 6. SUMMARY AND CONCLUSIONS

References

Appendices A-I

Samenvatting

curriculum vitae

Dankwoord

---

ABSTRACT

---

In order to gain insight into the mechanical behaviour of soft tissues by means of experimental research, tools have been developed for stress and strain field measurement which allow to take into account inhomogeneous properties. These tools have been applied to the collagenous connective tissue structure of the lateral side of the elbow joint. This structure was chosen as object of investigation because an extensive anatomical description was available.

For stress measurement a redesign of the buckle transducer was applied. This redesign implies improvements with respect to size and shape, installation conditions and time dependence of the output signal.

For strain field measurement an image recording system is used. The coordinates of markers, mounted on the object under investigation, in different deformation states are reconstructed from the captured images. Next, the coordinates of a group of markers, in the vicinity of each marker are used to determine estimates for the components of the deformation tensor  $F$  in each material point, defined by the centroid of a marker. With these estimates, components of the Green-Lagrange strain tensor  $E$  are calculated. Mathematical models which describe the different stages of the measurement are shown to be essential for design for accuracy and for justified interpretation of the results. Furthermore, attention is paid to the measurement of strain fields on curved surfaces and on the identification of markers by different object configurations.

Different types of experiments have been performed on tissue samples. One experiment was performed on the connective tissue structure in situ. Rather than the establishment of material parameters or quantitative structural properties, the experiments were focused on investigating which phenomena and which parameters should be considered important. It is demonstrated that the mechanical behaviour of the tissue is very complex. With the involved parameters, thickness, collagen fibre texture and boundary conditions, the measured phenomena can only partially be explained. For further research more detailed information on fibre texture and more certainty on the thickness measuring method are of primary interest. Moreover, for a quantitative description of the mechanical behaviour or for the determination of material parameters the interaction between experiments and numerical simulation of these experiments is essential.





## Notation

$a$	scalar
$\vec{a}$	vector
$  \vec{a}  $	length of $\vec{a}$
$\vec{a} \cdot \vec{a}$	dot product of two vectors
$\vec{a} * \vec{a}$	cross product of two vectors
$\vec{a} \vec{a}$	dyadic product of two vectors
$A$	second-order tensor
$A^c$	conjugate of $A$
$A^{-1}$	inverse of $A$
$A \cdot \vec{a}$	dot product of a second-order tensor and a vector
$A \cdot B$	dot product of two second-order tensors
$A : B$	double dot product of two second-order tensors
$A B$	tensor product of two second-order tensors
$\text{tr}(A)$	trace of $A$
$\det(A)$	determinant of $A$
${}^4A$	fourth-order tensor
$\underline{a}$	column of scalars
$\underline{a}^T$	transposed column
$\underline{A}$	matrix
$\underline{A}^T$	transposed matrix
$\vec{a}, \bar{a}, \bar{A}, \bar{\bar{A}}$	stochastic variables
$\hat{a}, \hat{\bar{a}}, \hat{\bar{A}}, \hat{\bar{\bar{A}}}$	estimates
$E(\vec{a})$	expected value
$\bar{a}$	mean



---

## 1. INTRODUCTION

---

### 1.1 PROBLEM DEFINITION

The present thesis deals with an experimental investigation of the mechanical behaviour of 3-dimensional collagenous connective tissue structures, in particular the structures which provide for the transmission to bone of tensile forces, developed by the contractile elements of muscles.

This work has been performed in close cooperation between the department of Anatomy and Embryology of the University of Limburg and the department of Engineering Fundamentals of the Eindhoven University of Technology. It is part of an extensive research program aiming at a contribution to the understanding of the functional morphology of the human locomotion system. The experimental methods described in this thesis have been applied to tissues from the regio cubitalis, but can also be used for other tissues.

The anatomical description of collagenous connective tissue structures around the humero-radial joint of the elbow (Van Mameren and Drukker, 1984) has led to new insight into their mechanical function and their classification. This description differs from the concept of soft tissue structures around the humero-radial joint as given in classical anatomical text books (Morris and Anson, 1966, Warwick and Williams, 1973, Drukker and Jansen, 1975). These distinguish an active (the muscles) and a passive force transmitting system (the ligaments) parallel to each other. However, from the alternative description it is shown that the connective tissue usually forms an integral part of complex spatial structures to which the muscles attach and thus lying in series with the muscles. The force transmission from the contractile elements of the muscles to bone appears to be a complicated process therefore. The main function of these structures appears to be the transmission of the muscle forces to bones. Therefore, it is felt that increasing understanding the mechanical behaviour of these intermediate structures is of primary importance. As an extensive anatomical description of collagenous connective tissue structures around the lateral side of the humero-radial joint is available (Van Mameren, 1984), this structure was chosen as subject of investigation. Before a more accurate definition of purpose and scope of this study is given in section 1.3, the anatomy of this structure is described in the next section.

1.2 ANATOMY OF THE COLLAGENOUS CONNECTIVE TISSUE STRUCTURE ON THE LATERAL SIDE OF THE ELBOW JOINT

The elbow joint is a synovial joint in which the radius and ulna articulate with the humerus (fig. 1.2.1). The joint cavity is continuous with that of the proximal radio-ulnar joint.

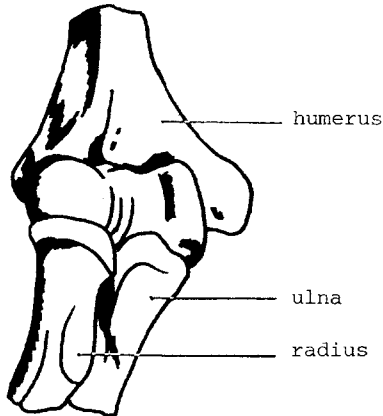


Fig. 1.2.1 Articulation of humerus, radius and ulna.

In classical text-books of anatomy, the soft tissue structures around the elbow joint are usually described in terms of muscles and ligaments (skin, subcutis, nerves, arteries and veins are not concerned with regard to the mechanical behaviour of the elbow joint; they will not be discussed here). The muscles that cross the elbow joint in the extensor region are depicted in fig. 1.2.2 where also the names of these muscles are given. The ligaments, as defined in the classical way, are depicted and named in fig. 1.2.3. This description starts from the principle of two separate force transmitting structures parallel to each other. One is called an active force transmitting structure (the muscles), the other a passive force transmitting structure (the ligaments).

To gain insight into the 3-dimensional structures of collagenous and muscular tissue in the lateral cubital region, skin and subcutaneous tissue should be removed and connections formed by connective tissue strands between fascia and skin sharply cut at the level of the fascia. This gives a clear view of the superficial muscles crossing the elbow on the lateral side. In order to remove the muscle fasciculi of the anterolateral group and to leave a maximum of the remaining connective tissue intact, lengthwise incisions are made in the epimysial connective tissue, or in the fascia when this is continuous with this epimysial connective tissue around the muscle. The muscle fasciculi are detached from their peripheral epimysial connective tissue and removed through the incisions (fig. 1.2.4). What remains is a three-dimensional system, with a complex

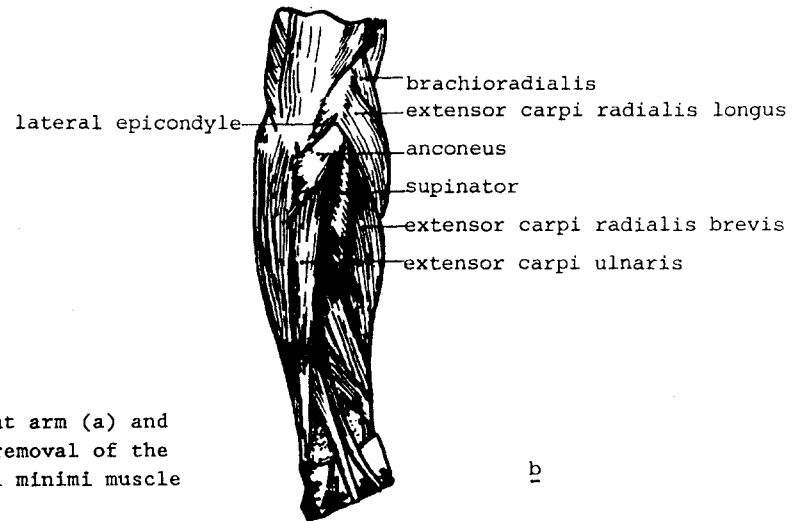
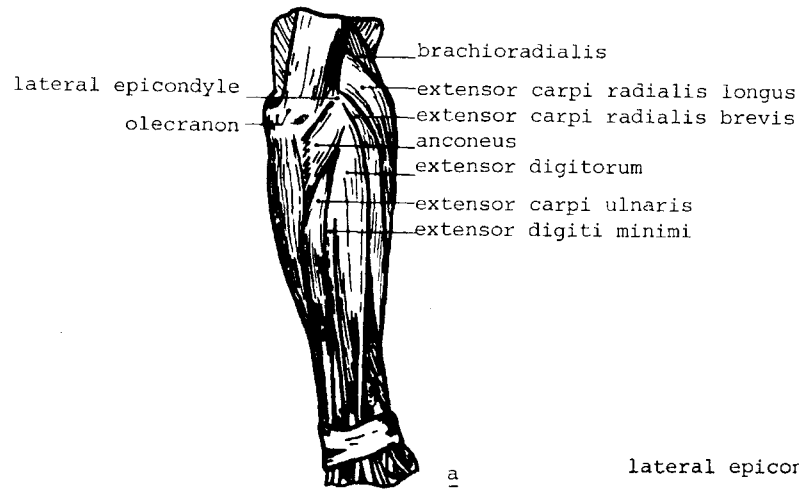


Fig. 1.2.2 Superficial extensor muscles of a right arm (a) and a view on the supinator muscle after removal of the extensor digitorum and extensor digiti minimi muscle (b).

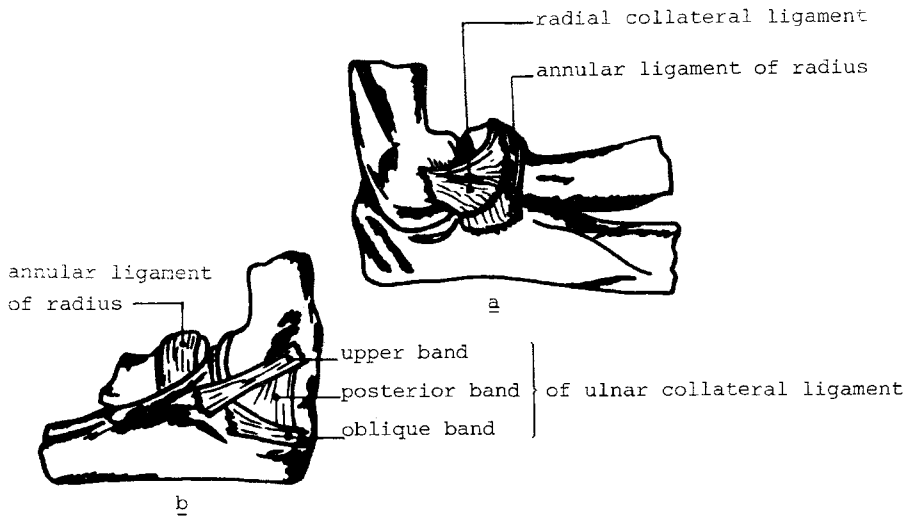


Fig. 1.2.3 Ligaments around the elbow joint; lateral (a) and medial (b) side.

topographical relation, of connective tissue septa in the proximal third of the forearm. These septa are parts of the walls of compartments from which inserting muscle fasciculi are removed. Directly distal to the lateral humeral epicondyle and latero-dorsal to the radial head, layers, which are the proximal continuations of the walls of the compartments, form an extensive complex of collagenous connective tissue (fig. 1.2.5). The deepest layer continues as the so-called fibrous capsular reinforcements of the humero-radial joint. It is not possible to detect distinct structures such as the radial collateral ligament or the annular ligament. After removing all the septa etc. up to the humeral lateral epicondyle, only very few fibres remain which are attached to both humerus and radius. Compared with the rest of the structure these fibres can only transmit a very small, practically negligible, load. There is no anatomical basis for the description of separate collateral or anular ligaments. In fact these are proximal continuations of the compartment walls mentioned. The so-called radial collateral ligament belongs to the septa within and around the muscles of the antero-lateral group; the anular ligament belongs to the sheath around the muscle fasciculi of the supinator muscle. The fibres of the last mentioned part do not lie circularly around the circumference of the radial head, as suggested by many pictures in classical text books of anatomy, but rather are helically oriented around the proximal part of the radius, superficial and proximal to the muscular tissue of the supinator muscle.

It is concluded that almost all of the collagenous connective tissue at the lateral aspect of the elbow joint is in series with muscular tissue thus transmitting the muscular tensile forces to the bone.

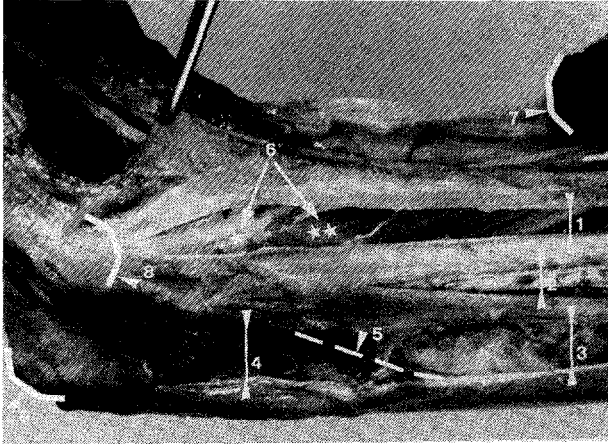


Fig. 1.2.4 Lateral side of the cubital regio of a right arm; brachioradialis, extensor carpi radialis longus and extensor carpi radialis brevis muscles are removed. Muscle fasciculi of the extensor digitorum, extensor digiti minimi, extensor carpi ulnaris, and anconeus muscles are detached and removed through incisions. The numbers in the figure indicate the following:

- 1: compartement of the extensor digitorum muscle
- 2: ,, ,, digiti minimi muscle
- 3: ,, ,, carpi ulnaris muscle
- 4: ,, anconeus muscle
- 5: boundary between the anconeus and the carpi ulnaris muscle
- 6: the septum underneath the extensor digitorum muscle (\*), to which fasciculi of this muscle were attached, lying loosely over the septum which covers the supinator muscle (\*\*)
- 7: distal muscle fibres of the brachioradialis and the extensor carpi radialis longus and brevis
- 8: lateral epicondyle
- 9: olecranon of ulna

(Courtesy H. van Mameren, 1984).

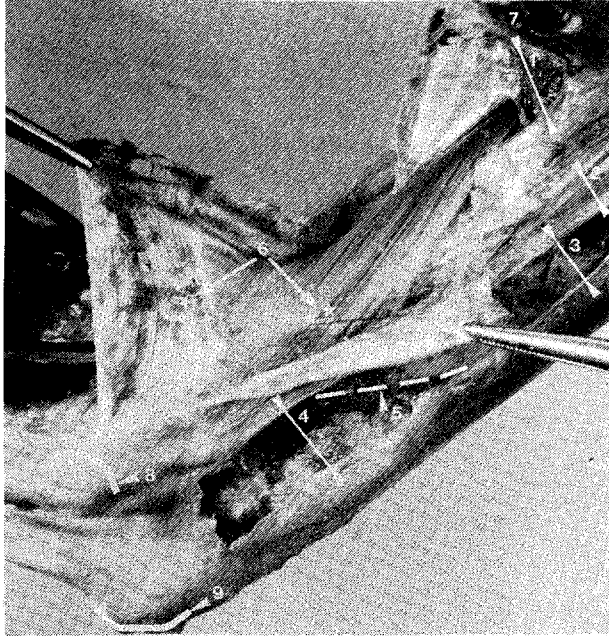


Fig. 1.2.5 The layers of collagenous connective tissue distal to the lateral humeral epicondyle. The meaning of the numbers is given in fig. 1.2.5 (courtesy H. van Mameren, 1984).

### 1.3 PURPOSE AND SCOPE OF THE PRESENT STUDY

In the previous section it was shown that the geometry of collagenous connective tissue structures around the lateral side of the elbow joint is more complex than in the classical description and that the concept of two parallel force transmitting systems is not always adequate. Moreover it was stated that detailed knowledge of the mechanical behaviour of such structures is of primary importance.

The mechanical behaviour of a structure can be described in terms of the state of stress and strain as a function of the material properties, the geometry and the boundary conditions. This is only possible when suitable constitutive equations are available. Ultimately, establishment of the constitutive behaviour of a material is an experimental problem. Common practice is to isolate samples of simple shape from the tissue under investigation, to load



these in a well controlled laboratory environment and to measure some load/deformation characteristic (Butler et al., 1978). The experiments are usually arranged in such a manner that the supposition of a homogeneous state of stress and strain seems reasonable and that the load history is simple. This has the advantage that only a few parameters are varied in one experiment and closed form solutions can be obtained for the theoretical model describing the experiment. Then it is possible to obtain a quantitative determination of material parameters.

There are a number of reasons why this does not work out for the connective tissues under consideration:

- First, because of inhomogeneous mechanical properties of the connective tissues, local slippage and premature failure in the grips and thickness variations of the samples, it is unlikely that a homogeneous strain distribution can be obtained. At least, the assumption of a homogeneous strain distribution has to be checked. The problem has been mentioned before in uniaxial tests (Zernick et al., 1984, Butler et al., 1984), biaxial tests (Humphrey et al., 1987), and it is raised as a reason for obscuring the value of constitutive models (Shoemaker et al., 1986). It is very likely that this problem is greatly underestimated and may be an important reason for the lack of conformity in reported results with regard to material and structural properties of biological tissues (Woo, 1986).
- As small samples of simple shape are prepared, the internal integrity of the tissue is highly disturbed. This can have far-reaching consequences on the way the tissue sample transfers the applied load. It is possible that a part of the sample, which is thought to be loaded is, in contrast, completely unloaded.
- The advantage of closed form solutions of the field equations describing the experiment lapses for the connective tissue under consideration. Because of the complex constitutive equations and the inhomogeneous properties, only numerical solutions can be obtained which demands for a completely different technique for parameter quantification.

Because of the above mentioned problems a development has been started which aims at measuring inhomogeneous stress and strain distributions as a start to a new way of tissue characterization. This has several advantages:

- As no precautionary measures have to be taken with regard to a desired strain distribution, more freedom in the design of experiments is obtained.
- Boundary conditions may be varied in many ways and thus more aspects of the material behaviour can be investigated. Consequently, parameters describing the material behaviour can be determined in one experiment.
- Demands for a simple geometry, which lead to disturbance of tissue integrity, may be dropped.

Only by means of a combination of a theoretical model and sophisticated experiments one may hope to gain some understanding of the above mentioned problems. That is why two parallel projects have been started at the same time. One project is focused on the development of a realistic theoretical model of connective tissue (Roddeman et al., 1986, 1987). The present thesis focuses on the development of the necessary experimental tools (Peters et al., 1986, 1987). Special attention is paid to an elaborate knowledge of the possibilities and restrictions of these tools.

In chapter 2 the development of a miniaturized force transducer of the buckle type is described. It can be positioned at a limited number of places in the structure and supplies information about the stress distribution in the tissue.

In chapter 3 a method for the measurement of strain distributions on curved outer surfaces of structures is described. This method is based on the application of image recording systems.

A description of the experimental set-up for strain distribution measurement is given in chapter 4.

In chapter 5 both techniques have been applied to study the behaviour of connective tissue samples. These tests had two objectives. On the one hand they were meant to support the above statements about the problems with regard to homogeneous stress and strain in tissue samples, and on the other they were meant to gain understanding on how these tissues transmit forces and investigate the relation between this function and the morphology. Chapter 6 contains the conclusions of the present study.

---

 2. FORCE MEASUREMENT
 

---

## 2.1 INTRODUCTION

In this chapter a redesign of the buckle transducer is described. It is used for the local measurement of (quasi-)static tensile forces in the membrane-like connective tissue structures around the elbow joint. The most important design requirements were:

- small sized relative to the dimensions of the structure under investigation.
- the width of the transducer must be equal to that of the strip of tissue on which the transducer is mounted.
- minimal hysteresis effects

The buckle transducer is a suitable means for direct measurement of tensile forces in rope- or membrane-like structures. Direct measurement of forces is an important advantage, because the mechanical properties of the material under consideration need not to be known. As will be shown in the present chapter this is only true if the transducer design satisfies certain conditions.

The buckle transducer was introduced in biomechanics by Salmons (1969) and used by many others (Barns and Pinder, 1974, Walmsley 1978, Lewis and Frasier, 1979, Lewis, Lew and Schmidt, 1982). Basically, it consists of a rectangular frame and a removable crossbar, the crossbar being much stiffer than the frame (fig. 2.1.1). As shown in fig. 2.1 a strip of tissue is led through the frame and over the crossbar. Exertion of a tensile force ( $\vec{F}(0)$ ) on

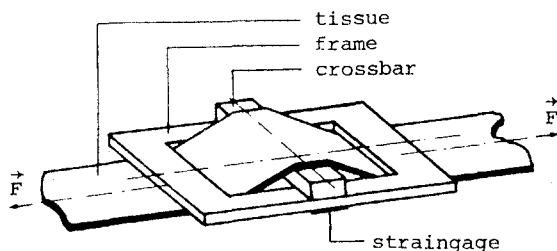


Fig.2.1.1 Basic principle of the buckle transducer.

the strip will cause the frame to deform. This deformation results in a strain gage voltage output that is directly related to the tensile force, thus providing a means for direct force measurement. From the reported results obtained by application of the buckle transducer it is clear that the usually applied transducers have a number of shortcomings. Not all aspects involved are well understood and further investigation and development is needed. From some pilot

studies it was concluded that none of the earlier designs of the buckle transducer were suitable for our purpose. Apart from their relatively large size these designs are prevented from a successful application towards our objective by three major disadvantages, affecting measurement accuracy and reproducibility. First, as the frame is considerably wider than the tissue strip led through (fig. 2.1.2.a), deformation of the frame will result not only from interaction with this strip but also from an unknown interaction with the surrounding tissue. Secondly, the actual mutual alignment of crossbar, frame and tissue strip may deviate from the desired configuration because their relative positions are not uniquely defined (fig. 2.1.2.b). Finally, the characteristics of the transducer show significant hysteresis.

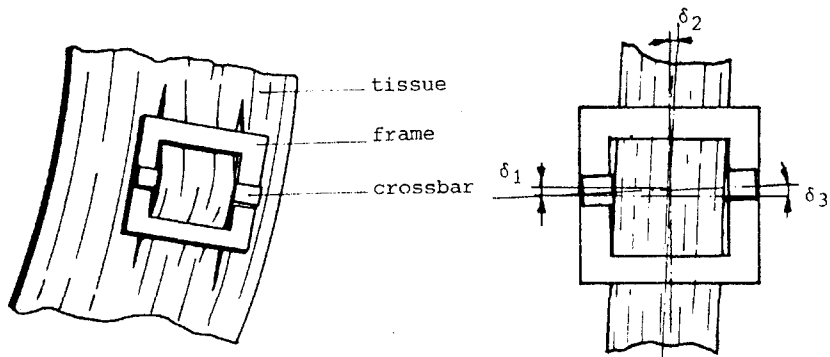


Fig. 2.1.2. Interaction of frame and surrounding tissue (a) and alignment errors (b).

With respect to the first disadvantage, modification of the transducer shape (substitution of the rectangular frame by a beam) is proposed by Peters et al. (1986) and Barry and Ahmed (1986). However, the large guides of the transducer applied by Barry and Ahmed may cause the same problem. Barry and Ahmed also pay attention to some problems with regard to the application of the buckle transducer. These are:

- decreasing tissue thickness due to the applied force
- preconditioning of the tissue
- shortening of the tissue due to transducer installation.

As will be discussed later these problems can be overcome by design adaptations. These adaptations are mainly prompted by a mechanical model of the buckle transducer.

The transducer design, special auxiliary tools and calibration are subject of the following section. The mechanical model is described in section 2.3 and finally, test results are presented in section 2.4.

## 2.2 REDESIGN OF THE BUCKLE TRANSDUCER

The redesigned buckle transducer is shown in fig. 2.2.1. The overall dimensions are 0.75 x 1.5 x 6 [mm]. The width of the frame is equal to the width of the tissue strip, so possible interaction with the surrounding tissue is minimized. This is also achieved by making the guides, which provide proper alignment of the transducer on the strip of tissue, as thin as acceptable. For this transducer the guides are 0.05 [mm] thick. The minimum dimensions of the frame are limited by the applied strainage (Micro Measurement, SA-09-030(G-120) that is cut to its minimum dimensions; 1.4 x 2.1 [mm]. Mounting of the strainage is done with a special tool because of the curved plane on

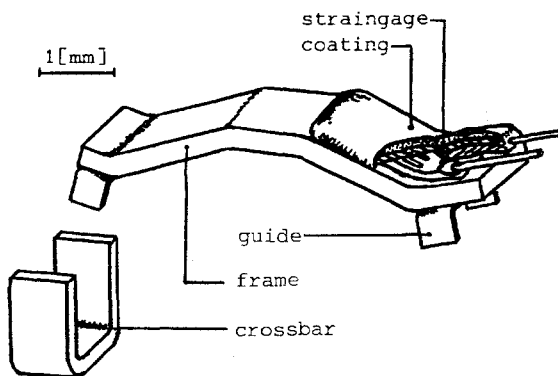


Fig. 2.2.1 The redesigned buckle transducer.

which it is bonded. For electrical insulation of the strainage a triple layered coating system is used: Ceta Bever two-component epoxy bond (layer 1), Micro Measurement M-coat D (layer 2), and Micro Measurement M-coat G (layer 3). The duration of life of the insulation is limited in situations where physiological solutions are used, but it is easy to apply a new coating. This concerns only the two top layers. Compensation of temperature effects is done with a dummy transducer (Doebelin, 1983).

Frame and guides are made of stainless steel while the crossbar is made of Molybdenum. Because of the relatively high Young's modulus of Molybdenum the crossbar combines a high stiffness with minimum dimensions; 0.15 x 0.9 x 4.5 [mm] in the unbended state.

The transducer is designed for a maximum load of 10 [N]. An installed buckle transducer is shown in fig. 2.2.2.

When installing the transducer the ends of the, disposable, U-formed crossbar are bent over the frame. This can be done with the aid of a specially developed installation tool (see fig. 2.2.3) or with the aid of two pairs of tweezers. In the first case, the distance  $\delta$  between frame and crossbar (as indicated in fig. 2.2.2) can be adjusted with the aid of the micrometer spindle.

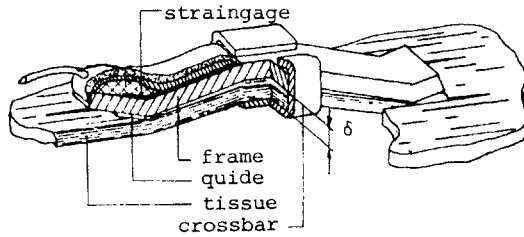
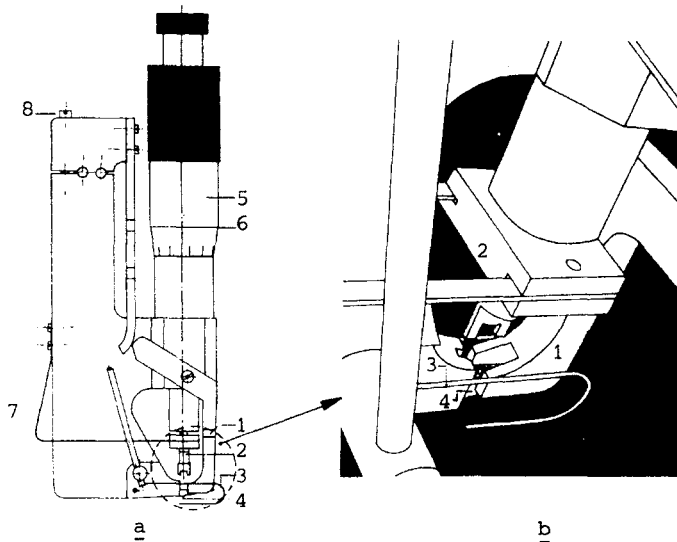


Fig. 2.2.2 The installed buckle transducer.



- |                            |                             |
|----------------------------|-----------------------------|
| 1: clamp                   | 5: micrometer spindle       |
| 2: crossbar bending stamp  | 6: clamp spring             |
| 3: auxiliary clamp springs | 7: bending stamp positioner |
| 4: crossbar bearer         | 8: spring-force adjustor    |

Fig. 2.2.3 Installation tool (a) and detail of the tool with a buckle transducer in it just before the crossbar ends are bent over the frame (b).

By adjusting the distance  $\delta$  the transducer's characteristics can be affected (see section 2.3). For this controlled way of transducer installation, calibration is needed only once for each transducer (measurement of sensitivity as a function of  $\delta$ ). This can be done on

a standard calibration body such as a thread, for example. Besides, in this way the transducer can be installed optimally with regard to friction (Peters, 1986). However, the use of the installation tool is elaborate due to the small dimensions of the transducer, and often leads to failures.

The second way of installation, by means of the tweezers, is much more convenient. In this case the strip of tissue is compressed between frame and crossbar without controlling the distance  $\delta$ . Thus, calibration has to be done after each installation. This is carried out as illustrated in fig. 2.2.4. Two threads are tied to the strip of tissue on both sides of the transducer. The threads, of which one is in series with another force transducer, are simultaneously loaded with an equal force. The output signals of buckle and the other force transducer are simultaneously measured. In this way, the sensitivity of the actual transducer-tissue unity is determined. It is important to use two counteracting threads; if only one thread is loaded, then surrounding tissue will transfer also a portion of the applied force. A disadvantage of this way of installation is the necessity of longer incisions than strictly required for the transducer installation, because room is needed for the threads.

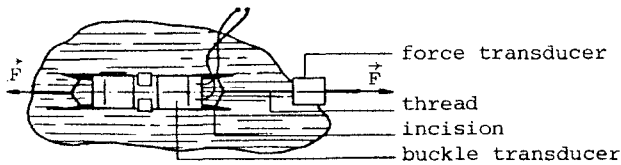


Fig. 2.2.4 Calibration of transducer-tissue unity using threads.

The implications of this easy way of installation for the transducer's characteristics are discussed in the next section, where the mechanical model of the transducer is examined. It will appear that this installation method has more benefits.

### 2.3 A MECHANICAL MODEL OF THE BUCKLE TRANSDUCER

To derive a relation between the tensile force  $\vec{F}(0)$  acting on the tissue strip and the strain induced by this load in the frame of the transducer, the quasi-static equilibrium of a part of the strip that is in contact with the frame, is considered (see fig. 2.3.1). The contact area between strip and frame is defined by the angle  $\alpha_1$ . It should be noticed that the tissue strip slips over the frame when it is loaded (and slips back in case of unloading). Friction between strip and frame will be taken into account supposing the Coulomb friction model is valid here. On the assumption that full slip

occurs, a straightforward calculation leads to the following expression for the force  $\vec{F}_f$  acting on the frame:

$$\vec{F}_f = - F(0) [e^{\mp\mu\alpha_1} \sin\alpha_1 \vec{e}_1 + (1-e^{\mp\mu\alpha_1} \cos\alpha_1)\vec{e}_2] \quad (2.3.1)$$

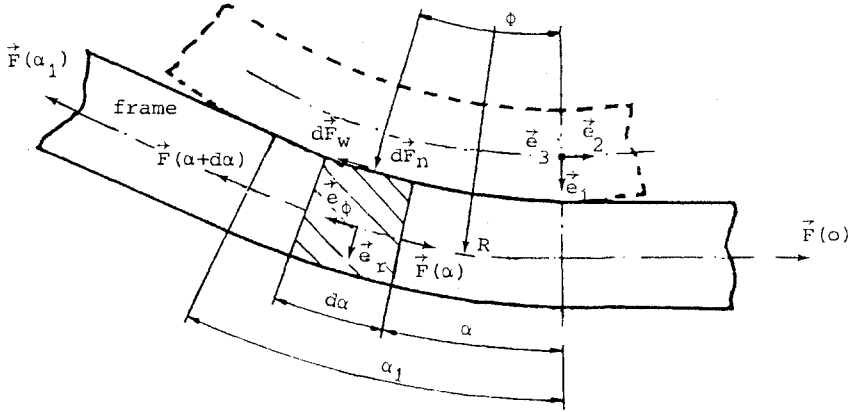


Fig. 2.3.1 Forces acting on an infinitesimal part of the tissue strip.

where  $\mu$  is the coefficient of friction, and the plus and minus signs apply for the cases of increasing and decreasing load  $\vec{F}(0)$  respectively. As the buckle transducer is symmetric it suffices to model one half of it as cantilever beam (see fig. 2.3.2).

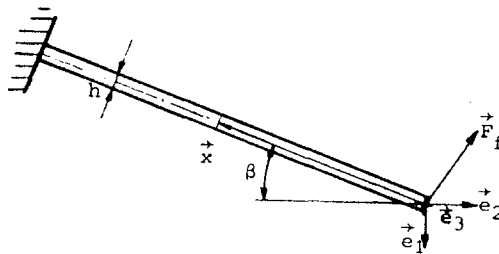


Fig. 2.3.2 Reduced model of the frame.

Neglecting shear forces, it is derived that the maximum principal strain in a cross-section of the frame at a position  $\vec{x}$  is given by:

$$\epsilon(\vec{x}) = - \frac{F(0)}{AE} [(\frac{\delta x}{h} \sin\beta - \cos\beta) - (\frac{\delta x}{h} \sin(\beta-\alpha_1) - \cos(\beta-\alpha_1))e^{\mp\mu\alpha_1}] \quad (2.3.2)$$



with:

E: Young's modulus and  
A: the cross-sectional area.

The angle  $\alpha_1$  in (2.3.2) is a function of the load  $\vec{F}(0)$ .

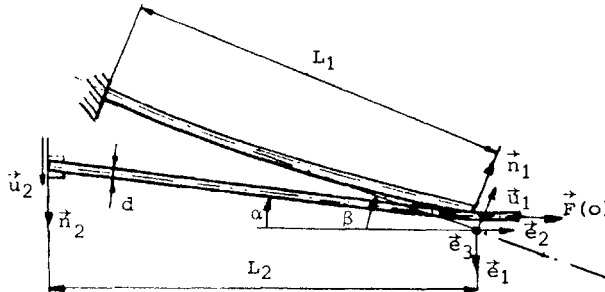


Fig. 2.3.3 Deflections of frame and crossbar.

Writing the deflection of the frame as  $\vec{u}_1 = u_1 \vec{n}_1$  with  $\vec{n}_1 = -\cos\beta \vec{e}_1 + \sin\beta \vec{e}_2$  and the deflection of the crossbar as  $\vec{u}_2 = u_2 \vec{n}_2$  with  $\vec{n}_2 = \vec{e}_2$ , it follows from fig. 2.3.3 that:

$$\tan \alpha_1 = \frac{\delta + d - u_1 \cos\beta - u_2}{L_2 + u_1 \sin\beta} \quad (2.3.3)$$

where  $d$ ,  $u_1$  and  $u_2$  are functions of the load  $\vec{F}(0)$ . It can be shown that  $u_1$  and  $u_2$  are negligibly small compared to  $(\delta + d)$  and  $L_2$ , at least for the present transducer. The dependence of  $d$  on the load  $\vec{F}(0)$  can be a source of errors. First, because of the visco-elastic properties of connective tissue it will, like the friction, cause hysteresis and, moreover, the output signal to be time dependent (Barry and Ahmed (1986)). Secondly, the characteristics of the transducer depend on the mechanical properties of the material under consideration. The relation between the thickness  $d$  and the load  $\vec{F}(0)$  is not determined by a simple one-dimensional stress-state but depends on the complex deformation of the tissue in the environment of the contact areas. However, it will be shown that these problems can be eliminated. From (2.3.2) it is seen that the term:

$$\left[ \frac{6x}{h} \sin(\beta - \alpha_1) - \cos(\beta - \alpha_1) \right] e^{\mp \mu \alpha_1} \quad (2.3.4)$$

includes all the mentioned difficulties. It is essential to minimize this term.

A possible method is to determine the value of  $\delta$  (see 2.3.3) for which the hysteresis is minimal (Peters, 1986) applying some proposed relation between  $d$  and  $\vec{F}(0)$ . The success of this method depends on

the proposed relation between  $d$  and  $\vec{F}(0)$ , the possibility to install the transducer with the determined  $\delta$ , and the measurement of the initial thickness of the tissue. For a transducer as small as the one described here, the installation with a prescribed value for  $\delta$  is feasible but troublesome. Further it is difficult to measure the thickness of soft tissues. That is why an alternative method is proposed.

Consider the situation for which  $\alpha_1 = \beta$ . Notice that, in this case, the tissue strip runs parallel to the frame. From (2.3.2) it can be seen that this would lead to a linear relationship between  $\varepsilon(\vec{x})$  and  $F(0)$ . It seems reasonable to provide that  $\alpha_1$  becomes equal to  $\beta$  somewhere in the loading range of the transducer. The resulting  $\varepsilon(\vec{x})$ ,  $F(0)$  curve is shown in fig. 2.3.4.

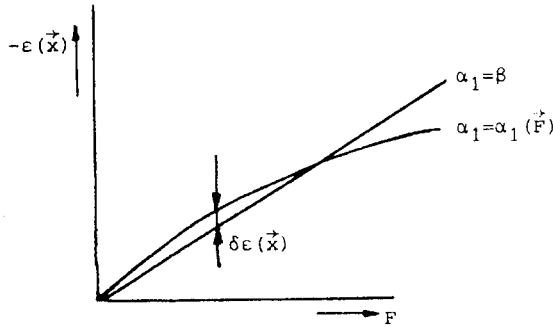


Fig. 2.3.4 The load-strain relation for  $\alpha_1 = \beta$  and for  $\alpha_1 = \alpha_1(F(0))$ . The angle  $\alpha_1$  decreases for an increasing load  $F(0)$ .

To obtain this situation,  $\alpha_1$  has to be larger than  $\beta$  in the unloaded state, so the tissue must be compressed against the frame by the crossbar when the transducer is installed (see fig. 2.3.5). As the thickness of the tissue strip is now prescribed for the compressed part, relation (2.3.3) should be adapted to this new situation. It follows (fig. 2.3.5) (neglecting  $u_1$  and  $u_2$ ):

$$\tan \alpha_1 = \frac{\delta + 0.5(d_c + d)}{L_2} \quad (2.3.5)$$

From (2.3.2) and (2.3.5) it follows that the relative deviations  $\Delta\varepsilon(\vec{x})/\varepsilon(\vec{x})$  caused by changes  $\Delta d$  of the tissue thickness can be expressed by (assuming that  $\mu\alpha_1 \ll 1$ ):

$$\frac{\Delta\varepsilon(\vec{x})}{\varepsilon(\vec{x})} = \frac{\cos^2 \beta}{2L_2 \sin \beta} \Delta d \quad (2.3.6)$$

From this it can be seen that the effect of thickness reduction on the output signal can be brought to an acceptable level provided that appropriate values are chosen for the transducer parameters  $\beta$  and  $L_2$  (see fig. 2.3.5).

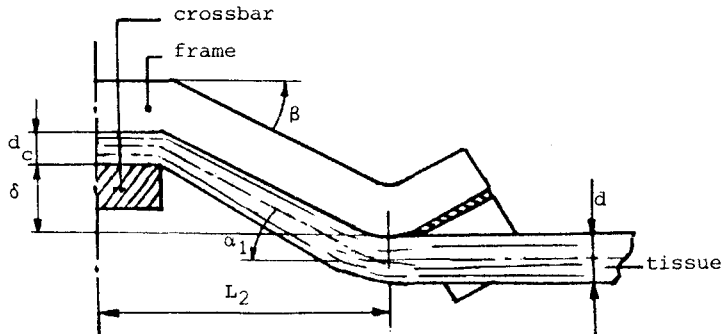


Fig. 2.3.5 An installed transducer whereby the tissue is compressed between frame and crossbar.

Of course, the foregoing is a qualitative analysis because:

- tissue thickness is not a well defined quality
- nothing is known about the thickness reduction  $\delta d$
- no statement is made about the extent to which the tissue should be compressed between the crossbar and the frame

However, a reasonable estimation of the effect of thickness reduction can be made. For example, if the initial thickness of the tissue strip is 0.5 [mm] and assuming the maximum thickness reduction occurring at the maximum load, to be less than 5% of the initial thickness it follows for the transducer described here ( $\beta = 0.26[\text{rad}]$ ,  $L_2 = 1.6[\text{mm}]$ ):

$$\left( \frac{\Delta \varepsilon(\vec{x})}{\varepsilon(\vec{x})} \right)_{\max} \leq 0.028 \quad (2.3.7)$$

This is improved for a decreasing initial thickness. From the foregoing it may be concluded that:

- the load-strain relation can be approximated by a linear function of the form  $\varepsilon(\vec{x}) = c F(0)$
- deviations from this function caused by thickness reduction can be brought within a level for which they may be regarded as acceptable measuring errors.
- as time dependency of the output signal is determined by the (visco-elastic) thickness reduction, this phenomenon also no longer has to be taken into account.

With regard to friction, the transducer installation according to the second procedure will not be optimal. However, it can be proven that deviations from the optimal performance are small. Besides, friction

between tissue and transducer, in the sense of a Coulomb friction model, may be expected to be low. Other friction phenomena such as hitching and grooving can be lowered by proper design.

The compression of the tissue between crossbar and frame is advantageous with respect to two more aspects:

- The shortening of the tissue strip due to transducer installation can be compensated (for example, 20 % thickness reduction of a strip with  $d = 0.4$  [mm] compensates the shortening completely).
- The transducer is clamped to the tissue strip, so shifting and twisting of the transducer with respect to the strip is being suppressed.

In this section it was shown that with the aid of a mechanical model of the buckle transducer insight can be gained with respect to optimal design as well as to installation prescriptions. Notwithstanding the qualitative character of the analysis it is obvious that a fair indication can be given for the circumstances for which the transducer can be used as a device, which has a linear behaviour and does not depend on the mechanical properties of the material under consideration.

#### 2.4 TEST MEASUREMENTS

The buckle transducer was subjected to several types of tests. In this section these tests are discussed.

##### Interfering inputs

An important error source is the interfering input caused by temperature changes. Temperature effects are compensated with a dummy transducer. Long duration measurements with the temperature kept at a constant level (S.D.  $0.02$  [ $^{\circ}\text{C}$ ], 2000 samples over 8 hours) demonstrated an average zero drift of less than 0.3% of the full scale (10 [N]) with a standard deviation better than 0.4% of the full scale. However, with application of the transducer under normal circumstances whereby the control over the conditions is less, this accuracy is not achieved. Besides, a dummy transducer does not compensate other electric interfering inputs. The answer to this problem is the simultaneous measuring of loaded and unloaded transducers. Assuming that the output signals of all the transducers, loaded and unloaded, contain partly the same errors caused by interfering inputs, the output signal of the loaded transducers can be corrected by subtraction of the (averaged) output signal of the unloaded transducers. This procedure is demonstrated when time dependency of the transducer output signal caused by visco-elastic tissue thickness reductions is brought into discussion.

##### Hysteresis phenomena

Friction between the transducer and the tissue and visco-elastic properties of the tissue are sources for hysteresis phenomena. To

demonstrate the hysteresis caused by friction the transducer was mounted to a linen rope with elastic properties. As was shown in section 2.3, adjusting the distance  $\delta$  affects hysteresis. Fig. 2.4.1 shows the measured load-strain curves for two different values of  $\delta$ . The hysteresis, as demonstrated by curve 1 can be lowered as shown by curve 2. The almost linear behaviour of the transducer is also reflected by curve 2.

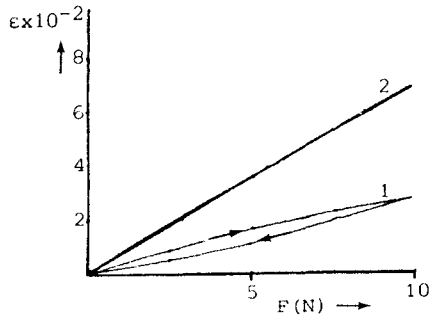


Fig. 2.4.1 Measured load-strain curves for two different values of  $\delta$  ( $\delta_1 = 0.57[\text{mm}]$ ,  $\delta_2 = 0.27[\text{mm}]$ ).

A time dependence of the output signal caused by visco-elastic material properties is considered together with errors caused by interfering inputs. For the latter, errors which are the same for

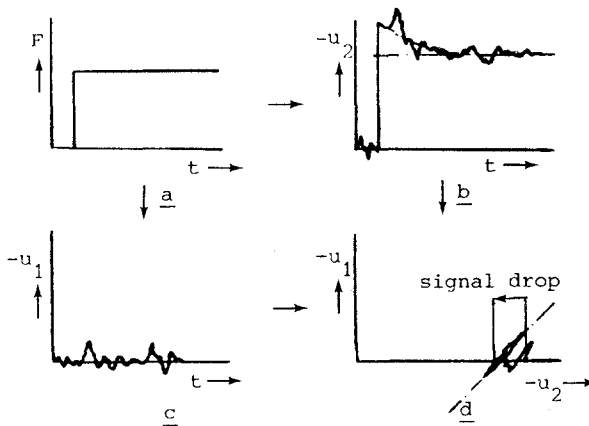


Fig. 2.4.2 The output signal  $u_1$  (b) of a transducer loaded with a step force (a) and the output signal  $u_2$  (c) of an unloaded transducer plotted in one diagram (d). The output signal  $u_1$  is plotted (b) with (—) and without (---) errors caused by interfering inputs.

loaded and unloaded transducers and errors which are different for each transducer separately, are distinguished. Theoretically the output signals of a transducer loaded with a step force and an unloaded transducer would look like figs. 2.4.2.b and c. Plotting  $u_1$  against  $u_2$  would lead to fig. 2.4.2.d. Variations along the line L in fig. 2.4.2(d) are caused by errors which are the same for both transducers. These errors can be removed from  $u_1$  by subtraction of  $u_2$ . As stated in the previous section, the signal drop caused by the visco-elastic thickness reduction can be reduced by proper design and correct installation of the transducer. In fig. 2.4.3 the measured output signals of a loaded and an unloaded transducer are plotted in one graph. It can be seen that no signal drop because of viscoelastic effects can be distinguished.

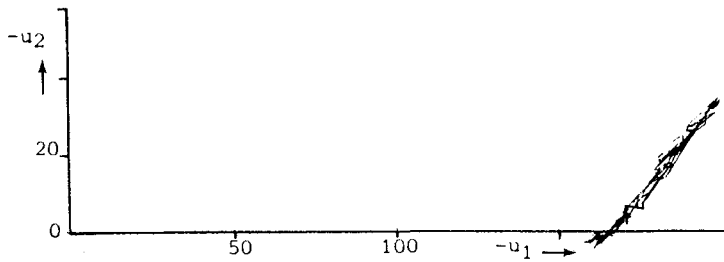


Fig. 2.4.3 Measured output signals of a loaded and an unloaded transducer plotted in one graph.

The standard deviation of the random errors is less than 2.5% of the full scale.

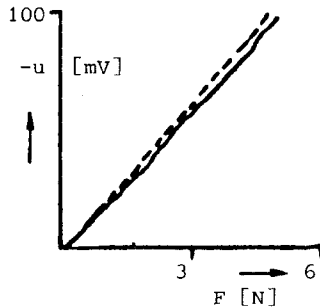


Fig. 2.4.4 Load-strain relation according to calibration (1) and according to the situation of loading a specimen without transducer surrounding tissue (b).

### Calibration

To check the calibration method described in section 2.2 a transducer was installed in a tissue specimen and calibrated according to the prescribed procedure. After that, the tissue surrounding the transducer was cut and the specimen was loaded again. The results of this procedure are shown in fig. 2.4.4.

The difference between the two curves is less than 1.5 % which is satisfactory, taking into account the standard deviation of 2.5% for the random errors.

In this section it was demonstrated that the newly designed buckle transducer satisfies the expectations prompted by the mechanical model described in section 2.3.

The model gives a good insight into the behaviour of the transducer and leads to solutions for problems.

With the improvements concerning the proper mutual alignment of frame, crossbar and tissue strip, the prescriptions for installation and the calibration method, the redesigned buckle transducer is believed to be an improvement when compared to earlier designs. It has proven to be accurate to an acceptable level for local force measurement, taking into account the complex interaction between transducer and tissue and despite its small dimensions.





---

### 3. STRAIN MEASUREMENT

---

#### 3.1 INTRODUCTION

This chapter deals with the theoretical backgrounds of a method for measuring strain distributions by means of an image recording system. The decision to use an image recording system is based on the important advantages that the method is non contacting and that a large amount of information on the strain distribution can be collected. Much attention is paid to error sources and the way they affect the measured strains. A good understanding of these effects is of decisive importance for a successful experimental set-up and a correct interpretation of the results.

Strain measurement on biological tissues brings along several specific problems. Numerous precautions must be taken and prior to and during testing to measure reproducible results.

General problems and problems related to the strain measurement techniques are distinguished. General problems are:

- a. individual genetic and epigenetic variations
- b. characterization and thus classification of donor tissue fails
- c. preparation and storage of specimens
- d. control of testing environment
- e. alteration of the tissue properties in time.

For a discussion on these problems reference is made to literature (Butler et al., 1978, Hubbard and Soutas-little, 1984, Panjabi et al., 1984, Hasberry and Percy, 1986, Woo et al., 1986)

Problems related to the applied techniques for strain measurement are:

- a. transmission of forces and/or displacements to the specimen
- b. influence of the applied transducers on the strain field
- c. realization of a homogeneous strain distribution
- d. definition of a reference configuration

They are elucidated briefly here below.

#### sub a

The transmission of forces and/or displacements to a specimen is done by attaching a clamp. Tissue may slip within the clamps. This is one of the reasons that calculating tissue strain from measured clamp displacements is not advisable. Moreover, large clamping forces introduce initial, unintended large deformations. Finally, it is often not clear whether all parts of the tissue within the clamps are proportionally loaded.

sub b

Techniques for the measurement of strain whereby transducers are connected to the tissue, such as high-extension rubber strain gages (Mizrahi 1980), liquid metal strain gages (Seireg 1978, Stone, et al., 1983, Riemersma, 1986) and Hall effect devices (Arms et al., 1983), demand stringent requirements with respect to the measuring force and the connection itself. Due to the very low initial stiffness relatively small loads may already cause large deformations which interfere strongly with the deformation to be measured. Moreover, it is often a troublesome and laborious work to create a well defined connection between tissue and transducer. When there is little control on how the connection is accomplished, the transfer of the measured signal from the tissue to the transducer is arbitrary.

sub c

There are several reasons violating the assumption of a homogeneous strain distribution. This has already been pointed out extensively in chapter 1.

sub d

It is unfeasible to define a reproducible reference configuration while the specimen is unloaded. The problem of the definition of a reference configuration concerns specimen dimensions as well as shape. Unloaded means here the absence of controlled prescribed forces. As the initial stiffness of a specimen is very low, both due to mechanical properties (low Youngs moduli, low shear moduli) and due to geometrical properties (small thickness) an extremely low force can already cause large deformations. It should be noticed that a specimen actually never is in an unloaded state. Gravitation, surface tension, measuring forces, etc. are always present and, in consequence of the low initial stiffness, may affect the geometry considerably.

Because of the disadvantages of techniques for strain measurement on soft tissue which apply transducers which contact the tissue, within the present work a strain measuring technique which does not demand for contact with the tissue, is chosen. Besides, as has been argued before, this measuring technique must be suited to measure non-uniform strain distributions. The measurements will be restricted to quasi-static states of the object under investigation.

The method described is based on a reconstruction of the spatial coordinates of the centroids of markers, attached to the tissue, from recorded images (Notice that the attachment of markers to the tissue demands for contact before the actual measurements are performed. However, there are no measuring forces and the only demand for a marker is that it keeps its position on the tissue). When the coordinates of the markers are known for two configurations, the mutual displacements of the markers can be determined. From the mutual displacements of markers lying close together, the local

strain components can be estimated if a suitable mathematical model is available.

Most of the reported work concerning strain measurement with the aid of image recording systems has been done with one camera and is restricted to two-dimensional measurements. This means application to planar objects which do not rotate out of their initial plane (Hoffman and Grigg, 1984, Woo et al., 1986) or the assumption that the curvature of the object may be neglected (Prinzen et al., 1986). When the outer surface of an object is curved and/or the object rotates, the 3-Dimensional coordinates of the markers have to be measured. The estimated strains however are in this case two-dimensional.

Recent advances in analytical photogrammetry have made non-metric or amateur cameras become suitable for applications where moderately high relative accuracy is satisfactory ("in the range of 1:6000 to 1:10000 or better", Karara, 1985). In this case, however, correction of errors of the measured data is of great importance and has to be done for each recorded image separately because the error sources may not be expected to be stable in time (Feig, 1971). In literature on strain measurements, the reported accuracy is often disappointing. The main reason for that may be the omission of correction of the measured data.

The mathematical models which describe the several stages of the measuring method, are subject of this chapter. They serve not only for the development of efficient algorithms for computation and justified methods for the determination of the strain distribution, but also as a guide for the design and the construction of the experimental set-up. In section 3.2.1 the theory of the central projection, which describes the transformation from the object space to the image plane, is treated briefly. Then, in section 3.2.2, a model is developed for the reconstruction of the three-dimensional coordinates of the centroids of markers by means of statistics. A special choice is made for the position and orientation of the image planes. This special choice has advantages with regard to the simplicity of the reconstruction model, for the calibration and correction model and for the construction of the experimental set-up. In section 3.3.1 a general 3-dimensional model is derived for the estimation of the deformation gradient tensor  $F$  by means of markers lying close together. By means of an estimate of  $F$ , different types of strain measures can be calculated. This is restricted to the Green-Lagrange strain tensor, however. It is important to notice that only estimates for the strain components can be derived. Not only because of measuring errors but, and this has often more impact, also because the vectors from which the strain components have to be calculated are finite while the definition of strain refers to infinitesimal vectors. This leads to contradictory demands. For a good estimate of strains, markers have to be close together. However, this means that their mutual displacements will be small and thus relatively less accurately measured. (A more accurate definition of

"lying close together" is given in chapter 4, section 4.2.3). The special case of strain measurement on curved outer surfaces is discussed in section 3.3.2. Next, in section 3.4, the marker identification problem is dealt with. Two types of identification problems are distinguished. First, identification of markers from two different images of the same configuration of a body and secondly, identification of markers from two different configurations of a body. In the last section (3.5) extensive attention is paid to different types of measuring errors. A method for the correction of systematic errors is derived and the influence of random errors on the displacement gradient tensor  $F$  and the Green-Lagrange strain tensor is expressed by means of their most important statistical properties. These are important for design for accuracy and useful for a correct interpretation of experimental results as will be shown in the next chapter.

### 3.2 RECONSTRUCTION OF SPATIAL MARKER COORDINATES

#### 3.2.1 Theory of the central projection

In this section a short description of the theory of the central projection is given. For a more extensive treatment reference is made to literature (Schwidersky and Ackermann, 1976).

The image of the object space formed by a set of lenses is a perspective transformation of that object space. This perspective transformation from the three dimensional object space to the two dimensional image plane, is described with the aid of the theory of the central projection. This theory is strongly allied with the theory of geometrical optics. However, not the development of physical models but rather the description of the geometrical results is the purpose and scope of this theory.

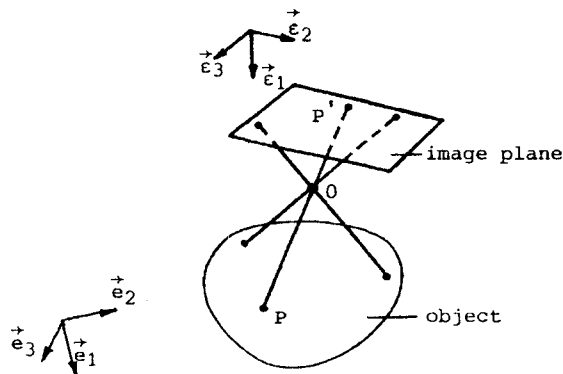


Fig. 3.2.1 Geometrical model of a perspective transformation.

The object space is transformed into a set of geometrical points in the image plane. It is assumed that the following statements hold (see fig. 3.2.1):

- an object point, its corresponding image point and the centre of projection are points of a straight line
- the object space consists of a set of geometrical points which do not change during exposure time

Two orthonormal coordinate systems are introduced: The object space coordinate system  $\vec{e}_i$ ;  $i \in [1,2,3]$  and the image coordinate system  $\vec{e}_j$ ;  $j \in [1,2,3]$  respectively. One of the unit vectors  $\vec{e}_j$  is, by definition, always perpendicular to the image plane. Here, the unit vector  $\vec{e}_1$  is chosen (fig. 3.2.1). From this it follows that the component  $x_1 = \vec{x} \cdot \vec{e}_1$  of a position vector  $\vec{x}$  of an image point has the same, constant value for all image points. There is no fundamental difference between choosing the image plane and object on one or on the other side of the centre of projection (compare fig. 3.2.1 with fig. 3.2.2). The relationship between the coordinates

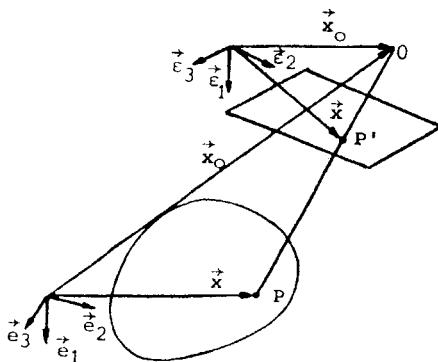


Fig. 3.2.2 Position and orientation of object and image plane with respect to the centre of projection.

$\underline{x}$  of a position vector  $\vec{X}$  of a point P in the object space and the coordinates  $\underline{x}$  of a position vector  $\vec{x}$  of the corresponding projected point P' on the image plane, is described by the collinearity equation:

$$\frac{\underline{x} - \underline{x}_0}{\|\underline{x} - \underline{x}_0\|} = R \cdot \frac{\underline{X} - \underline{X}_0}{\|\underline{X} - \underline{X}_0\|} \quad (3.2.1)$$

where  $\underline{X}_0$  and  $\underline{x}_0$  are the coordinates of the position vectors  $\vec{X}_0$  and  $\vec{x}_0$  of the centre of projection O with respect to object space coordinate system and the image coordinate system respectively (see fig. 3.2.2), and R is a proper orthonormal matrix with the properties:

$$\underline{R}^C \cdot \underline{R} = \underline{I}; \quad \det(\underline{R}) = 1. \quad (3.2.2)$$

The matrix  $\underline{R}$  transforms the object space coordinate system to the image coordinate system. If  $\vec{\varepsilon}_1$  is the unit vector perpendicular to the image plane, then the camera constant  $c$  is defined as:

$$c = x_1 - x_{01} \quad (3.2.3)$$

Relation (3.2.1) contains nine independent parameters: The six components of the coordinates  $\underline{x}_0$  and  $\underline{X}_0$  and three independent quantities which determine the matrix  $\underline{R}$ . Between the nine components of  $\underline{R}$  there are six independent relations: The orthogonality relations (Bopp and Krauss, 1978). From (3.2.1) and (3.2.3) one can find an explicit expression for the image coordinates  $\underline{x}$ :

$$\underline{x} = \frac{c}{R_{1i}(x_i - X_{0i})} \underline{R} \cdot (\underline{X} - \underline{X}_0) + \underline{x}_0 \quad (3.2.4)$$

Or with:

$$a = -R_{1i} X_{0i} \quad (3.2.5)$$

which is called the camera distance:

$$\underline{x} = \frac{c}{R_{1i} X_i + a} \underline{R} \cdot (\underline{X} - \underline{X}_0) + \underline{x}_0 \quad (3.2.6)$$

Expression (3.2.6) describes a unique, non-linear transformation of the three dimensional coordinates  $\underline{X}$  to the image plane. It is not possible to obtain unique spatial coordinates  $\underline{X}$  from given image plane coordinates  $\underline{x}$ . This can be seen by substitution of arbitrary coordinates  $\underline{x}$  from the set:

$$\underline{X} = \underline{X}_s + \alpha(\underline{X}_s - \underline{X}_0); \alpha \in \{R\} \quad (3.2.7)$$

into (3.2.6). From (3.2.1) only two equations can be obtained for three unknown object point coordinates. It is necessary that object points are transformed to two or more differently oriented image planes, to be able to reconstruct the coordinates of an object point. In the next section this method will be described for a particular choice of the image plane orientations.

### 3.2.2 A theoretical model for the reconstruction of spatial marker coordinates.

If one of the relations formulated in the previous section is used for the reconstruction of object space coordinates, the nine independent parameters expressed by  $\underline{X}_0$ ,  $\underline{x}_0$  and  $\underline{R}$  must be known. A common way to determine these parameters is by means of a transformation of a sufficient number (at least 5) of control markers in the object space, from which the spatial coordinates are known for each camera that is used. From relation (3.2.1) a set of non-linear

equations for the nine unknown parameters can be derived. The known spatial and image coordinates of control markers are substituted in these equations. A frequently used method for the solution of this problem is the Direct Linear Transformation (DLT) (Abdel-Aziz and Karara, 1971). Within this method eleven new parameters are introduced which are functions of the original nine independent parameters. As these parameters are considered to be independent, this method is an approximation of the original problem (Bopp & Krauss, 1978). At least six control markers are needed for the Direct Linear Transformation method. If a high accuracy is desired, this method is not suitable (Fioretti et al., 1985, Wood and Marshall, 1986).

Our starting point is the supposition that the two times nine independent parameters are known for two differently oriented image planes. First, the origins of the image plane coordinate systems are chosen in such a way that they coincide with the centres of

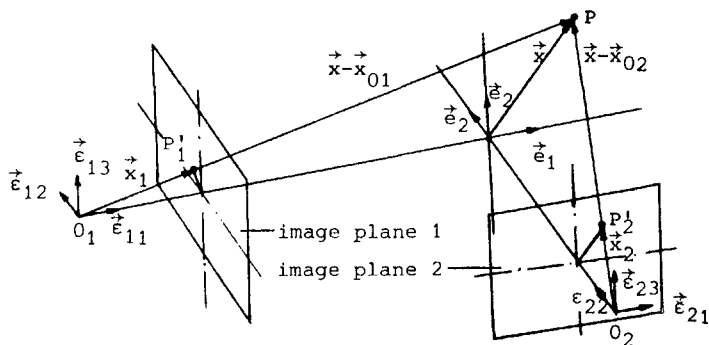


Fig. 3.2.3 The set-up of the two image planes with respect to the object space coordinate systems.

projection of the corresponding image planes. Therefore  $x_{0i} = 0$ , where  $i \in \{1, 2\}$  is a label for the image planes. Further, the optical axes, which are perpendicular to the corresponding image planes, pass through the origin of the spatial coordinate system and are parallel with  $a$ , for both image planes different, base vector of this system. This set-up has the advantage of maximum stereo separation (Erdman et al., 1979). Finally, the camera constant  $c$  is chosen equal to the camera distance  $a$ , and the camera distance is assumed to be the same for both image planes. As will be shown in section 3.5 the choice  $c=a$  is not a restriction for the method described here. The set-up of the image planes as described is shown in fig. 3.2.3. For this set-up it is seen that:

$$\begin{aligned} x_{01} &= 0 & x_{02} &= 0 \\ R_1 &= I & R_2 &= I \end{aligned} \quad (3.2.8)$$

$$x_{11} = a$$

$$x_{22} = a$$

The components  $x_{ij}$ ;  $i \in \{1, 2\}$ ,  $j \in \{1, 2, 3\}$  are, according to (3.2.6) given by:

$$x_{ij} = \frac{a}{\bar{X}_i + a} (X_j + a \delta_{ij}) \quad ; \quad i \in \{1, 2\}, j \in \{1, 2, 3\} \quad (3.2.9)$$

For  $i = j$ , (3.2.9) gives a trivial result, so (3.2.9) leaves us with an indeterminate set of four non-trivial, non-linear equations for the three components  $X_j$  which we may write as:

$$\underline{x} = \underline{f}(\underline{X}, a) \quad (3.2.10)$$

where:

$$\underline{x} = [x_{12}, x_{13}, x_{21}, x_{23}]^T \quad (3.2.11)$$

$$\underline{X} = [X_1, X_2, X_3]^T \quad (3.2.12)$$

$$\underline{f}(\underline{X}, a) = \left[ \frac{a X_2}{\bar{X}_1 + a}, \frac{a X_3}{\bar{X}_1 + a}, \frac{a X_1}{\bar{X}_2 + a}, \frac{a X_3}{\bar{X}_2 + a} \right]^T \quad (3.2.13)$$

As the image plane coordinates  $x_{ij}$ , obtained from observations during an experiment, contain random errors  $\bar{v}_{ij}$ , they should be treated as stochastic variables (Systematic errors are discussed in section 3.5 and ignored here). The set of image coordinates  $\bar{\underline{z}}$  containing a random error is defined by:

$$\bar{\underline{z}} = \underline{x} + \bar{\underline{v}} \quad (3.2.14)$$

where  $\bar{\underline{v}}$  is the set of random errors given by:

$$\bar{\underline{v}} = [\bar{v}_{12}, \bar{v}_{13}, \bar{v}_{21}, \bar{v}_{23}]^T \quad (3.2.15)$$

It is assumed that these errors are statistically independent and have a normal distribution. The expected values and variances of the errors are given by:

$$E(\bar{\underline{v}}) = \underline{0} \quad (3.2.16)$$

$$E(\bar{\underline{v}}\bar{\underline{v}}^T) = \sigma^2 \underline{I} \quad (3.2.17)$$

where  $\underline{I}$  is a fourth-order identity matrix. From (3.2.10) and (3.2.14) it follows :

$$\bar{\underline{z}} = \underline{f}(\underline{X}, a) + \bar{\underline{v}} \quad (3.2.18)$$

The statistical model expressed by (3.2.18) is known as a Fisher-model (Schweppe, 1972). A correct way to obtain a set of estimates  $\hat{\underline{x}}$  for the set of coordinates  $\underline{x}$  is the maximum likelihood method. In



that case the probability density function  $p(\underline{z}; \underline{X})$  given by (Kreyszig, 1983):

$$p(\underline{z}; \underline{X}) = \frac{1}{4\pi^2 \sigma^4} e^{-\frac{1}{2\sigma^2}(\underline{z} - \underline{f}(\underline{X}, a))^T \cdot (\underline{z} - \underline{f}(\underline{X}, a))} \quad (3.2.19)$$

is maximized for a given set of observations  $\underline{z}$ . The maximum of  $p(\underline{z}; \underline{X})$  is reached when the scalar function  $J(\underline{X})$  given by

$$J(\underline{X}) = (\underline{z} - \underline{f}(\underline{X}, a))^T \cdot (\underline{z} - \underline{f}(\underline{X}, a)) \quad (3.2.20)$$

is minimal. A standard calculation leads to the set of equations given by:

$$\left( \frac{\partial \underline{f}(\underline{X}, a)}{\partial \underline{X}} \right)^T \Big|_{\underline{X}=\hat{\underline{X}}} \cdot (\underline{z} - \underline{f}(\hat{\underline{X}}, a)) = \underline{0} \quad (3.2.21)$$

These equations can be solved iteratively (For a thorough discussion on this subject see Scales, 1985).

An explicit expression for the set of estimates  $\hat{\underline{X}}$  can be derived if a more intuitive method, based on the method of least squares, is used. This method is described in appendix A. As no iterative solution process is needed, this method is less time consuming. It is easily shown that, whereas in the iterative method the residuals  $\bar{v}_{ij}$  (3.2.15) are minimized, residuals of the form

$$\left(1 + \frac{X_1}{a}\right) \bar{v}_{ij} \quad (3.2.22)$$

are minimized with the method described in appendix A, this method being less accurate. However, when  $\frac{X_1}{a} \ll 1$  this may be acceptable. The magnitude of  $\frac{X_1}{a}$  depends on the experimental set-up.

Of course it is not possible to create a set-up of the image planes which satisfies exactly the configuration as defined here; some deviations will always occur. Besides, it is important to know how large the influence is of some specific deviation on the final measurement data, so indications can be given which factors need extra attention with design. This will be the subject of section 3.5 where systematic errors and corection of these errors are discussed.

### 3.3 STRAIN ESTIMATION FROM MEASURED MARKER COORDINATES

#### 3.3.1 Estimation of deformation quantities

Consider a body M. Each material point of M has a unique label  $\xi$  (see fig. 3.3.1):

$$\xi^T = [\xi_1, \xi_2, \xi_3] \quad (3.3.1)$$

The position vector  $\vec{x}$  of a material point depends on the time  $t$  and a label  $\xi$  (the material coordinates):

$$\vec{x} = \vec{x}(\xi, t) \quad (3.3.2)$$

For  $t = t_0$  it is written:

$$\vec{x}_0 = \vec{x}(\xi, t_0) \quad (3.3.3)$$

A curve with  $\xi_i$  is constant for  $i \neq j$  is called the  $\xi_j$  parametric curve. The tangent vectors  $\vec{c}_i$  of the three parametric curves are

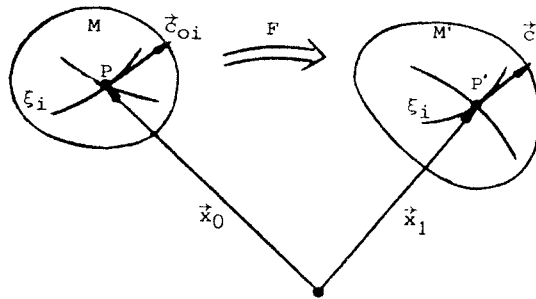


Fig. 3.3.1 Two states of a deformable body  $M$ .

mutually independent and constitute a local vector basis:

$$\vec{c}_i = \frac{\partial \vec{x}}{\partial \xi_i} \quad ; \quad i \in \{1, 2, 3\} \quad (3.3.4)$$

The configuration at time  $t = t_0$  is defined as the reference configuration. Tangent vectors at a time  $t$  are related to the corresponding tangent vectors at time  $t_0$  by:

$$\vec{c}_i = F \cdot \vec{c}_{0i} \quad ; \quad F = (\vec{\nabla}_0 \vec{x})^c \quad (3.3.5)$$

where  $\vec{\nabla}_0$  is the gradient operator with respect to the reference configuration and  $F$  is the deformation gradient tensor. Consider two points  $P$  and  $Q$  (marker centroids) in the reference configuration at  $t = t_0$  and in an arbitrary configuration at time  $t$ . The vectors connecting  $P$  and  $Q$  are denoted as  $\Delta \vec{x}_0$  and  $\Delta \vec{x}_1$ , respectively. Writing  $\Delta \vec{x}_0$  as:

$$\Delta \vec{x}_0 = \sum_{i=1}^3 \Delta x_{0i} \vec{c}_{0i} \quad (3.3.6)$$

it follows from (3.3.5):

$$\sum_{i=1}^3 \Delta x_{0i} \vec{c}_i = F \cdot \sum_{i=1}^3 \Delta x_{0i} \vec{c}_{0i} \quad (3.3.7)$$

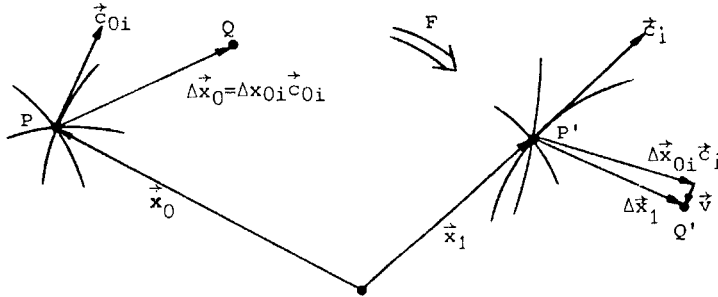


Fig. 3.3.2 Two marker centroids P and Q in two different configurations and definition of the model error  $\vec{v}$ .

Defining a vector  $\vec{v}$  as (see fig. 3.3.2):

$$\vec{v} = \Delta \vec{x}_1 - \sum_{i=1}^3 \Delta x_{0i} \vec{c}_i \quad (3.3.8)$$

(3.3.7) can be rewritten to:

$$\Delta \vec{x}_1 - F \cdot \Delta \vec{x}_0 = \vec{v} \quad (3.3.9)$$

As one can see from (3.3.9) and fig. 3.3.2 the vector  $\vec{v}$  is the "model error" due to the fact that  $\Delta \vec{x}_1$  and  $\Delta \vec{x}_0$  are finite vectors. Notice that  $\vec{v} = \vec{0}$  for a homogeneous strain field. When  $\Delta \vec{x}_1$  and  $\Delta \vec{x}_0$  become infinitely small, it is seen that:

$$\lim_{\substack{\Delta \vec{x}_1 \rightarrow \vec{0} \\ \Delta \vec{x}_0 \rightarrow \vec{0}}} (\Delta \vec{x}_1 - F \cdot \Delta \vec{x}_0) = \vec{0} \quad (3.3.10)$$

and from this the commonly used definition of F in terms of infinitesimal quantities  $d\vec{x}_0$  and  $d\vec{x}_1$  is found:

$$d\vec{x}_1 = F \cdot d\vec{x}_0 \quad (3.3.11)$$

Returning to (3.3.9), which is the starting point for the estimation of strain quantities from measured marker coordinates, first an expression for an estimate  $\hat{F}$  of the deformation gradient tensor F in a material point is derived. If from a group of markers the coordinates are measured for two different configurations of a body one can calculate the vectors  $\Delta \vec{x}_{0i}$  and  $\Delta \vec{x}_1$  (stochastics) which connect one marker (P) of the group to the rest of the markers (see fig. 3.3.3).

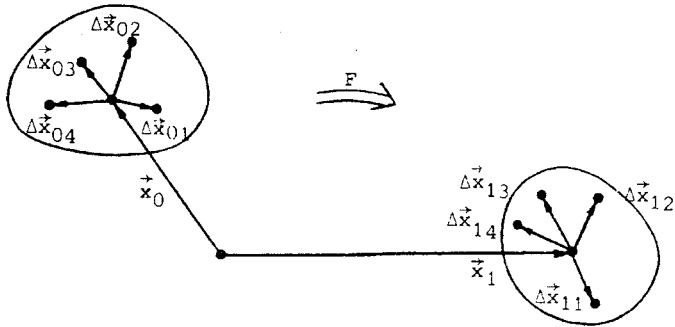


Fig. 3.3.3 A group of markers from which an estimate for the deformation gradient tensor  $F$  in point  $P$  is calculated.

The marker  $P$  is called the central marker. According to (3.3.9) it is written:

$$\vec{\Delta x}_{1i} - F \cdot \vec{\Delta x}_{0i} - \vec{v}_i = \vec{w}_i \quad ; i \in \{1, 2, \dots, n\} \quad (3.3.12)$$

The vectors  $\vec{\Delta x}_{1i}$  and  $\vec{\Delta x}_{0i}$  are considered to be stochastics due to measurement errors. The vector  $\vec{v}_i$  depends on the position of a marker with respect to the central marker. As this position is chosen arbitrarily,  $\vec{v}_i$  is also considered to be a stochastic vector and written as:

$$\vec{v}_i = \vec{v} + \delta \vec{v}_i \quad (3.3.13)$$

Thus, it is assumed that  $\vec{v}_i$  consists of a constant part  $\vec{v}$  and a random part  $\delta \vec{v}_i$ . Defining a deviation  $\vec{u}_i$ :

$$\vec{u}_i = \vec{w}_i + \delta \vec{v}_i \quad (3.3.14)$$

it follows from (3.3.12.):

$$\vec{\Delta x}_{1i} - F \cdot \vec{\Delta x}_{0i} - \vec{v} = \vec{u}_i \quad (3.3.15)$$

For the sake of simplicity it is assumed that the deviation  $\vec{u}_i$  is only related to the vector  $\vec{\Delta x}_{1i}$ . Further, it is assumed that the deviations are not correlated and normally distributed:

$$E(\vec{u}_i) = \vec{0} \quad (3.3.16)$$

$$E(\vec{u}_i \vec{u}_j) = \delta_{ij} \sigma^2 I \quad (3.3.17)$$

The probability density function of a set of deviations  $\vec{u}$

$$\vec{u}^T = [\vec{u}_1, \vec{u}_2 \dots \vec{u}_n] \quad (3.3.18)$$

is given by:

$$P(\vec{u}; \vec{v}, F) = (2\pi\sigma^2)^{-1.5n} e^{-\frac{1}{2\sigma^2} \sum_{i=1}^n \vec{u}_i \cdot \vec{u}_i} \quad (3.3.19)$$

From (3.3.19) estimates of  $\hat{\vec{v}}$  and  $\hat{F}$  can be determined based on the maximum likelihood method. In that case the estimates maximize  $P(\vec{u}; \vec{v}, F)$  for a given set  $\vec{u}$ . This maximum is reached when the scalar function  $J$ :

$$J = \frac{1}{n} \sum_{i=1}^n (\Delta\vec{x}_{1i} - F \cdot \Delta\vec{x}_{0i} - \vec{v}) \cdot (\Delta\vec{x}_{1i} - F \cdot \Delta\vec{x}_{0i} - \vec{v}) \quad (3.3.20)$$

is minimal. This minimum can be found by variations of  $J$  with respect to  $\vec{v}$  and  $F$ . This yields (see appendix B):

$$\hat{\vec{v}} = \Delta\vec{x}_1 - \hat{F} \cdot \Delta\vec{x}_0 \quad (3.3.21)$$

$$\hat{F} = X_{01}^c \cdot X_{00}^{-1} \quad (3.3.22)$$

where:

$$X_{00} = \frac{1}{n} \sum_{i=1}^n \Delta\vec{x}_{0i} \Delta\vec{x}_{0i} - \Delta\vec{x}_0 \Delta\vec{x}_0 \quad (3.3.23)$$

$$X_{01} = \frac{1}{n} \sum_{i=1}^n \Delta\vec{x}_{0i} \Delta\vec{x}_{1i} - \Delta\vec{x}_0 \Delta\vec{x}_1 \quad (3.3.24)$$

are tensors which describe the distribution of the markers and:

$$\Delta\vec{x}_0 = \frac{1}{n} \sum_{i=0}^n \Delta\vec{x}_{0i} \quad (3.3.25)$$

$$\Delta\vec{x}_1 = \frac{1}{n} \sum_{i=0}^n \Delta\vec{x}_{1i} \quad (3.3.26)$$

are the mean vectors of the markers in the reference configuration and in the current configuration respectively. The estimate  $\hat{\vec{v}}$  for the model error  $\vec{v}$  is not used in what follows. Its importance is, that by taking this into account, one may expect that a better estimate  $\hat{F}$  for the deformation gradient tensor  $F$  is obtained.

Notice that:

$$R(\vec{n}) = (\vec{n} \cdot X_{00} \cdot \vec{n})^{0.5} \quad (3.3.27)$$

is a measure for the distance of markers with respect to the point with the mean position vector  $\bar{x}_0$  in the direction defined by  $\vec{n}$ . If the markers are regularly distributed around the central marker,  $X_{00}$  will have a diagonal form. Besides, if the markers also occupy a circular area the diagonal terms will be nearly the same and thus  $R$  is independent of  $\vec{n}$ . In that case  $X_{00}$  may be approximately expressed as:

$$X_{00} = \frac{1}{3} \text{tr}(X_{00})I \quad (3.3.28)$$

It is easy to prove that  $\hat{F}$  is an unbiased estimate, thus  $E(\hat{F}) = F$ . Besides,  $\hat{F}$  is normally distributed. By means of  $F$ , different strain measures can be calculated. We restrict ourselves to the Green-Lagrange strain tensor, which is defined as:

$$E = \frac{1}{2} (F^C \cdot F - I) \quad (3.3.29)$$

The estimate  $\hat{E}$  is then given by:

$$\hat{E} = \frac{1}{2} (\hat{F}^C \cdot \hat{F} - I) \quad (3.3.30)$$

As  $\hat{E}$  is a non-linear function of  $\hat{F}$  it is a biased estimate. One can derive:

$$E(\hat{E}) = E + \frac{\sigma^2}{n} X_{00}^{-1} \quad (3.3.31)$$

From (3.3.31) it follows that the accuracy of the estimate  $\hat{E}$  depends, among other things, on the number of markers ( $n$ ) and their distribution ( $X_{00}$ ). In section 3.5 the accuracy of  $\hat{F}$  and  $\hat{E}$  is studied.

### 3.3.2 Strain distributions on curved surfaces

In the previous sections a method is described for the estimation of the deformation gradient tensor  $F$ . This method is generally applicable for 1-, 2-, or 3-D measurements. However, in most practical situations markers are placed on the outer surface of an object. When this outer surface is flat and does not rotate 2-D measurements are satisfactory. But, when the outer surface is curved and/or rotates the marker coordinates have to be measured in three dimensions although the strain distribution on the surface is strictly 2-dimensional. Question is, how to estimate a 2-D deformation gradient tensor  $F$  from the 3-D marker coordinates.

For that purpose two flat planes  $P_0$  and  $P_1$  are defined through a central marker in the reference and the current configuration respectively. It is assumed that all markers in the vicinity, which are used for the definition of vectors  $\Delta \vec{x}_{0i}$  and  $\Delta \vec{x}_{1i}$ , lie respectively, within these planes. Of course this assumption can only

hold for a surface which is slightly curved in the region of the group of markers used.

Consider the reference configuration. A unity vector  $\vec{n}_0$  is defined which is normal to the plane  $P_0$  (see fig. 3.3.4) and points away from the body. An arbitrary point with a position vector  $\Delta\vec{x}_0$  lies within the plane  $P_0$  if and only if:

$$(\Delta\vec{x}_0 - \Delta\vec{x}_{0s}) \cdot \vec{n}_0 = 0 \quad (3.3.32)$$

where  $\Delta\vec{x}_{0s}$  is the position vector of another arbitrary point in this plane. The unknowns  $\Delta\vec{x}_{0s}$  and  $\vec{n}_0$  have to be determined from the measured vectors  $\Delta\vec{x}_{0i}$ ;  $i \in \{1, 2, \dots, n\}$  which are the position vectors of markers with respect to the central marker. For that the

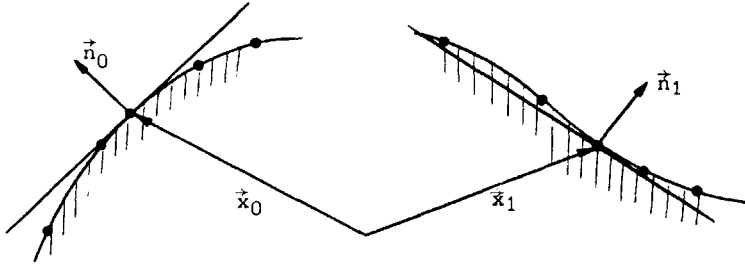


Fig. 3.3.4 Planes through a group of markers on the outer surface of a body.

method of least squares is used;  $\Delta\vec{x}_{0s}$  and  $\vec{n}_0$  are determined in such a way that:

$$J_0 = \frac{1}{n} \sum_{i=1}^n ((\Delta\vec{x}_{0i} - \Delta\vec{x}_{0s}) \cdot \vec{n}_0)^2 \quad (3.3.33)$$

is minimal with the constraint:

$$(\vec{n}_0 \cdot \vec{n}_0) = 1 \quad (3.3.34)$$

This constraint is taken into account by means of a Lagrange multiplier. The problem then becomes the determination of  $\Delta\vec{x}_{0s}$  and  $\vec{n}_0$  and a multiplier  $\lambda_0$  so that:

$$J_0^* = \frac{1}{n} \sum_{i=1}^n ((\Delta\vec{x}_{0i} - \Delta\vec{x}_{0s}) \cdot \vec{n}_0)^2 - \lambda_0 (\vec{n}_0 \cdot \vec{n}_0 - 1) \quad (3.3.35)$$

is minimal. The requirement  $\delta J_0^*$  equals zero for each variation  $\delta\lambda_0$  results in the constraint given by (3.3.34). Requiring that  $\delta J_0^*$  equals zero for each variation  $\delta\Delta\vec{x}_{0s}$  yields:

$$\Delta \vec{x}_{0s} = \frac{1}{n} \sum_{i=1}^n \Delta \vec{x}_{0i} = \Delta \vec{x}_0 \quad (3.3.36)$$

which is the mean position vector of the group of markers. Finally, the requirement  $\delta J_0^*$  equals zero for each variation of  $\vec{n}_0$  results in:

$$X_{00} \cdot \vec{n}_0 = \lambda_0 \vec{n}_0 \quad (3.3.37)$$

where  $X_{00}$  is the marker distribution tensor given by (3.3.23). As  $X_{00}$  is a symmetrical and (semi-)positive definite tensor, its eigenvalues are real and (semi-)positive. From (3.3.37) it can be seen that the desired unity vector  $\vec{n}_0$  is one of the eigenvectors of  $X_{00}$  and that the multiplier  $\lambda_0$  is the corresponding eigenvalue. This implies that  $\vec{n}_0$  and  $\lambda_0$  are not uniquely determined by (3.3.37). This is consistent with the fact that the first variation of  $J_0^*$  leads to a stationary point of  $J_0^*$ , but does not guarantee that this point is a minimum. From the three possible solutions the one that minimizes  $J_0$  has to be chosen. Substitution of (3.3.36) and (3.3.37) into (3.3.35) results in:

$$J_0^* = \vec{n}_0 \cdot X_{00} \cdot \vec{n}_0 = \lambda_0 \quad (3.3.38)$$

It is clear that  $\vec{n}_0$  is the eigenvector  $\vec{n}_{01}$  from  $X_{00}$  which corresponds to the smallest eigenvalue  $\lambda_{01}$ :

$$\lambda_0 = \lambda_{01} \leq \lambda_{02} \leq \lambda_{03} ; \vec{n}_0 = \vec{n}_{01} \quad (3.3.39)$$

For the current configuration, in the same way we obtain:

$$X_{11} \cdot \vec{n}_1 = \lambda_1 \cdot \vec{n}_1 \quad (3.3.40)$$

where  $\vec{n}_1$  is the unity vector ( $\vec{n}_1 \cdot \vec{n}_1 = 1$ ) normal to the plane  $P_1$  (see fig. 3.3.4) and  $\lambda_1$  the smallest eigenvalue of  $X_{11}$ . The tensor  $X_{11}$  is the marker distribution tensor for the current configuration:

$$X_{11} = \frac{1}{n} \sum_{i=1}^n \Delta \vec{x}_{1i} \Delta \vec{x}_{1i} - \Delta \vec{x}_1 \Delta \vec{x}_1 \quad (3.3.41)$$

where  $\vec{x}_1$  is the mean position vector given by:

$$\vec{x}_1 = \frac{1}{n} \sum_{i=1}^n \Delta \vec{x}_{1i} \quad (3.3.42)$$

It was assumed that all markers lie in the planes just established. Of course this is not the case and the next step is the projection of the marker position vectors on the planes. For the reference configuration this projection is given by:

$$\Delta \vec{x}_{0i}^* = \Delta \vec{x}_{0i} - (\Delta \vec{x}_{0i} \cdot \vec{n}_0) \vec{n}_0 \quad (3.3.43)$$

which is rewritten to:



$$\Delta \vec{x}_{0i}^* = (I - \vec{n}_0 \vec{n}_0) \cdot \Delta \vec{x}_{0i} \quad (3.3.44)$$

For the current configuration it is obtained:

$$\Delta \vec{x}_{1i}^* = (I - \vec{n}_1 \vec{n}_1) \cdot \Delta \vec{x}_{1i} \quad (3.3.45)$$

Defining  $X_{00}^*$  and  $X_{01}^*$  as:

$$X_{00}^* = \frac{1}{n} \sum_{i=1}^n \Delta \vec{x}_{0i}^* \Delta \vec{x}_{0i}^* - \Delta \vec{x}_0^* \Delta \vec{x}_0^* \quad (3.3.46)$$

$$X_{01}^* = \frac{1}{n} \sum_{i=1}^n \Delta \vec{x}_{0i}^* \Delta \vec{x}_{1i}^* - \Delta \vec{x}_0^* \Delta \vec{x}_1^* \quad (3.3.47)$$

where  $\Delta \vec{x}_0^*$  and  $\Delta \vec{x}_1^*$  are the mean vectors given by:

$$\Delta \vec{x}_0^* = \frac{1}{n} \sum_{i=1}^n \Delta \vec{x}_{0i}^* \quad (3.3.48)$$

$$\Delta \vec{x}_1^* = \frac{1}{n} \sum_{i=1}^n \Delta \vec{x}_{1i}^* \quad (3.3.49)$$

one can show, with the aid of (3.3.44) and (3.3.45), that:

$$X_{00}^* = (I - \vec{n}_0 \vec{n}_0) \cdot X_{00} \cdot (I - \vec{n}_0 \vec{n}_0) \quad (3.3.50)$$

$$X_{01}^* = (I - \vec{n}_0 \vec{n}_0) \cdot X_{01} \cdot (I - \vec{n}_1 \vec{n}_1) \quad (3.3.51)$$

where  $X_{00}$  is given by (3.3.23) and  $X_{01}$  by (3.3.24). The deformation gradient tensor  $F$  can be estimated by:

$$\hat{F} \cdot X_{00}^* = X_{01}^{*c} \quad (3.3.52)$$

As  $X_{00}^*$  is singular, a so-called pseudo-inverse is introduced for the determination of  $F$ . From (3.3.50) it follows that we may write  $X_{00}^*$  as:

$$X_{00}^* = \lambda_{02} \vec{n}_{02} \vec{n}_{02} + \lambda_{03} \vec{n}_{03} \vec{n}_{03} \quad (3.3.53)$$

where  $\lambda_{02}$ ,  $\lambda_{03}$  and  $\vec{n}_{02}$ ,  $\vec{n}_{03}$  are the eigenvalues and eigenvectors of  $X_{00}$  different from  $\lambda_0$  and  $\vec{n}_0$ . The tensor  $X_{00}^{*-1}$  defined by:

$$X_{00}^{*-1} = \frac{1}{\lambda_{02}} \vec{n}_{02} \vec{n}_{02} + \frac{1}{\lambda_{03}} \vec{n}_{03} \vec{n}_{03} \quad (3.3.54)$$

is a pseudo-inverse from  $X_{00}^*$  for which we may write:

$$X_{00}^{*-1} = (X_{00}^* + \vec{n}_0 \vec{n}_0)^{-1} - \vec{n}_0 \vec{n}_0 \quad (3.3.55)$$

and, of course:

$$X_{00}^* = (X_{00}^{*-1} + \vec{n}_0 \vec{n}_0)^{-1} - \vec{n}_0 \vec{n}_0 \quad (3.3.56)$$

Substitution in (3.3.52) gives:

$$\hat{F} \cdot (I - \vec{n}_0 \vec{n}_0) = (I - \vec{n}_1 \vec{n}_1) \cdot X_{01}^c \cdot X_{00}^{*-1} \quad (3.3.57)$$

It is not possible to determine a unique solution for  $\hat{F}$  from (3.3.57). The general solution of (3.3.57) is given by:

$$\hat{F} = (I - \vec{n}_1 \vec{n}_1) \cdot X_{01}^{*c} \cdot X_{00}^{*-1} + \vec{f} \vec{n}_0 \quad (3.3.58)$$

where  $\vec{f}$  is a vector which may be chosen arbitrarily. It describes the deformation perpendicular to the plane through the markers. Naturally, no information about this deformation can be obtained from measurements in a plane. So, only information about the deformation in plane is obtained from (3.3.58).

### 3.4 Marker identification

#### 3.4.1 Introduction

In the preceding sections a method is described to determine the Green-Lagrange strain tensor in a finite number of material points. For this it was assumed that each marker is uniquely labelled. Of course, markers do not have a label. The only feature, considered here, by which markers can be distinguished and through which a marker can be given a label, is its position. Shape and size are excluded as discriminators, at least for object markers. The distinction between control and object markers is based on the size; control markers are always much larger than object markers. It is easy to label the control markers by prescribing the way a picture is placed on the scanner (see chapter 4) and their known distribution. This will not be discussed. This section is restricted to identification of object markers.

The problem of marker identification has to be solved two times during data processing. First, by finding the same marker in the two different pictures from the differently orientated logic cameras (fig. 3.2.3). Secondly, by finding the same marker in the different states of deformation. In the following these two cases will be dealt with separately.

#### 3.4.2 Marker identification for different pictures

From each of the two different pictures corresponding to the differently orientated logic cameras a marker is chosen arbitrarily. The residual, defined by (3.2.20) (or by (A.7) if the reconstruction method based on the method of least squares is used), for this pair of markers is of the magnitude of the square of the random errors provided this pair is a correct combination, i.e. the same marker. Otherwise the residual will be of the magnitude of the square of the

distance between the image markers. When the minimal distance between the image markers is considerably larger than the measurement errors, a combination for arbitrarily chosen markers is the right one when the residual of this combination is within a properly chosen tolerance. A problem which may occur is outlined in fig. 3.4.1. When a line from a marker to one centre of projection intersects with a line from another marker to the other centre of projection (see fig. 3.4.1a, point p), the two times two image markers give four possible combinations which might have residuals that are within the

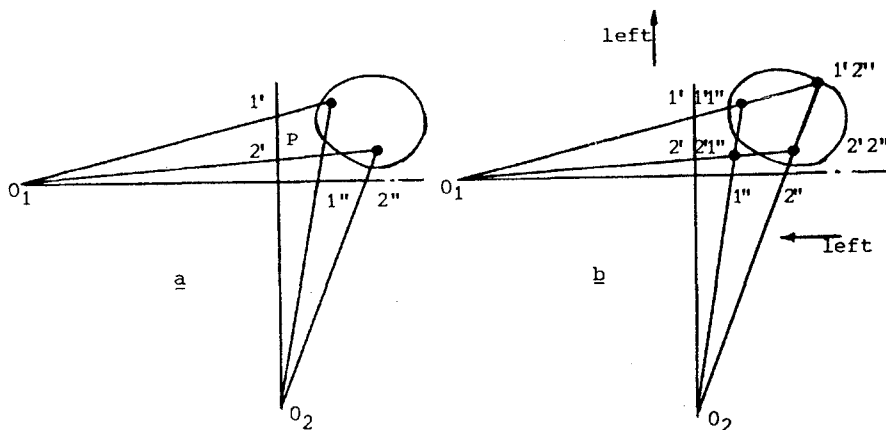


Fig 3.4.1 Two markers giving an indeterminate identification problem.

chosen tolerance (see fig. 3.4.1b). However, for markers mounted on the outer surface of an object this problem is solved by starting the identification with combinations of markers which lie on the left side in both images (or both on the right side). This is illustrated in fig. 3.4.1b. Starting from the left side, the first combination 1'-1'' gives a correct reconstruction of the coordinates of marker 1. Next, as 1'' is now labeled, combination 2'-2'' is found to be a correct one. This method has proven to be successful in practice.

### 3.4.3 Marker identification for different states of deformation

The marker identification problem when different states of deformation of the object are compared is more complex than the problem described in subsection 3.4.2. Only for the special case where (see fig. 3.4.2):

$$\|\vec{u}_i\| < \frac{1}{2} \|\Delta \vec{x}_{0ij}\|_{\min} \quad ; \quad i, j \in \{1, 2, \dots, n\} \quad (3.4.1)$$

with:

$\vec{u}_i$  : displacement vector of the centroid of the i-th marker

$\Delta \vec{x}_{0ij}$ : the vector pointing from the centroid of the i-th marker to the centroid of the j th marker

the identification problem is easily solved. The two different configurations of the body are denoted as  $C_0$  and  $C_1$ , respectively, and the position vectors corresponding to these configurations as  $\vec{x}_{0i}$  and  $\vec{x}_{1j}$ ;  $i, j \in \{1, 2, \dots, n\}$ , respectively. For the special case

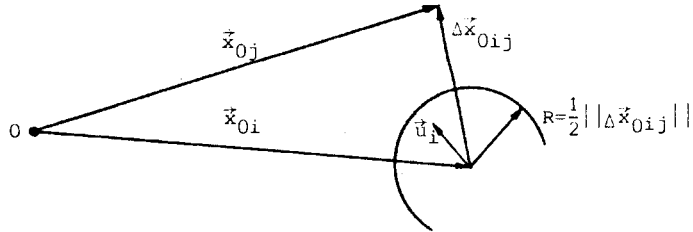


Fig. 3.4.2 The special case ( $\|\vec{u}_i\| < R$ ) for which the identification problem is easily solved.

defined by (3.4.1), the combination of vectors  $\vec{x}_{0i}$  and  $\vec{x}_{1j}$  for which  $\Delta_{ij}$  defined by:

$$\Delta_{ij} = \|\vec{x}_{1j} - \vec{x}_{0i}\| \quad (3.4.2)$$

is minimal, is a combination belonging to the same marker in the two different configurations  $C_0$  and  $C_1$ . However, the condition expressed by (3.4.1) is a very rigorous one. This is demonstrated with a simple example. A specimen applied for a uniaxial tensile test with an initial length of 100 [mm] and with a minimal marker distance of 2 [mm] may be extended no further than 1 [mm] to provide that (3.4.1) is satisfied. This corresponds with a maximum longitudinal strain allowed of 1%, which is much too small when studying soft biological tissues.

In the following a method is described for which a less stringent condition than (3.4.1) is allowed. The method has an ad-hoc character, but has proven to be effective in most practical situations. The object is to estimate the translation, rotation and deformation of the object under investigation without knowing the identity of the markers. From these estimates also estimates  $\hat{\vec{u}}_i$  for the displacements  $\vec{u}_i$  can be determined and thus estimates  $\hat{\vec{x}}_{1i}$  for the position vectors  $\vec{x}_{1i}$ .

First, two characteristic quantities of the total sets of position vectors  $\vec{x}_{0i}, \vec{x}_{1j}$ ;  $i, j \in \{1, 2, \dots, n\}$  are introduced. The mean position vectors are defined by:

$$\vec{x}_0 = \frac{1}{n} \sum_{i=1}^n \vec{x}_{0i} \quad (3.4.3)$$

$$\vec{x}_1 = \frac{1}{n} \sum_{j=1}^n \vec{x}_{1j} \quad (3.4.4)$$

and the distribution tensors by:

$$D_0 = \frac{1}{n} \sum_{i=1}^n (\vec{x}_{0i} - \vec{x}_0)(\vec{x}_{0i} - \vec{x}_0) \quad (3.4.5)$$

$$D_1 = \frac{1}{n} \sum_{j=1}^n (\vec{x}_{0j} - \vec{x}_1)(\vec{x}_{1j} - \vec{x}_1) \quad (3.4.6)$$

The translation  $\vec{u}_t$  of the object is defined as:

$$\vec{u}_t = \vec{x}_1 - \vec{x}_0 \quad (3.4.7)$$

To define a rotation it is observed that both the distribution tensors  $D_0$  and  $D_1$  are symmetrical and real. Thus, both tensors have three real eigenvalues  $\lambda_{0i}$  and  $\lambda_{1i}$  with three corresponding eigenvectors  $\vec{n}_{0i}$  and  $\vec{n}_{1i}$  respectively (Hadley, 1979). When the three eigenvalues are different then the eigenvectors are orthogonal. In general the length of an eigenvector is not of interest. For convenience, it is assumed that they are of unit length. One can prove for a rigid body movement that:

$$D_1 = R \cdot D_0 \cdot R^c \quad (3.4.8)$$

where  $R$  is a proper orthonormal tensor which describes the rotation of the object, and is given by:

$$R = \sum_{i=1}^3 \vec{n}_{1i} \vec{n}_{0i} \quad (3.4.9)$$

Notice that the direction of an eigenvector is not uniquely defined and thus  $R$  is not uniquely defined by (3.4.9). A restriction on the choice of the direction of the eigenvectors  $\vec{n}_{1i}$  is imposed which is based on practical considerations. Suppose that for each eigenvector  $\vec{n}_{0i}$  it holds:

$$\vec{n}_{0i} \cdot R \cdot \vec{n}_{0i} = \vec{n}_{0i} \cdot \vec{n}_{1i} > \cos \frac{\pi}{4} \quad (3.4.10)$$

then it also holds:

$$\vec{n}_{0i} \cdot R \cdot \vec{n}_{0j} = \vec{n}_{0i} \cdot \vec{n}_{1j} < \cos \frac{\pi}{4} \quad j \neq i \quad (3.4.11)$$

In words; when the rotation of a rigid body is such that the angle between the similar eigenvector in the two considered configurations is always smaller than  $\frac{\pi}{4}$  [rad], then the angles between this eigenvector in one configuration and the other two eigenvectors in

the other configuration are always larger than  $\frac{\pi}{4}$ [rad]. If (3.4.10) is elevated as a requirement it is, by that, also a criterion to define R uniquely. This requirement is, from a practical point of view, very reasonable; rotations will be, in general, much smaller.

In the previous, the translation vector  $\vec{u}_t$  and the rotation tensor R are defined for a rigid body movement. However, the present thesis deals with deforming objects for which the part of the movement that is considered as rigid can be defined in many ways. Here, rigid body movement for a deforming object is defined analogous to real rigid body movement given by (3.4.7) and (3.4.9). Notice that (3.4.8) does not hold for a deforming object. The relation between the position vectors of a marker in two configurations  $C_0$  and  $C_1$  is defined by:

$$\vec{x}_{1i} = R \cdot (\vec{x}_{0i} - \vec{x}_0) + \vec{x}_1 + \vec{u}_{1j} \quad (3.4.12)$$

where  $\vec{u}_{1j}$  represent the displacement vectors due to the deformation of the body. Using (3.4.3) and (3.4.4) it follows that:

$$\vec{u} = \frac{1}{n} \sum_{i=1}^n \vec{u}_{1i} = \vec{0} \quad (3.4.13)$$

Neutralization of the rotation and translation gives:

$$\vec{x}_{0i} = R^{-1} \cdot (\vec{x}_{1i} - \vec{x}_1) + \vec{x}_0 - R^{-1} \cdot \vec{u}_{1i} \quad (3.4.14)$$

With:

$$\vec{x}'_{0i} = R^{-1} \cdot (\vec{x}_{1i} - \vec{x}_1) + \vec{x}_0 \quad (3.4.15)$$

$$\vec{u}_{0i} = R^{-1} \cdot \vec{u}_{1i} \quad (3.4.16)$$

(3.4.14) is rewritten to:

$$\vec{x}_{0i} = \vec{x}'_{0i} - \vec{u}_{0i} \quad (3.4.17)$$

As  $\vec{x}_0$ ,  $\vec{x}_1$  and R can be determined the position vectors  $\vec{x}'_{0i}$  can also be determined. The position vectors  $\vec{x}'_{0i}$  are said to correspond to a virtual configuration  $C'_0$  which differs from  $C_0$  due to a deformation of the body. To attain that corresponding markers come sufficiently close, neutralization of the rotation and translation is not sufficient. In addition it is necessary to estimate the displacement  $\vec{u}_{0i}$  in equation (3.4.17). The method described below is restricted to markers which are placed on slightly curved outer surfaces. First, it is noticed that the distribution tensor  $D_0$  is similar to the marker distribution tensor  $X_{00}$  defined by (3.3.23). Secondly, it is observed that the deformation of a surface is strictly 2-dimensional. To estimate this 2-dimensional deformation from the 3-dimensional marker coordinates, a flat plane  $P_0$  through  $\vec{x}_0$  is defined according to the theory described in section 3.3.2. Let the eigenvalues  $\lambda_{0i}$  of  $D_0$  be

arranged according to their magnitude as  $\lambda_{01} < \lambda_{02} < \lambda_{03}$ . Then  $\vec{n}_{01}$  is the unit normal vector on the plane  $P_0$ . The marker position vectors  $\vec{x}_{0i}$  and  $\vec{x}'_{0i}$  are now projected on this plane:

$$\vec{x}_{0i}^* = \vec{x}_{0i} - (\vec{x}_{0i} \cdot \vec{n}_{01}) \vec{n}_{01} \quad (3.4.18)$$

$$\vec{x}'_{0j} = \vec{x}'_{0j} - (\vec{x}'_{0j} \cdot \vec{n}_{01}) \vec{n}_{01} \quad (3.4.19)$$

The eigenvectors  $\vec{n}_{02}$  and  $\vec{n}_{03}$  form a base for the plane  $P_0$  with the origin at  $\vec{x}_0$  and constitute four quadrants. Both for  $\vec{x}_{0i}^*$  and  $\vec{x}'_{0j}^*$ , the mean position vectors of markers within a quadrant can be calculated. The two times four mean position vectors are given by (see fig. 3.4.3):

$$\langle \vec{x}_0^* \rangle_k = \frac{1}{n_k} \sum_{i=1}^{n_k} \vec{x}_{0i}^* \quad ; \quad k \in \{1, \dots, 4\} \quad (3.4.20)$$

$$\langle \vec{x}'_0^* \rangle_m = \frac{1}{n_m} \sum_{j=1}^{n_m} \vec{x}'_{0j}^* \quad ; \quad m \in \{1, \dots, 4\} \quad (3.4.21)$$

where  $n_k$  and  $n_m$  are the number of markers in the four quadrants corresponding to the configurations  $C_0^*$  and  $C_0'^*$ . These mean position

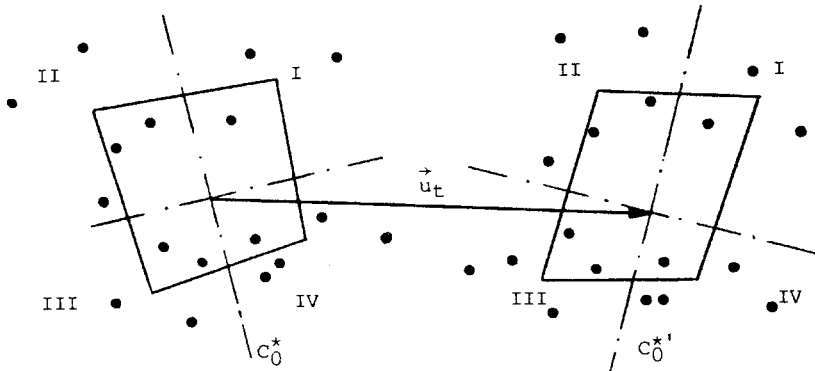


Fig. 3.4.3 The mean position vectors from markers within a quadrant and the 4-node element defined from these vectors.

vectors may be considered to be the nodes of a 4-node element (Zienkiewicz, 1979) in the undeformed ( $C_0^*$ ) and in the deformed state ( $C_0'^*$ ). From a standard calculation (analogous to the method to correct for systematic errors belonging to image coordinates; see section 3.5) estimates  $\vec{u}_j^*$  for the displacements:

$$\vec{u}_j^* = \vec{u}_j - (\vec{u}_j \cdot \vec{n}_{01}) \vec{n}_{01} \quad (3.4.22)$$

can be obtained and from these, estimates  $\hat{x}_{0j}^*$  given by:

$$\hat{x}_{0j}^* = \vec{x}_{0j}^* - \hat{u}_j^* \quad (3.4.23)$$

for the position vectors  $\vec{x}_{0j}^*$ . The position vectors  $\hat{x}_{0j}^*$  are said to correspond to a virtual configuration  $\hat{C}_0^*$  which is an estimate for the configuration  $C_0^*$ . It may be expected, at least for most practical situations, that the estimates  $\hat{x}_{0j}^*$  are good enough to apply a criterion similar to (3.4.1) for marker identification. Thus, the combination of position vectors  $\vec{x}_{0i}^*$  and  $\hat{x}_{0j}^*$  for which  $\Delta_{ij}^*$  defined by:

$$\Delta_{ij}^* = ||\vec{x}_{0j}^* - \vec{x}_{0i}^*|| \quad (3.4.24)$$

is minimal, may be considered as a combination belonging to the same marker in the two different configurations  $C_0^*$  and  $\hat{C}_0^*$ . The estimates  $\hat{x}_{0j}^*$  can be improved by using an iterative process. In that case the last obtained estimates  $\hat{x}_{0j}^*$  serve as the coordinates for new mean position vectors  $(\vec{x}_0^*)_m$ . This will not be discussed in more detail.

In the foregoing a method is described to identify markers from different deformed configurations of an object. Although this method does not guarantee that the identification problem is always solved correctly, it has proven to be effective and reliable in practice.

### 3.5 Error Analysis

#### 3.5.1 Calibration and correction of systematic errors

In the previous sections it was assumed that the image plane coordinates contain only random errors. However, between the transformation of the object space to the image plane and the final reconstruction of the spatial marker coordinates several operations are carried out on the image, giving rise to both random and systematic errors. This section deals with systematic errors.

The important features of the method for correction of systematic errors described in this section are:

- a black box approach, thus all types of errors are described with the same mathematical model.
- this mathematical model governs both correction and calibration at the same time.
- correction and calibration are carried out for each image separately.
- the method allows for the use of cheap standard components for the experimental set-up.
- the camera constant  $c$  need not to be known and accurate knowledge of the camera distance  $a$  is not required.



The errors due to deviations from the desired orientations and positions of the image planes can be derived in a straightforward manner from the physical cause of the error (see appendix C). For sources of errors such as lens distortion and (non-uniform) film shrinkage when photo- or ciné cameras are used, or geometric distortions of TV and Video systems, this is very laborious, if not impossible. Besides, if standard image recording systems are used it is difficult to alter the total set-up, so there is no need for physically based models from the point of view of design. A common approach to model these types of errors is the application of polynomials of the form:

$$\begin{bmatrix} \delta x_{i2} \\ \delta x_{i3} \end{bmatrix} = \begin{bmatrix} a_{i0} \\ a_{i20} \end{bmatrix} + \begin{bmatrix} a_{i11} & a_{i12} & a_{i13} & \cdots \cdots \cdots \\ a_{i21} & a_{i22} & a_{i23} & \cdots \cdots \cdots \end{bmatrix} \cdot \begin{bmatrix} x_{i2} \\ x_{i3} \\ x_{i2}x_{i3} \\ x_{i2}^2 \\ \cdot \\ \cdot \\ \cdot \end{bmatrix} \quad (3.5.1)$$

where  $i \in \{1, 2\}$  stands for the image plane concerned. The number of terms of the polynomials depend on the desired accuracy. As both, errors as a result of deviations of orientation and position of the image planes and errors due to lens distortion are taken into account with a similar model (see appendix C) one can superpose the first on to the second. For calibration and correction of the image plane coordinates control markers in the object space can be applied. Control markers have a fixed accurately known position in the object space. With the aid of these markers the exact values of the parameters governing the collinearity equations (3.2.1) and the coefficients in equation (3.5.1) can be established. Images captured after that, then can be calibrated and corrected provided that image transformations, whatever they may be, are that stable in time that remaining disturbances are within the range of the allowed random errors. In case of relatively precise strain measurements whereby cheap standard components are applied for the experimental set-up this is certainly not true. Calibration and correction has to be done for each image separately. Thus, besides the object which is investigated, each image must also contain a representation of a calibration object in addition. In view of the relatively small observation volume this gives no insurmountable practical drawbacks as concerned to costs, tractability and the location of the control points with the necessary accuracy.

As images are calibrated and corrected separately before the 3-D-reconstruction is performed, in the following only one image is considered (image plane 1, fig. 3.2.3). The model describing the

image coordinate errors (3.5.1) will first be written in a more convenient form. For that purpose a principal plane is introduced (see fig. 3.5.1) with normalized coordinates  $(\xi, \eta)$  which are chosen

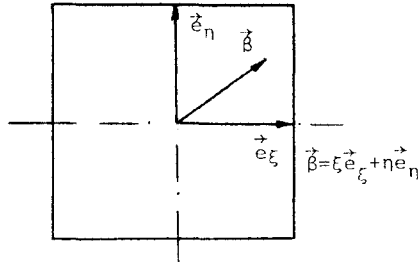


Fig. 3.5.1 Principal plane with the natural coordinates  $\xi$  and  $\eta$ .

in such a way that on the faces of this finite and bounded plane their values are  $\pm 1$ , thus:

$$-1 \leq \xi \leq +1 \quad (3.5.2)$$

$$-1 \leq \eta \leq +1 \quad (3.5.3)$$

Consider an arbitrarily deformed rectangle in the image plane (see fig. 3.5.2). Assume that there exists a one-to-one transformation from the principal plane to the deformed plane.

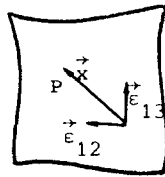


Fig. 3.5.2 A deformed rectangle in the image plane.

Then for an image vector  $\vec{x}$  corresponding to a point P in the deformed plane it is written:

$$\vec{x} = \vec{x}(\xi, \eta) \quad (3.5.4)$$

This last assumption is always true when the determinant of the Jacobian tensor J defined by  $(\vec{\beta})$  is defined in fig. 3.5.1):

$$J = \left( \frac{\partial \vec{x}}{\partial \vec{\beta}} \right)^c \quad (3.5.5)$$

has a positive sign for every vector  $\vec{x}$  within the deformed rectangle. It will be clear that a rectangular image plane can be distorted (deformed) due to all kinds of errors in the optical system. To correct for this distortion a number of control markers are placed in view of the camera from which the "exact" position in 3-Dimensional space is known. So the distortions of these control markers can be measured. The problem is, how to derive the distortion of other points from those of the control markers. A quite general and flexible method, frequently chosen to describe the geometrical transformation given by (3.5.4) is the application of shape functions  $N_i(\xi, \eta)$ ;  $i \in \{1, \dots, n\}$ : (Zienkiewicz, 1979). For (3.5.4) it is possible to write:

$$\vec{x} = \sum_{i=1}^n N_i(\xi, \eta) \vec{x}_{ci} \quad (3.5.6)$$

where  $\vec{x}_{ci}$  are the image plane vectors of a number of control markers. The exact form of the shape functions depends on the number and configuration of the control markers. For both the exact as well as the measured image plane coordinates of all markers the same transformation, defined by (3.5.6) is chosen. By defining  $\vec{x}^*$  as a measured position vector of a marker with  $\vec{x}$  as its exact position vector, the distortion  $\delta\vec{x}$  is given by:

$$\delta\vec{x} = \vec{x}^* - \vec{x} \quad (3.5.7)$$

From the above it follows that:

$$\vec{x}^* = \sum_{i=1}^n N_i(\xi, \eta) \vec{x}_{ci}^* \quad (3.5.8)$$

$$\delta\vec{x} = \sum_{i=1}^n N_i(\xi, \eta) \delta\vec{x}_{ci} \quad (3.5.9)$$

The shape functions determine the "error-model". From the measured coordinates of object and control markers a set of normalized coordinates  $(\xi, \eta)$  can be found and when the exact image coordinates

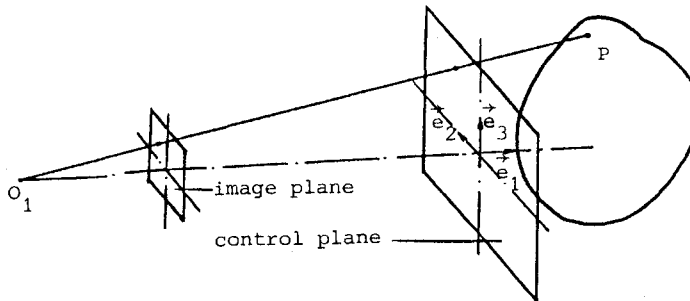


Fig. 3.5.2 Definition of the control plane for image plane.

of the control markers are known then the corrected image coordinates for each marker can be obtained with the aid of (3.5.6).

In practice, it is impossible to determine the exact image coordinates  $\vec{x}_{ci}$  of the control markers (3.5.6). For that reason a special choice is made for the distribution of the control markers in the object space. All the control markers lie in the plane spanned by  $\vec{e}_2$  and  $\vec{e}_3$  (see fig. 3.5.2). This plane is called the control plane. The position vectors of the control points are denoted by  $\vec{x}_{ci}$ ; ie (1...n) where n is the number of control points. The exact transformation from a control point to the image plane is given by (see fig. 3.5.2):

$$\vec{x}_{ci} = \frac{c}{a} \vec{x}_{ci} \quad (3.5.10)$$

Substitution of (3.5.10) in (3.5.6) leads to:

$$\frac{a}{c} \vec{x} = \sum_{i=1}^n N_i(\xi, \eta) \vec{x}_{ci} \quad (3.5.11)$$

For  $c = a$  (3.5.11) yields:

$$\vec{x} = \sum_{i=1}^n N_i(\xi, \eta) \vec{x}_{ci} \quad (3.5.12)$$

In (3.5.12)  $\vec{x}$  is the position vector of an object marker transformed to the control plane. This is a transformation to an image plane for which  $c = a$ . The method for coordinate reconstruction described in section 3.2.2 is based on this imaginary image plane. Summarizing:

- from measured, real image coordinates of object and control markers a set of normalized coordinates  $(\xi, \eta)$  can be determined
- next with (3.5.12) the corrected coordinates  $\vec{x}$  can be obtained.

The determination of the set of normalized coordinates  $(\xi, \eta)$  from (3.5.8) can usually not be done directly as the shape functions are, non-linear with respect to the normalized coordinates (for more than two control points). However it is fairly simple to calculate  $\xi$  and  $\eta$  iteratively.

The method for calibration and correction described here has several advantages. First, it is not necessary for the camera constant  $c$  to be known or constant. Secondly, as a result of the chosen form for the error-model the coefficients  $a_{ij}$ ,  $b_{ij}$  of (3.5.1) need not to be determined. Further the model is able to describe all kinds of transformations depending on the choice of the shape functions. Shape functions are known for a large number of different distributions of the control markers.

Finally, it is important to notice that the machining of the control object does not have to be done very accurately; accurate measuring of the coordinates of the control points after the machining is sufficient.

There are also some disadvantages. By choosing the control markers in a plane perpendicular to the optical axis full correction is not possible for deviations of  $\delta\vec{X}_0$ . The errors resulting from these deviations are a function of the real marker position  $\vec{X}$  (see appendix C). For  $c=a$  the image coordinate errors are noted as  $\delta x_{ij}$ . For the partial errors, which are a function of the object space coordinates  $X_i$ , we note  $\delta x_{ij}^*$  and from (C.22) we may write:

$$\delta x_{ij}^* = -\frac{a}{X_i + a} \delta X_{0j} + \frac{X_{ij}}{X_i + a} \delta X_{0i} \quad (3.5.13)$$

If  $a \gg X_i$  this can be rewritten as:

$$\delta x_{ij}^* = -\delta X_{0j} + \frac{X_{ij}}{a} \delta X_{0i} + \frac{X_i}{a} \delta X_{0j} - \frac{X_{ij}X_i}{a^2} \delta X_{0i} \quad (3.5.14)$$

For the first two terms on the right hand side of (3.5.14) a correction is accomplished because they are not a function of the object space marker coordinates  $X_i$ . The error represented by the third term is not corrected. The magnitude can be affected by three factors:

- by placing the object under investigation closer to the control plane ( $X_i$  small).
- by increasing the camera distance  $a$
- by raising the accuracy with which the position of the centre of projection is realized.

The last term on the right hand side of (3.5.14) is also not corrected. However, if  $X_i \ll a$  this term is much smaller than the third one and may be neglected.

A large camera distance, relative to the object size ( $X_i$ ), decreases the error in the reconstruction coordinates which results from the

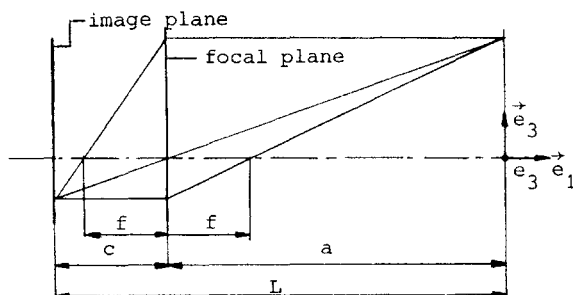


Fig. 3.5.3 Definition of L.

error introduced by using an estimate  $\hat{a}$  for the camera distance  $a$ . A first guess for  $\hat{a}$  is easily obtained from the experimental set-up. As the position of the image plane is usually marked on the outside of a camera one can measure the distance  $L$  (see fig. 3.5.3) between image

plane and the origin of the object space coordinate system. The focal length  $f$  is given for a lens-system. If  $L$  and  $f$  are known it is possible to determine  $a$  with the aid of the lens formula:

$$\frac{1}{f} = \frac{1}{a} + \frac{1}{c} \quad (3.5.15)$$

One can derive, noticing that  $c = L - a$ :

$$a = \frac{L}{2} \left( 1 + \left( 1 - \frac{4f}{L} \right)^{1/2} \right) \quad (3.5.16)$$

This first guess is often good enough, but, if necessary a better estimate for the camera distance can be established by a repeated reconstruction of the coordinates of two markers from which the mutual distance is accurately known. Hereby  $a$  is varied around the value of the first guess. The camera distance used in the reconstruction which gives the best estimate for the marker distance can be regarded as the real camera distance.

Formula (3.5.16) is based on the assumption that the camera is focused on the control plane. However, from a practical point of view it is more likely that the camera is focused on a plane somewhere between control plane and object. Noting the distance between control plane and plane of focusing as  $d_f$ , the estimated camera distance obtained from (3.5.16) should be corrected for (see Appendix D):

$$\delta a = \left( \frac{c}{f} - 1 \right)^2 d_f \quad (3.5.17)$$

So, if  $c$  and  $f$  are nearly of the same magnitude, which is true for a large camera distance, the influence of focusing of the camera distance may be neglected.

### 3.5.2 Statistical properties of the deformation gradient tensor $F$ and the Green-Lagrange strain tensor $E$

In order to make statements about the accuracy with which the components of  $\hat{F}$  are estimated and test hypotheses about the occurring deformation field, expressions have to be derived for the variances of these components and covariances between these components. Notice that, although vector and tensor notation is used, expressions are similar to those found in literature on experimental design theory. First, an estimate  $\hat{\sigma}^2$  for the variance  $\sigma^2$  of  $\vec{u}$  will be derived. For that purpose the unexplained variation  $V_u$  which is defined as:

$$V_u = \sum_{i=1}^n (\Delta \vec{x}_i - \hat{\Delta \vec{x}}_i) \cdot (\Delta \vec{x}_i - \hat{\Delta \vec{x}}_i) \quad (3.5.18)$$

is considered. After a straightforward calculation this is transformed to (see appendix E):

$$V_u = n(I : X_{11} - \hat{F}^C \cdot \hat{F} : X_{00}) \quad (3.5.19)$$

The first term  $I:X_{11}$  is called the total variation  $V_T$ , the second one  $\hat{F}^C \cdot \hat{F}:X_{00}$  the explained variation  $V_e$ . The number of degrees of freedom of  $V_T$  is equal to the number of measured vector components. When the dimension of the experiment is  $D$ , the number of degrees of freedom is  $nD$ . The number of degrees of freedom of the explained variation is equal to the number of the components of  $\hat{F}\hat{F}$  and  $\hat{V}$ , thus  $D^2 + D$ . So, the number of degrees of freedom for the unexplained variation equals  $(n-D-1)D$ . It can be proved (Doornbos, 1980) that for the expected value of  $V_u$  the following expression holds:

$$E(V_u) = (n-D-1)D\sigma^2 \quad (3.5.20)$$

This gives an unbiased estimate for  $\sigma^2$ :

$$\hat{\sigma}^2 = \frac{V_u}{(n-D-1)D} \quad (3.5.21)$$

As  $\frac{V_u}{\sigma^2}$  has a  $\chi^2$ -distribution with  $(n-D-1)D$  degrees of freedom it is possible to establish confidence intervals for  $\sigma^2$  with the aid of statistical tables.

For the determination of confidence intervals for the components of  $\hat{F}$  it is necessary to derive an expression for the variance-covariance tensor of  $\hat{F}$ . This tensor is defined as:

$${}^4C = E[(\hat{F}^C - F^C)(\hat{F} - F)] \quad (3.5.22)$$

In appendix F it is shown that:

$${}^4C = \frac{\sigma^2}{n} X_{00}^{-1} \cdot \left( \frac{1}{n} \sum_{i=1}^n \Delta \vec{x}_{0i} I \Delta \vec{x}_{0i} - \Delta \vec{x}_0 I \Delta \vec{x}_0 \right) \cdot X_{00}^{-1} \quad (3.5.23)$$

The variance of a component  $\hat{F}_{ij}$  of  $\hat{F}$  is given by the component  $C_{ijij}$  of  ${}^4C$ , the covariance between two components  $\hat{F}_{ij}$  and  $\hat{F}_{kl}$  by the component  $C_{ijkl}$  of  ${}^4C$ . The correlation coefficient between two components  $\hat{F}_{ij}$  and  $\hat{F}_{kl}$  is defined as:

$$\rho(\hat{F}_{ij}, \hat{F}_{kl}) = \frac{C_{ijkl}}{(C_{jijj} C_{klkl})^{1/2}} \quad (3.5.24)$$

The components of  ${}^4C$  with respect to an orthonormal vectorbase  $\vec{n}_i$ ;  $i \in \{1, 2, 3\}$  follows from:

$$C_{ijkl} = ((({}^4C \cdot n_l) \cdot n_k) \cdot n_j) \cdot n_i \quad (3.5.25)$$

which yields:

$$C_{ijkl} = \frac{\sigma^2}{n} (X_{00}^{-1})_{ii} \delta_{jk} \quad (3.5.26)$$

From (3.5.26) it follows:

$$\text{var}(\hat{F}_{ij}) = \frac{\sigma^2}{n} (X_{00}^{-1})_{jj} \quad (3.5.27)$$

$$\text{cov}(\hat{F}_{ij}, \hat{F}_{ik}) = \frac{\sigma^2}{n} (X_{00}^{-1})_{jk} \quad (3.5.28)$$

$$\text{cov}(\hat{F}_{ij}, \hat{F}_{kl}) = 0 \quad ; i \neq k \quad (3.5.29)$$

Thus, only those components of the deformation gradient tensor  $\hat{F}$  which contribute to deformations in the direction of one of the base vectors are correlated.

As stated before the components  $\hat{F}_{ij}$  are unbiased estimates of the components  $F_{ij}$  and they have a normal distribution. Denoting:

$$\sigma^2 (\hat{F}_{ij}) = \sigma^2 (X_{00}^{-1})_{jj} \quad (3.5.30)$$

than:

$$\frac{\hat{F}_{ij} - F_{ij}}{\sigma(\hat{F}_{ij})} \quad (3.5.31)$$

has a  $N(0,1)$  distribution. Replacing  $\sigma(\hat{F}_{ij})$  by its estimate given by:

$$\hat{\sigma}(\hat{F}_{ij}) = \hat{\sigma}^2 (X_{00}^{-1})_{jj} \quad (3.5.32)$$

which has a  $\chi^2$ -distribution (3.5.21) with  $\nu = (n-D-1)D$  degrees of freedom than:

$$\frac{\hat{F}_{ij} - F_{ij}}{\hat{\sigma}(\hat{F}_{ij})} \quad (3.5.33)$$

has a student t-distribution (Doornbos, 1980) with  $\nu$  degrees of freedom. Again, with the aid of statistical tables one can establish confidence intervals for the components  $F_{ij}$ .

Finally, the variance-covariance tensor of  $\hat{E}$  as is defined:

$${}^4L = E[(\hat{E} - E)(\hat{E} - E)] \quad (3.5.34)$$

A lengthy but straightforward calculation (see appendix G) yields for the components of L:

$$L_{klmn} = \frac{\sigma^2}{4n} [F_{pk}F_{pm}(X_{00}^{-1})_{ln} + F_{pk}F_{pn}(X_{00}^{-1})_{ml} + F_{pl}F_{pn}(X_{00}^{-1})_{km} + F_{pl}F_{pm}(X_{00}^{-1})_{kn}] \quad (3.5.35)$$

Hereby the higher order terms are neglected. This tensor cannot be applied for the determination of confidence intervals for the



components  $E_{ij}$  as  $\hat{E}$  is a biased estimate and so the statistical meaning of  ${}^4L$  is not clear. However, the variance-covariance tensor  ${}^4L$  gives us a reasonable insight in the accuracy properties of  $\hat{E}$ . Besides it can be used for experimental design because the influence of different parameter on this accuracy properties is expressed in  ${}^4L$ .



---

 4. STRAIN DISTRIBUTION MEASUREMENT: THE EXPERIMENTAL SET-UP
 

---

## 4.1 INTRODUCTION

In this chapter the design and testing of the experimental set-up for the measurement of strain distributions are discussed.

It is important to notice that the accuracy is not only determined by the measuring system, but also by factors which are specific for each individual experiment. As in literature these factors are usually not mentioned explicitly, it is unfeasible to compare the reported accuracies in a proper way.

The design process mainly is based on the theoretical results derived in chapter 3. The most important design requirements and restrictions imposed upon the set-up are:

- the set-up has to be suitable for measuring strain distributions on the outer surface of slightly curved objects, which are allowed to rotate and have a maximum size of 60 x 20 [mm].
- application of an ordinary photo camera in combination with a scanner for the discretization and digitizing of the captured pictures.
- a standard deviation of 0.001 for the principal strains of a 2-dimensional homogeneous strain field.

The latter is based on the definition of a standardized group of object markers (fig. 4.1.1). This group consists of nine circular markers in a flat plane. It is called the standard strain group. Note that the model error  $\vec{v}$  (see (3.70)) equals zero for a homogeneous strain field.

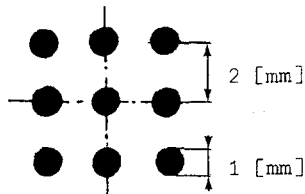


Fig. 4.1.1 Definition of the standard strain group (n=8).

From these requirements and with the aid of the theory described in chapter 3 the following properties for the set up have been derived (appendix H):

- scan resolution :  $p \geq 20$  [pix/mm]
- number of pixels :  $\geq 1750 \times 2500$  [pix<sup>2</sup>]
- camera distance :  $a > 840$  [mm]
- number of control markers :  $n = 12$  [ctrl mrk/plane]

Notice that the scan resolution is given as the number of pixels per millimeter measured in the object space. If the magnification factor

of a picture is denoted as  $m$  the resolution  $p_s$  of the applied scan apparatus is given by:

$$P_s = p/m \quad (4.1.1)$$

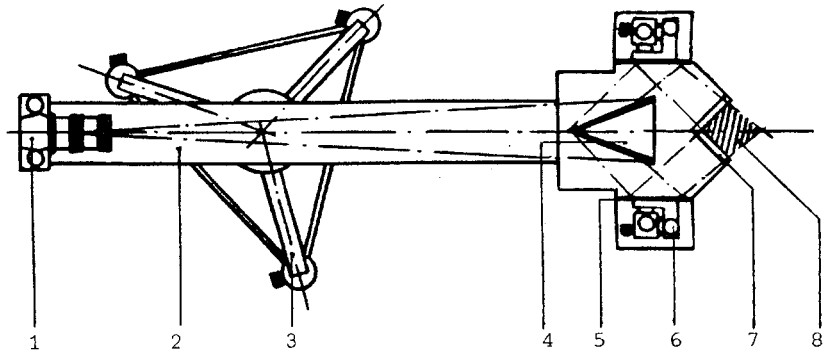
In the next section the experimental set-up is described. A mirror system is applied (Erdman et al., 1979) to obtain two views on one single picture. In section 4.2.2 the successive data processing steps, which have to be executed to find the desired strains are shortly described.

Next, in section 4.2.3 several aspects with regard to the accuracy of the strain measurements will be discussed. The last section deals with test measurements. Attention is paid to the different aspects related to accuracy which are discussed in the present and the previous chapter.

#### 4.2 THE EXPERIMENTAL SET-UP

##### 4.2.1 The optical system

A top-view of the optical system is given in fig. 4.2.1. Only one physical camera together with a mirror system is used. In this way two logical cameras are constituted. This has the advantage that synchronization of camera shutters is not necessary and that the



- |                  |                    |
|------------------|--------------------|
| 1 camera         | 5 side mirror      |
| 2 optical bench  | 6 mirror adjustor  |
| 3 tripod         | 7 control frame    |
| 4 central mirror | 8 measuring volume |

Fig. 4.2.1 The optical system (top view).

set-up is more compact than a set-up with two camera's (fig. 4.2.2).

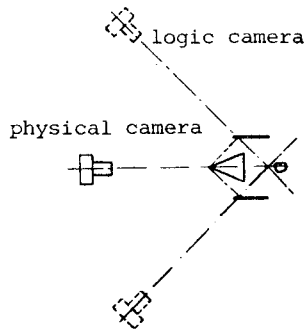


Fig 4.2.2 A set-up with one physical camera together with a mirror system.

Camera, mirror system and control frame are mounted on an optical bench. The bench is mounted on a movable tripod by means of a ball-joint. This makes it simple to place the set-up near the object. The positions of the side mirrors are adjustable so the logic camera's can be brought into the correct positions. In table 4.2.1 the technical data of the strain measurement system are summarized.

Table 4.2.1

Technical data of the strain measurement system.

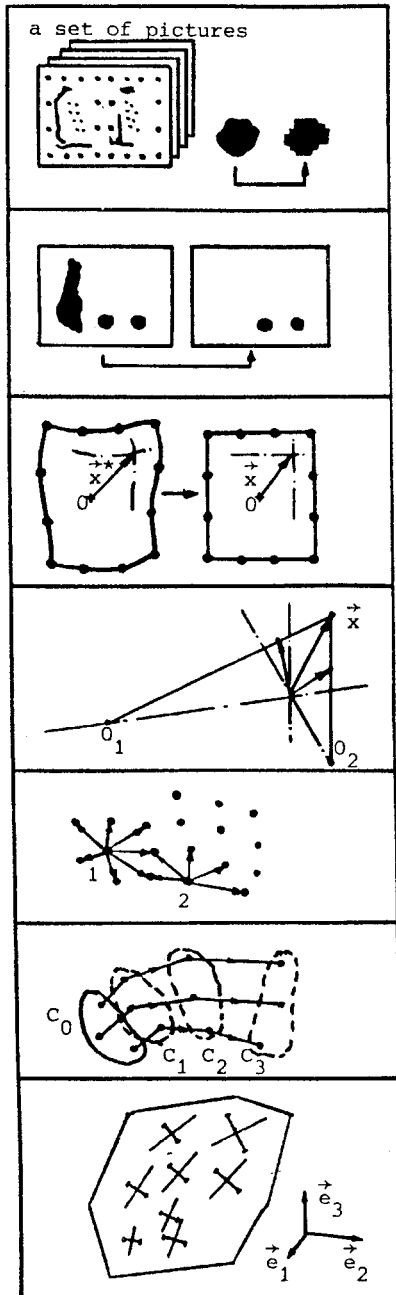
---

camera body	: Nikon F2A
lens system	: Nikon Nikkor (f= 105 [mm]) Panagor auto tele convertor (2x), polarisation filter
focal distance	: 210 [mm]
camera distance	: 910 [mm]
film	: Agfa-ortho 25 professional (35 [mm])
measuring volume	: 70 x 50 x 50 [mm]
number of control markers	: 12 for each control plane
diameter control markers	: 2 [mm]
scanner	: FIT-PS Perscan (2048 x 3360 [pix], 10[pix/mm]), two grey-levels
host computer	: IBM PC-XT; extensions: Tecmar captain board, Tecmar graphic master board, Microsoft mouse

---

#### 4.2.2 Data processing

In this section a brief description of the data processing is given. A review of this process is given in fig. 4.2.3. After a set of pictures is captured these pictures are scanned (discretization). Image data are stored as sets of three numbers {i, j, k} which define each an adjoining row of black pixels (fig. 4.2.4).



## Scanning

- discretization of the pictures

Scan image file

## Marker detection

- automatic and manual removal of noise
- marker centroid determination

## Correction

- correction of coordinates according to the theory described in section 3.5

## Identification and 3-D reconstruction

Coordinate file

## Strain group definition

## Marker identification

## Strain calculation

- choice of reference and current state
- graphical output.

Strain file

Fig. 4.2.3 A review of the data processing.

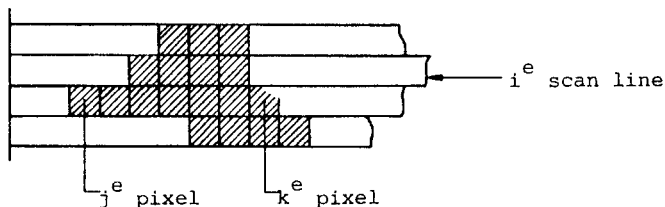


Fig. 4.2.4 Designation of an adjoining row of black pixels.

The image data will not only contain information from the markers but also from black parts of the background (background noise). Separation of the markers and noise, the marker detection, is done as follows:

- Starting from the first scan line, groups of connected adjoining rows of black pixels are detected. Such a group forms a black area.
- Based on a set of area descriptors, which will be defined below, it is automatically decided whether the area must be recognized as a marker.
- After that the marker centroid is computed the data which describe the treated area are excluded from the image data.
- The detection is continued on the scan line where the first black pixel row of the last treated area is found.

The area descriptors used for the marker detection are the following:

- Area size: The number of pixels an area consists of.
- Slenderness: The ratio of the maximum dimensions of the area measured in the direction of the scan lines and perpendicular to this direction.
- The number of branches.

The concept of a branch is defined as follows:

Each row of black pixels belonging to an area is labelled with a number  $i$ ;  $i \in \{1, 2, \dots, n\}$ . When a row is connected with  $m_i$  other rows, the number of branches  $k_i$  of that row is given by:

$$k_i = 0 \quad \text{when } m_i = 0, 1 \quad (4.2.1)$$

$$k_i = m_i \quad \text{when } m_i \geq 2$$

The number of branches  $k_b$  of an area is defined as:

$$k_b = \sum_{i=1}^n k_i \quad (4.2.2)$$

To illustrate the concept of branches some examples of areas with the corresponding number of branches are given in fig. 4.2.5.

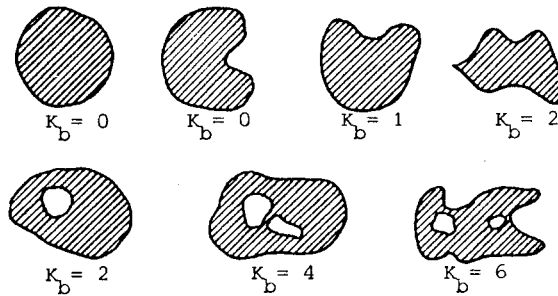


Fig. 4.2.5 Examples of areas with the corresponding number of branches.

By choosing appropriate limitations for the mentioned descriptors most of the background noise is automatically eliminated. For the noise that is left a visual control is carried out and this noise is removed manually.

Correction, identification and 3-D reconstruction are done according to the theory described in chapter 3.

Which markers are considered as central markers and which markers belong to the corresponding strain groups is a matter of selection. Insight in the actual experiment has to lead to a reasonable choice of the strain groups. It is allowed to define different strain groups for the same central marker. In this way the influence of the choice of a strain group can be investigated.

The identification and labeling of markers in the different configurations of the object under investigation is done as described in section 3.4.3.

After definition of the reference and current state, strains are calculated according to the theory described in chapter 3 section 3.3. For each strain group all characteristic properties, as defined in chapter 3, are available. For a graphical representation of the results the principal strains and corresponding eigenvectors are determined. They can be presented on screen as a 3-D vector plot. The object may be composed as a wire frame by drawing lines, at choice, between markers. Also, software was developed for postprocessing.

#### 4.2.3 Aspects of accuracy

As stated in the introduction, accuracy is not only determined by the set-up but also influenced by factors specific for each individual experiment. The standard strain group is meant as a tool for design and as a guide for what may be expected and what is possible. The accuracy which can be obtained in practice will generally be different. The present section consists of two parts. The first part



deals with means to control the accuracy. In the second part the interpretation of the measured strain distributions, with respect to accuracy, is discussed.

control of the accuracy

It is noted that the variances of both the components of the deformation gradient tensor  $F$  (3.5.27) and the Green-Lagrange strain tensor  $E$  (3.5.35) are mainly governed by the factor:

$$\frac{\sigma^2}{n} X_{00}^{-1} \quad (4.2.3)$$

The variances of the components of  $F$  and  $E$  also depend on the state of deformation. However, this state is unknown in advance and will not be taken into account in the following. Besides, as motivated in appendix H, this simplification has no far-reaching consequences on the results obtained.

Let us examine the variance  $\sigma^2$ , defined by (3.3.17), in (4.2.3). As can be seen from (3.3.14) there are two sources for this error. These are the model errors  $\delta \vec{v}_i$ ; and the measurement errors  $\vec{w}_i$ . With regard to the model errors  $\delta \vec{v}_i$  it is observed that they depend on the unknown state of deformation so it is not possible to make clear statements about them. However, it may be expected that these errors increase, when the area occupied by a strain group is increased. This certainly is true when the state of deformation is inhomogeneous. From this point of view it is advisable to keep the area occupied by a strain group as small as possible. The size of this area is characterized by expression (3.3.27). The measurement errors are assumed to be dominated by the discretization of the pictures. In appendix I it is shown that the variance due to the discretization is given by (I.31):

$$\sigma^2 = \frac{1}{5.5 p^3 d} [\text{mm}^2] \quad (4.2.4)$$

Markers of a strain group are said to lie close together if the variance  $\hat{\sigma}^2$  estimated with the aid of (3.5.21) is of the same order as the theoretically determined  $\sigma^2$  by means of (4.2.4).

The importance of a high scan resolution  $p$  is obvious. It can be changed by choosing another magnification factor  $m$  (see (4.1.1)). Decreasing the variance  $\sigma^2$  by increasing the marker diameter seems also evident. However, before this is concluded the number of markers  $n$  belonging to a strain group has to be considered. It is reasonable to state that the number of markers within a given area is inversely proportional to the square of the marker diameter; thus:

$$n \triangleq d^{-2} \quad (4.2.5)$$

This is based on the assumption that the ratio between marker diameter and mutual marker distance is constant. From (4.2.4) and (4.2.5) it is seen that

$$\frac{\sigma^2}{n} \triangleq d \quad (4.2.6)$$

Thus, bearing in mind the assumption made, the accuracy is raised when the number of markers in a given area is increased. This, contradicts the suggestion with regard to increasing the marker diameters resulting from (4.2.4). It should be noted that  $X_{00}^{-1}$  does not change essentially when the number of markers in a given area is changed.

Further examination of  $X_{00}^{-1}$  is restricted to strain groups for which the markers are homogeneously distributed in a circular area. According to (3.3.28)  $X_{00}^{-1}$  then is written as:

$$X_{00}^{-1} = \frac{3}{\text{tr}(X_{00})} I \quad (4.2.7)$$

where  $\frac{1}{3} \text{tr}(X_{00})^{1/2}$  can be interpreted as the average distance between markers and the central marker. This is called the group radius. From (4.2.7) it is immediately clear that the accuracy is raised when the group radius is increased. However, this increases the area occupied by the markers so the model errors  $\delta \vec{v}_1$  may be increased too, as argued before. Thus, caution has to be taken by choosing the size of the strain group.

Finally, it is observed that for a strain group for which  $X_{00}$  is of the form given by (4.2.7) the covariances of F ((3.5.28) and 3.5.29)) and E (3.5.35) are minimized.

One possibility to increase the accuracy, scanning a picture more than once, is left out of consideration because this is taking up too much time with the processing of the data.

Summarizing, it can be stated that the accuracy of the strain distribution measurement can be influenced by the marker diameter  $d$ , the number of markers in a strain group, the distance of these markers to the central marker and their distribution. Some of these factors conflict, so a compromise has to be searched for which leads to an optimal performance for a given experiment.

#### Interpretation of the results

From (3.5.35) it is easily derived that the variances of the normal and shear components of the Green-Lagrange strain tensor F are given by:

$$\sigma_{E_{ii}}^2 = \frac{\sigma^2}{n} F_{pi} F_{pi} (X_{00}^{-1})_{ii} \quad (4.2.8)$$

and

$$\begin{aligned} \sigma_{E_{ij}}^2 = & \frac{\sigma^2}{4n} [F_{pi}F_{pi}(X_{00}^{-1})_{ii} + 2 F_{pi}F_{pj}(X_{00}^{-1})_{ij} + \\ & + F_{pj}F_{pj}(X_{00}^{-1})_{jj}] \end{aligned} \quad (4.2.9)$$

respectively. Again, restricting  $X_{00}$  to the form given by (4.2.7), noting that:

$$F_{pi} F_{pj} = 2 E_{ij} + \delta_{ij} \quad (4.2.10)$$

and assuming that  $E_{ij} \ll 1$ , (4.2.8) and (4.2.9) reduce to:

$$\sigma_{E_{ii}}^2 = \frac{\sigma^2}{n} 3 \operatorname{tr}^{-1}(X_{00}) \quad (4.2.11)$$

and

$$\sigma_{E_{ij}}^2 = \frac{\sigma^2}{n} \frac{3}{2} \operatorname{tr}^{-1}(X_{00}) \quad (4.2.12)$$

respectively. Because  $\sigma^2$  can be calculated with the aid of (I.31) the variances  $\sigma_{E_{ii}}$  and  $\sigma_{E_{ij}}$  can be determined for a given experiment.

From the results, in terms of computed strains, an estimate  $\hat{\sigma}^2$  can be obtained with the aid of (3.5.21). Using (4.2.8) and (4.2.9) leads to estimates  $\hat{\sigma}_{E_{ii}}$  and  $\hat{\sigma}_{E_{ij}}$ . By comparing the beforehand calculated and the afterwards estimated variances, statements can be made about the assumptions and simplifications which are included within the theory. This will be demonstrated in the next section.

While the calculated strains are presented in a vector plot, finally the accuracy of the direction of the principal strains is considered. Restricting ourselves to the 2-dimensional case it is well-known that the direction of the eigenvectors of the principal strains with respect to some local coordinate system is determined by an angle  $\phi$  which follows from:

$$\tan 2\phi = \frac{2E_{12}}{E_{11}-E_{22}} \quad (4.2.13)$$

For  $\phi \ll 1$  deviations  $\delta\phi$  are given by:

$$\delta\phi = \frac{1}{E_{11}-E_{22}} \delta E_{12} - \frac{E_{12}}{(E_{11}-E_{22})^2} (\delta E_{11} - \delta E_{22}) \quad (4.2.14)$$

Thus, the variance  $\sigma_{\phi}^2$  of  $\phi$  for  $\phi = 0$ , whereby  $E_{12} = 0$ , is given by:

$$\sigma_{\phi}^2 = \frac{1}{(E_{11}-E_{22})^2} \sigma_{E_{ij}}^2 \quad (4.2.15)$$

It is immediately seen from (4.2.15) that for  $E_{11} \approx E_{22}$ ,  $\sigma_{\phi} \rightarrow \infty$ , which is obvious as  $\phi$  is not defined in that case.

### 4.3 TEST MEASUREMENTS

With the results of the measurements described in this section, the actual performance of the measuring system is compared with the predicted performance. These are tests for the theoretical models described in chapter 3. First, discretization errors are dealt with, and next, on the basis of a uniaxial tensile test on a synthetic strip (Medical Sheeting), different aspects of accuracy are discussed.

#### Discretization errors

One of the major assumptions within the theory concerning the errors is that the random errors caused by discretization of the pictures are the only important ones (Appendix I). Other kinds of random errors and systematic errors for which no correction is carried out are assumed to be much smaller and can be neglected. To verify this the spatial coordinates of 48 markers on a flat rigid plate, distributed in such a manner that they captured a maximum of the measuring volume, were reconstructed from five different scans. The theoretical and measured results, as well as the important

Table 4.3.1.

Measured and theoretically determined deviation  $\sigma_x$  (I.19).

Standard deviation	:	$\sigma_x$ [mm]
measured	:	0.0073
predicted	:	0.0071
Scan resolution	:	$p = 13$ [pix/mm]
Marker diameter	:	$d = 0.5$ [mm]
Number of degrees of freedom	:	$n = 576$

parameters involved are given in table 4.3.1. The agreement is quite good. This indicates that the assumptions with regard to the random errors are legitimate and (4.2.4) is an appropriate formula for determination of the accuracy of a particular measurement.

#### Testing of the accuracy by means of a tensile test

On a specimen (Medical Sheeting; 42 x 14 x 0.15 [mm]) 88 markers (indian ink,  $d = 0.75$  mm) were placed in a way as shown in fig. 4.3.1. The mean distance between the markers was 2 [mm], the scan resolution  $p = 13$  [pix/mm]. The specimen was subjected to a tensile test whereby the clamp displacement  $u_{c1}$  was prescribed as given in table 4.3.2. In this table, also the Green-Lagrange strains calculated from the clamp displacements is given. After data

Table 4.3.2

The clamp displacement ( $u_{c1}$ ) and the Green-Lagrange strain ( $E_{c1}$ ) based on the clamp displacement.

	$u_{c1}$ [mm]	$E_{c1}$	$\lambda = \frac{L}{L_0}; L = L_0 + U_{c1}$ $E_{c1} = \frac{1}{2} (\lambda^2 - 1)$
1	0.00	0.0000	
2	0.05	0.0012	
3	0.10	0.0024	
4	0.20	0.0048	
5	0.50	0.0120	
6	1.00	0.0241	
7	2.00	0.0488	
8	5.00	0.1261	
9	5.00	0.1261	

processing it appeared that only 6 markers were not suited for further use due to artifacts in some of the pictures. They are omitted in fig. 4.3.1.

The difference between state 8 and 9 in table 4.3.2 is that for state 9 the optical system (fig. 4.2.1) was moved with respect to the

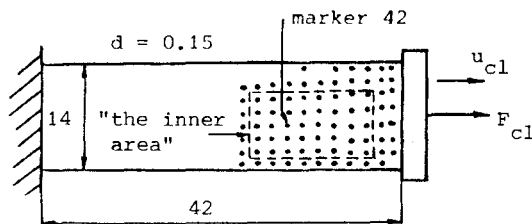


Fig. 4.3.1 A specimen with Indian ink markers subjected to a tensile test.

specimen. First, the influence of the marker distance with respect to the central marker is examined. Strain groups are defined with 3 different sizes ( $\text{tr}(X_{00}) = 6, 22, 49$ ). This is done with strain groups of 4 markers as well as groups of 7 markers. For each of the size/number combination 8 different groups are defined by choosing markers randomly from a given set of markers which are regularly distributed around the central marker. This central marker (no. 42 see fig. 4.3.1) is chosen in the middle of the specimen and far from the clamps so the influence of an inhomogeneous strain field may be considered to be minimal; at least for a strain group with a relatively small dimension  $R$  (chapter 3 (3.3.27)) compared to the width of the specimen. The theoretically determined deviation  $\sigma$  (4.2.4) as well as the estimated deviations  $\hat{\sigma}$  (3.5.21) from the measured results are given in table 4.3.3. These results refer to the situation of maximum clamp displacement. ( $E_{c1} = 0.1261$ ).

Table 4.3.3

Measured (3.5.21) and theoretically determined (4.2.4) deviation  $\sigma$  as a function of the marker distance. The number of markers in a strain group is given by  $n$ ,  $\text{tr}(X_{00})$  is the trace of the marker distribution tensor  $X_{00}$ .

				$\sigma$ [mm]
Theory	:	$n \text{ tr}(X_{00})$		0.011
Measured	:	4	6	0.013
			22	0.013
			49	0.022
		7	6	0.010
			22	0.014
			49	0.021

From table 4.3.3 it is seen that for a strain group with a large dimension, theoretical and experimental results deviate considerably. This is caused by the model error  $\delta \vec{v}_i$  (3.3.13). From now on this model error is taken into account by assuming a linear relationship between  $\sigma_v$  and  $\text{tr}(X_{00})$  given by:

$$\sigma_v = 3.7 \cdot 10^{-4} \text{tr}(X_{00})[\text{mm}] \quad (4.3.1)$$

The theoretical and measured results for the deviation  $\sigma_{E_{ii}}$  ((4.2.11) and (4.2.8) respectively) are given in table 4.3.4.

Table 4.3.4

Measured (4.2.8) and estimated (4.2.11) deviations  $\sigma_{E_{ii}}$ . The number of markers in a strain group is given by  $n$ ,  $\text{tr}(X_{00})$  is the trace of the marker distribution tensor  $X_{00}$ .

		$\sigma_{E_{ii}}$	
$n$	$\text{tr}(X_{00})$	Theory	Measured
4	6	0.0032	0.0035
	22	0.0021	0.0019
	49	0.0021	0.0026
7	6	0.0024	0.0019
	22	0.0016	0.0016
	49	0.0016	0.0017

Taking into account the simple model for  $\sigma_v$  (4.3.1) the agreement is very good.

Next, the influence of the number of markers in a strain group is examined while the distribution tensor  $X_{00}$  (3.3.23) is,

approximately, kept constant. This is done by choosing markers randomly from a given set of 48 markers which are regularly

Table 4.3.5

Measured (3.5.21) and theoretically determined (4.2.4) deviation  $\sigma$  as function of the number of markers ( $n$ ) in a strain group;  $\text{tr}(X_{00})$  is the trace of the marker distribution tensor  $X_{00}$ .

	$n$	$\sigma$	
Theory	:	0.016	$\text{tr}(X_{00}) = 33$
measured	4	0.019	
	8	0.016	
	16	0.016	

distributed around the central marker (no 42). In this way, 15 different strain groups are defined for three different sizes of strain groups ( $N = 4, 8, 16$ ). Results for the deviation  $\sigma$  are given in table 4.3.5. (for the theoretically determined deviation  $\sigma$  the contribution of  $\delta \vec{v}_1$  is here taken into account according to (4.3.1)).

Table 4.3.6

Measured (4.2.8) and estimated (4.2.11) deviations  $\sigma_{E_{ii}}$  as function of the number of markers ( $n$ ) in a strain group;  $\text{tr}(X_{00})$  is the trace of the marker distribution tensor  $X_{00}$ .

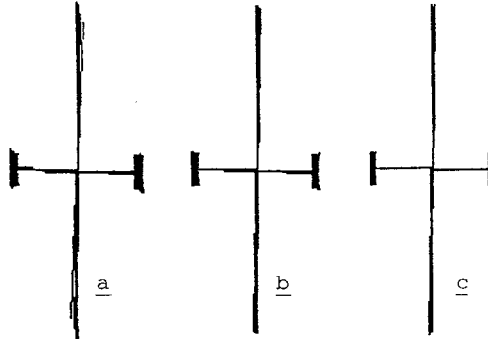
	$n$	Theory	Measured	$\text{tr}(X_{00}) = 33$
	4	0.0020	0.0028	
	8	0.0014	0.0016	
	16	0.0010	0.0012	

Again, these results refer to  $E_{c1} = 0.1261$ . In table 4.3.6 measured and theoretical results for the deviation  $\sigma_{E_{ii}}$  are given.

As an illustration vector plots of the principal strains are given for the different group sizes in fig. 4.3.2 as well as the deviations  $\sigma_\phi$  (see 4.2.15) and the values of the principal strains.

Finally, the results from a large number of strain groups are presented. For each marker three groups of 8 markers were defined by choosing randomly from the set of the 20 adjacent markers. The results presented in table 4.3.7 concern the inner-area (the two rows near the clamp and the markers on the edge are excluded), those in table 4.3.8 concern all markers. As the differences between the results of the three randomly chosen strain groups per marker were negligible ( $\pm 0.0001$  for the strain deviations), the values given in both tables are averages of these results. The difference between the

two sets of strain groups shows the influence of the inhomogeneous strain field near the clamp and, possibly, at the edges.



Mean principal strains		Deviation $\sigma_\phi$ [rad]	
$E_{11}$	$E_{22}$	$\sigma_\phi$	
a: 0.1131	- 0.0490	a: 0.009	
b: 0.1129	- 0.0468	b: 0.006	
c: 0.1133	- 0.0463	c: 0.004	

Fig. 4.3.2 Vector plots of the principal strains for fifteen randomly chosen strain groups with different size ( $n = 4, 8, 16$ ).

The theoretically determined  $\sigma_{E_{ii}}$ , with  $\text{tr}(X_{00}) = 13.6$ , equals  $14.10^{-4}$  and, with taking into account (4.3.1) it follows  $\sigma = 120.10^{-4}$  and  $\sigma_{E_{ii}} = 16.10^{-4}$ . Determination of a strain measure from the clamp displacements ( $E_{C1}$ ) leads to an overestimation of the real strain (about 10% when "1-2" and "1-3" are excluded).

The following observations are made from table 4.3.7 and 4.3.8:

- the agreement between the results obtained from the measurements and the theoretically determined values is, on the whole, good.
- the difference between the results for which the unloaded state is taken as the reference state and those for which the preceding state is taken as the reference state is remarkable, (except for the large step 7-8 ( $u_{C1} = 3$  [mm])). This indicates that the unloaded state is poorly defined.
- the results for "8 - 9", the situation for which the specimen was undisturbed but the optical system was moved, are correct. They coincide with the theoretical results without taking into account (4.3.1).
- the influence of inhomogeneous strain fields near the clamp is clearly visible but not startling as can be seen by comparing table 4.3.7 and 4.3.8.



Table 4.3.7

The unexplained variation  $V_u$  and the deviations  $\hat{\sigma}$  (3.5.21),  $\hat{\sigma}_{E_{ii}}$  (4.2.8) and  $\hat{\sigma}_\phi$  (4.2.15) for the inner area

	$V_u^*$	$\hat{\sigma}^*$	$\hat{\sigma}_{E_{ii}}^*$	$\hat{\sigma}_\phi$
1-2 <sup>+</sup>	21	145	21	0.99
1-3	17	130	19	1.04
1-4	18	134	19	0.45
1-5	22	148	21	0.13
1-6	20	142	21	0.05
1-7	21	146	22	0.02
1-8	25	159	24	0.01
1-9	26	161	24	0.01
2-3	14	116	17	0.74
3-4	12	111	16	0.42
4-5	16	126	18	0.38
5-6	14	119	17	0.07
6-7	14	117	17	0.03
7-8	25	158	23	0.02
8-9	9	95	13	1.08

Table 4.3.8

The unexplained variation  $V_u$  and the deviations  $\hat{\sigma}$  (3.5.21),  $\hat{\sigma}_{E_{ii}}$  (4.2.8) and  $\hat{\sigma}_\phi$  (4.2.15) for all markers

	$V_u^*$	$\hat{\sigma}^*$	$\hat{\sigma}_{E_{ii}}^*$	$\hat{\sigma}_\phi$
1-2 <sup>+</sup>	22	148	23	0.98
1-3	17	131	20	0.89
1-4	22	147	22	0.54
1-5	22	149	22	0.15
1-6	22	149	23	0.06
1-7	24	156	24	0.03
1-8	31	175	27	0.01
1-9	32	179	28	0.01
2-3	14	117	17	0.70
3-4	12	118	16	0.33
4-5	18	135	21	0.51
5-6	15	123	19	0.09
6-7	15	122	19	0.04
7-8	26	162	25	0.02
8-9	9	92	14	0.83

\* multiply with  $10^{-4}$

+ the two numbers i-j refer to the reference and actual state

It is concluded that the strain measuring system fulfils the expectations that result from theoretical considerations and that theoretical models are useful tools for design of the set-up and interpretation of measured data. It is seen that, after correction for systematic errors, the random errors resulting from the discretization of an image are dominating, at least for a strain field which does not vary strongly within an area occupied by a strain group. When large strain gradients occur the random part  $\delta \vec{v}_i$  (3.3.14) of the model error  $\vec{v}_i$  will obscure the results. However, this is not necessarily a negative result. By comparing the estimated deviations  $\hat{\sigma}_{E_{ii}}$  of the strain groups, strong local changes in the strain field can be detected. Strong local changes in the strain field may not always be recognizable from the determined strain field. As the strain field is estimated by using finite vectors  $\Delta \vec{x}_{ij}$  (3.3.20) such effects may be obscured.

---

## 5. LOAD TRANSMISSION BY COLLAGENOUS CONNECTIVE TISSUES.

---

### 5.1 INTRODUCTION

In this chapter a description is given of experiments, in which the previously described tools are used to study the load transmission through collagenous connective tissue. For this study, collagenous connective tissue from the cubital regio was used. The primary objective of the experiments was to gain insight into the mechanical behaviour of the structure. A secondary goal was to demonstrate the abilities of the developed tools when used on soft tissues.

The experiments were focused on four factors which are believed to be of major importance with regard to the mechanical behaviour of the tissues under investigation:

- the proportion of collagenous fibres
- the texture of the collagenous fibres
- the amorphous matrix
- the boundary conditions.

Collagenous fibres are considered to be the most important load-bearing components of the tissue. Their stiffness as well as their tensile strength are much larger than those of the other components (Gray, 1973, Ross and Clawson, 1980, Viidik and Vaust, 1980). For the structure under investigation, the majority of the collagenous fibres originates from the humeral lateral epicondyle and run from proximal to distal. Locally, the collagenous fibres are mainly oriented in parallel fashion. This causes the tissue to be highly anisotropic. The collagenous fibres determine the stiffness in one direction, whereas the stiffness transverse to that direction is mainly determined by the few diverging collagenous fibres and the amorphous matrix. This matrix is important for the load transfer between collagenous fibres when the tissue is sheared.

The high anisotropy together with the boundary conditions are of major importance with respect to the force transmission through a structure consisting of this type of material. For example, when inhomogeneous boundary conditions are applied to the tissue some "believes" used in engineering practice lose their value. Boundary conditions are said to be inhomogeneous when they produce an inhomogeneous stress and strain field in a homogeneous body. For most engineering materials the following holds:

- If the distribution of a load on a small part of body's surface is changed without changing its resultant, the stress and strain fields alter only significantly near the part of the surface where the load is applied.

This is known as the principle of Saint-Venant. It is often used for the mathematical solution of mechanical problems with inhomogeneous boundary conditions. The principle states that the solution may be in

error in the vicinity of a limited area, elsewhere the solution is satisfactory (Hunter, 1983). As will be demonstrated, for the type of tissue considered, Saint-Venant's principle is not valid due to the high anisotropy.

It was felt that experiments with inhomogeneous boundary conditions are of great importance to gain more insight in the mechanical behaviour. For instance, loading a small part of an edge of a specimen is instructive, because in this case shear is forced to a high level. The invalidity of St. Venant's principle is then demonstrated in a most distinct way. The first experiment described in section 5.3 is an example of this. Next, comparison of the effect of different non-homogeneous loads yields indications on the homogeneity of the specimen. Further, measuring the way stress and strain fields are affected by known inhomogeneous boundary conditions, supports the interpretation of measured stress and strain fields in case boundary conditions are not or badly known. The last experiment described in this chapter is an example thereof.

The types of boundary conditions which have been applied to the edge of samples during testing are:

- prescription of the displacement of an edge as a whole (tensile test conditions).
- loading of an edge with, approximately, a constant distributed force.
- loading of a small part of one edge to create an inhomogeneous boundary condition.

How these boundary conditions are realized in practice is subject of the next section which also deals with more general aspects of the experiments. These experiments are described in the remainder of this chapter. Although different parts of the structure from the cubital regio are used in different experiments, the results are not presented as specific for these parts. On the contrary, one important mechanical phenomenon of this type of tissue is highlighted with each experiment described. The experiments concern anisotropy (section 5.3.1), inhomogeneity (section 5.3.2), biaxial loading (section 5.3.3) and in situ measurements (section 5.3.4).

## 5.2 GENERAL ASPECTS CONCERNING THE EXPERIMENTAL PROCEDURES

Storage, preparation and testing environment

Tissue samples were obtained from freshly frozen cadavers (- 25 [°C]). After preparation or use in an experiment, samples were frozen again. Storage was repeated no more than two times. During preparation or during an experiment the tissue was abundantly suffused with saline at room temperature. Effect of freezing, restoring and experimental environment as well as donor age are not taken into account as experimental variables (Woo et. al, 1986).

The experiments described in this chapter, except for the last one, are done on samples of the collagenous connective tissue structure from the lateral side of the elbow regio. The structure can be isolated as a whole from its surroundings (subcutaneous tissue, muscle fibres, etc.) without disturbing its coherence. It is cut, as close as possible to the humeral lateral epicondyle. As the complex geometry of the structure is normally maintained by the supporting surroundings, this geometry is lost after isolation of the structure. Next the intermuscular septa are separated from the epimysial connective tissue. Fig. 5.2.1 gives an example of such a fragment. The characteristic fibrous texture is accentuated by means of trans-illumination. In this way, pictures of all specimens were made to obtain a (at least) gross impression of the fibre texture.

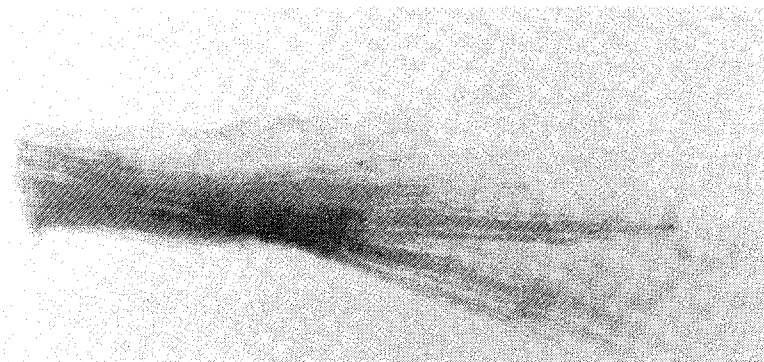


Fig. 5.2.1 The isolated intermuscular septum situated at the interface of the extensor carpi radialis brevis muscle on one hand and the extensor digitorum and supinator muscles on the other. Both, muscular fibres from the extensor carpi radialis brevis and the extensor digitorum muscles attached to this septum.

Specimens with a relatively simple shape are prepared from such fragments. During preparation care was taken to avoid the cutting of collagenous fibres as much as possible, maintaining a maximum of the integrity of the tissue.

#### Thickness measurement

A meaningful interpretation of the measured local stress and strain fields demands for a local measure of the thickness. As stated in chapter 3, tissue thickness is a vague and questionable conception. Thickness measurement for a rigid material does not cause problems, whereas for specimens of soft tissue this is certainly not trivial as the relation between the thickness and the squeezing measuring force is not very well understood (Vossoughi, 1984). For that reason cross-sectional area measuring techniques have been developed whereby the tissue is not touched (Ellis, 1969). However,

these techniques are still poor with respect to reproducibility. Moreover, most of them do not allow of local thickness measurement but rather give a measure for the cross-sectional area.

The thickness of a soft tissue specimen may vary due to local differences in the amount of non-fibrous substances (e.g. water, glycosaminoglycans, etc.). When investigating the mechanical behaviour of soft tissue, it seems obvious to choose for an operational definition of the thickness, which possibly only relates to the load-bearing substances (eg. collagenous fibres, Riemersma, 1986). It was beyond the scope of the present work to develop an elaborated thickness measuring method that meets such an operational definition and offers the possibility to measure local thickness.

From literature no such thickness measuring method is known. A more intuitively based method is chosen. This method is based on the idea that when the tissue is loaded with an indenter, with a relatively small diameter, the fluid-like substances are pressed away from the volume beneath the indenter within a short time (Oomens, 1985). This idea is outlined in fig. 5.2.2.

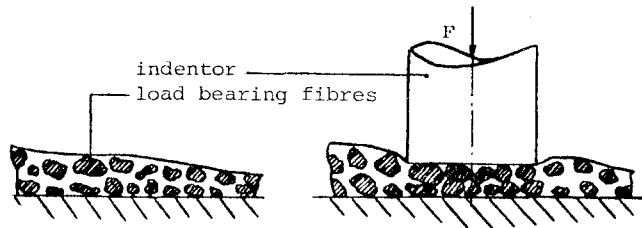


Fig. 5.2.2 A simplified representation of the applied thickness measuring method.

A dial gage is used for this purpose; the plunger functions as the indenter ( $D=4.7$ [mm], measuring force  $F=0.65$ [N]). The tissue specimen is spread on a rigid, flat foundation. The thickness is measured when the pointer does not change its position more than  $0.01$  [mm] within  $10$  [s]. This moment is usually reached within one minute. Reproducibility was better than  $\pm 0.03$  [mm]. No permanent plunger indentations were observed in the specimens, they disappear within a few minutes. It was concluded that tissue is not damaged by measuring its thickness in this way. As it is proposed that thickness is a measure for the content of the load-bearing substances, no other method was applied to determine this content.

## Markers

Several types of markers were tested on the connective tissue. Convenience of mounting, a regular shape and sensitiveness for damage were the major criteria for selection. Indian ink and paper markers appeared to be most favourable. Indian ink markers can be placed easier and faster than paper markers which have to be bonded (Histo Acryl) one by one. However, the shape of the ink markers is less regular; paper markers are circular disks (thickness: 0.05 [mm], diameter: 0.8 [mm]) stamped from dull black paper. A less regular shape leads to a reduced accuracy. Pilot studies showed that the standard deviation of measured marker coordinates obtained with ink markers was 1.5 times the standard deviation of coordinates obtained with paper markers. Moreover, ink markers are quickly damaged on which occasion ink particles are spread over the tissue and so a specimen becomes unfit for further use. For those reasons, all experiments concerning connective tissue are carried out using paper markers.

## Loading

The transfer of a loading force to a specimen is usually done with the aid of a clamp, with hooks or with staples and thread. Clamps are used when an entire edge of a specimen has to be gripped, hooks and thread for local loading of a specimen or for biaxial testing. A great variety of clamp designs has been published (Sauren, 1981, Butler, 1984, Riemersma, 1986). Clamps usually consists of two

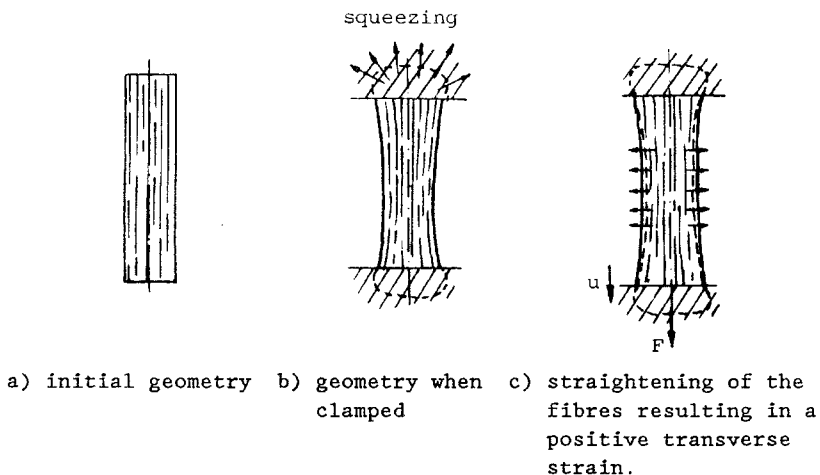


Fig. 5.2.3 The effect of squeezing of a specimen between the clamps

profiled plates between which the tissue is pressed. Besides slippage, the squeezing of the tissue between the plates may lead to surprising measuring results. This is demonstrated in fig. 5.2.3. Straightening of the collagenous fibres causes positive transverse strains. In pilot experiments positive transverse strains over 10% were measured. Therefore, a clamp was designed which does not cause widening of the tissue due to squeezing (see fig. 5.2.4).

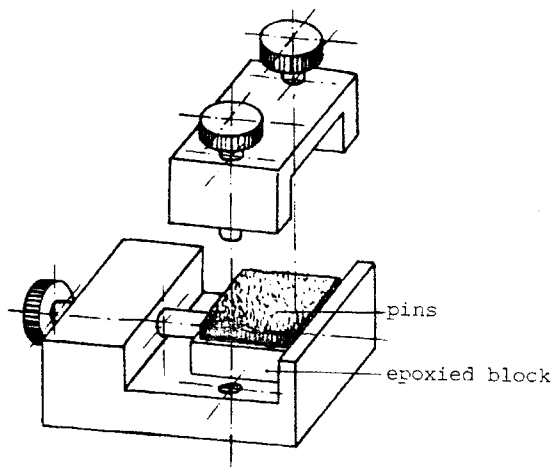


Fig. 5.2.4 A tissue clamp which avoids widening of a specimen due to clamping.

The most important part of the clamp is an epoxied block with a large number of small pins ( $d = 0.1$  [mm],  $L = 1.5$  [mm]) with a mutual distance of  $0.8$  [mm]. A specimen is put down on this block and softly tapped with a pair of tweezers so the pins penetrate the tissue. Next, the tissue is clamped causing the pins to penetrate the tissue further, meanwhile preventing it to widen. Some damage of the tissue will occur, but this is minimal and considered to be unimportant. The clamping effect can be further improved by treating the clamped part of the specimen with a bond.



Fig. 5.2.5 Mounting of a thread to a small strip of tissue.



For the transfer of local loads to a specimen the following procedure is used (see fig. 5.2.5). The part of the edge of the specimen to be loaded is isolated by making two small incisions ( $\pm 10$  [mm]). The width of such an isolated strip of tissue is usually about 2.5 - 3 [mm]. Next, the strip is hardened by greasing it with bond (Histo Acryl) and a thread is tied to this hardened part. Extra bond is spread over the knot to prevent slippage. The hardening prevents the untreated part of the strip to contract due to the knot. By means of the thread the strip can be loaded. In the following such a strip is called a load strip.

To create the possibility to prescribe equal displacements to a series of load strips (tensile test conditions) an equipment as shown in fig. 5.2.6 is used. The threads from the tissue strip can be fixed to a plate mounted on two long steelwires ( $L = 2000$  [mm]).

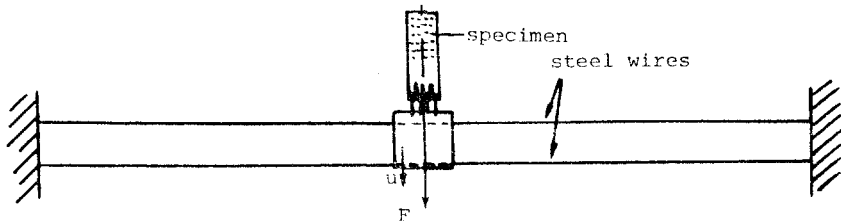


Fig. 5.2.6 Equipment for equal displacement prescription.

These steelwires prevent the plate to rotate, or translate in the direction perpendicular to the displacement prescribed. Within the range of prescribed displacements, the load required to move the plate is negligible (max 0.1 [N]) compared to the load transferred to the specimen (max. 20 [N]). The length of the threads between tissue strips and plates was chosen so that their extension was negligible compared to that of the specimen (ratio  $\approx 1:500$ ).

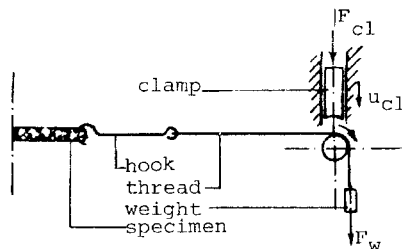


Fig. 5.2.7 Mounting of hooks and thread with the possibility to load the threads with a constant force by means of a weight or to prevent their displacement.

Finally, when a specimen is loaded biaxially, hooks and threads are used. These are only applied for loading a specimen perpendicular to the fibre direction. The mutual distance between the hooks ( $d = 0.05$  [mm]) is about 2 [mm]. All threads could be loaded with an equal force by weights or could be clamped such that the displacement of the edge to which they were attached was prescribed (fig. 5.2.7). The maximum tensile stress applied to the tissue was approximately  $10$  [ $\text{N}/\text{mm}^2$ ]. All experiments described are quasi-static, as time-dependent phenomena are beyond the scope of the present work.

### 5.3 RESULTS AND DISCUSSION

#### 5.3.1 Anisotropy

The impact of the anisotropy was demonstrated in an experiment performed on a specimen obtained from the fascia overlying the extensor carpi radialis brevis muscle. With this experiment the invalidity of Saint-Venant's principle is demonstrated. Collagenous fibres were oriented mainly in parallel fashion, diverging slightly in the distal direction. Therefore some fibres end on one of the long edges ("A", fig. 5.3.1) of the specimen. The proximal part was gripped, whereas on the distal part four threads were mounted

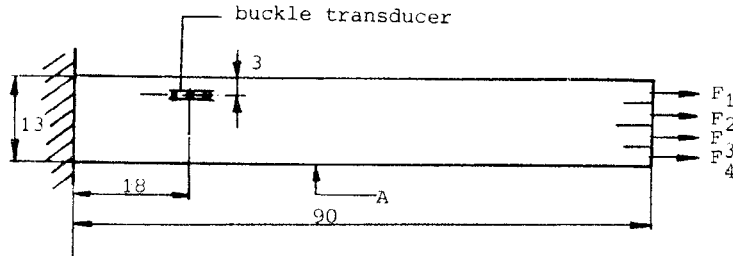


Fig. 5.3.1 Testing of the effect of anisotropy.

according to the procedure described in the previous section (fig. 5.3.1). A buckle transducer was installed near the clamp. In each experiment the four loading forces were varied on four levels (0, 1, 2, 3 [N]) and repeated 6 times. This cycle was repeated three times. The mean results of three repeated experiments are shown in fig. 5.3.2. For the forces  $F_3$  and  $F_4$  no curve is drawn in fig. 5.3.2 as the transducer did not give any significant signal for these loads.

The result is instructive. A portion of the fibres loaded by  $F_1$  pass the buckle transducer. The slope of the signal against force curve for  $F_1$  decreases. This shows that with an increasing force (increasing shear) more fibres of the tissue next to the loaded part are loaded. For the force  $F_2$  the transducer behaves in a reverse way.

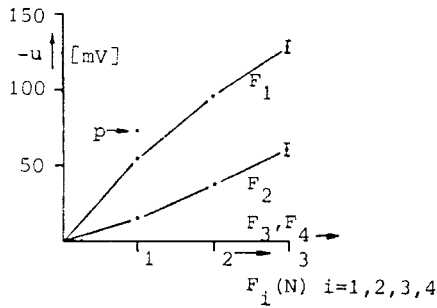


Fig.5.3.2 Measured response of a buckle transducer as a function of the magnitude and the location of a local load.

Because of the increasing shear the fibres which pass through the buckle transducer are loaded progressively. This phenomenon is restricted to a short distance, at least for this specimen, as demonstrated by the zero-response of the transducer on  $F_3$  and  $F_4$ . This phenomenon is confirmed by loading all threads with equal forces (1 N). In this case the effect of shear is eliminated mostly and thus the response of the transducer is higher (point P in fig. 5.3.2).

### 5.3.2 Inhomogeneity

Inhomogeneous properties were studied by means of successive strain and stress measurement on the same tissue sample. It will become clear that for the interpretation of the results it is necessary to account for the thickness of the tissue and the texture of the collagenous fibres.

A specimen was obtained from the fascia overlying the extensor digitorum muscle. Again, collagenous fibres were mainly oriented in a parallel fashion, diverging slightly in the distal direction. Therefore, some fibres end on a part of one of the long edges of the

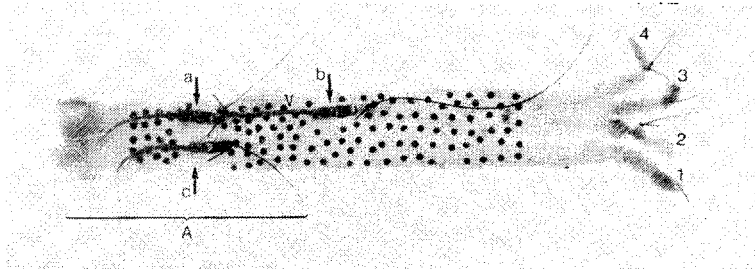


Fig. 5.3.3 A specimen obtained from the overlying fascia of the extensor digitorum muscle.

specimen (fig. 5.3.3., "A"). The picture of the specimen in fig. 5.3.3 also shows three installed buckle transducers and most of the markers. A thickness chart of the specimen is given in fig. 5.3.4. First the strain measurements were performed. Then the markers were removed from the places where the buckle transducers were installed. The results obtained for the stress measurements are presented first.

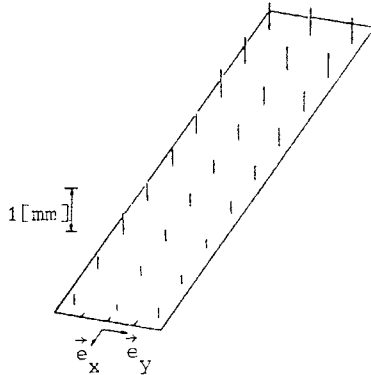


Fig. 5.3.4 Thickness chart of the specimen.

Two transducers (a, c) were mounted parallel close to the clamp and a third transducer (b) in series with (a) in the middle of the specimen (fig. 5.3.3). By comparing the response of the transducers (a) and (c) for similar loads on different load strips, the possible inhomogeneous properties can be demonstrated. These aspects were examined for local loading. For this purpose the "eccentricity"  $e$  of a local load is defined. A buckle transducer is said to belong to one of the isolated loading strips when the fibres passing through the buckle debouch on that strip. In that case the eccentricity is defined to be zero. Otherwise the eccentricity is defined as the number of strips shifted from the strip ascribed to the buckle transducer. The ascription of a buckle transducer to a loading strip is done by visual inspection of the fibre texture while the specimen is trans-illuminated. When this was infeasible, a buckle transducer was ascribed to the load strip which caused the maximum response for that transducer. By presenting the results in this way the influence of the fibre texture, important for this highly anisotropic material, is emphasized.

Transducer (c) is ascribed to load strip 1, transducers (a) and (b) to load strip 4. Results are shown in fig. 5.3.5. Measured local forces as well as stresses are given as function of the eccentricity  $e$ . The stress is determined by dividing the measured force by the width of the transducer and the local thickness measured in the unloaded state (first Piola-Kirchhoff stress). The results presented in fig. 5.3.5 refer only to the maximum loads (5[N]) because no extra information was obtained from the results for lower load levels.

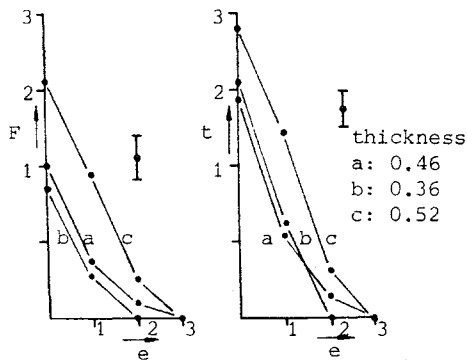


Fig. 5.3.5. Measured response of the transducers a, b, and c (see fig. 5.3.3) in terms of force  $F$  [N] (left panel) and stress component  $t$  [ $\text{N}/\text{mm}^2$ ] (right panel) as a function of the eccentricity  $e$  for  $F_1 = 5$  [N]. The thickness  $d$  [mm] of the tissue at the position of the transducers is given too.

Again, it is seen that the main part of the force transmission is restricted to a small part of the specimen. It can be expected that the maximum measured local force will be smaller than or equal to the applied load multiplied by the ratio between the width of the transducers (1.5 [mm]) and the width of the loading strips (3.25 [mm]). For the actual load case (5 [N]) the maximum measured load is expected to be 2.3 [N]. The results for transducers (a) and (b) meet these expectations. On the other hand those for transducer (c) do not due to fibres debouching transducer (c) end on a broader part of the specimen's edge.

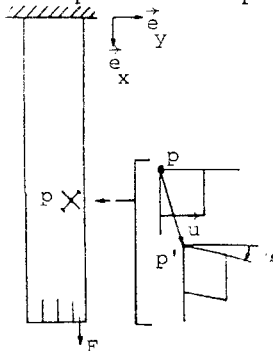


Fig. 5.3.6 Definition of an orthonormal vector base and the eigenvectors of the strain tensor  $E$  for a material point which is in pure shear.

Thus, a larger portion of fibres than suggested by the width-ratio is loaded. The response of transducer (a) is somewhat higher than of transducer (b), but this is not significant ( $p < 0.05$ ). The difference in the responses of transducers (a) and (c) already suggests

inhomogeneous effects. This will become more evident in the following discussion on the strain measurements.

Strain measurements have been performed for local loading, for the case of a distributed constant load as well as for tensile test conditions. For the presentation of the results an orthonormal vector base is introduced with respect to the specimen as shown in fig. 5.3.6. In the figures the principal strains are drawn as bars along the direction of the eigenvectors. The length of a bar corresponds with the magnitude of the principal strains. Negative

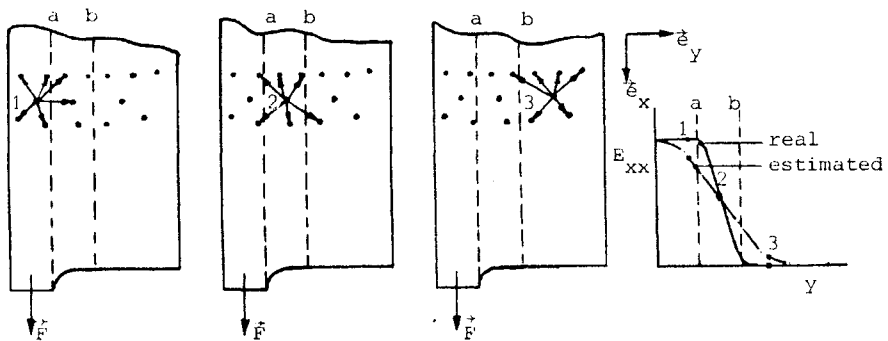


Fig. 5.3.7 Illustration of the effect of the finite length of the strain group vectors on the estimated strain components.

principal strains are discerned by cross lines at the ends of the bars. For a specimen under pure shear these bars are rotated over an angle of  $45^\circ$  with respect to the global vector base (fig. 5.3.6). In all figures concerning measured strains combinations of two numbers are given denoting the reference and the current state, respectively, for the results shown. Number 1 always indicates the unloaded state.

It should be noticed that due to the finite length of the vectors, used for the estimation of the strain tensor  $E$ , the influence of high gradients in the strain field is spread over a larger area than in reality. This is illustrated in fig. 5.3.7 where only the deformed state is drawn. By anticipating on the global strain field to be expected, this can be taken into account with the definition of the strain groups. In fig. 5.3.7, for the example, more markers have to be chosen in the  $x$ -direction than in the  $y$ -direction.

Fig 5.3.8 and 5.3.9 show the results of loading strip 1 (load case 1) and strip 4 (load case 4) with a load of 1, 3 and 5 [N].

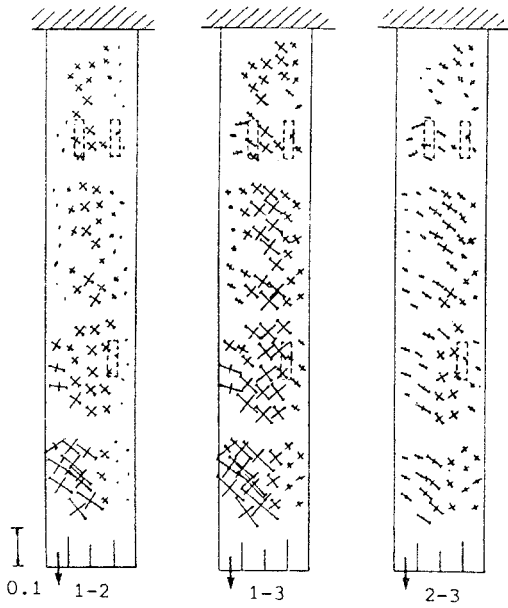


Fig. 5.3.8. Strain distribution for load case 1. The numbers indicate the reference and the deformed configurations (see text, page 5.12).

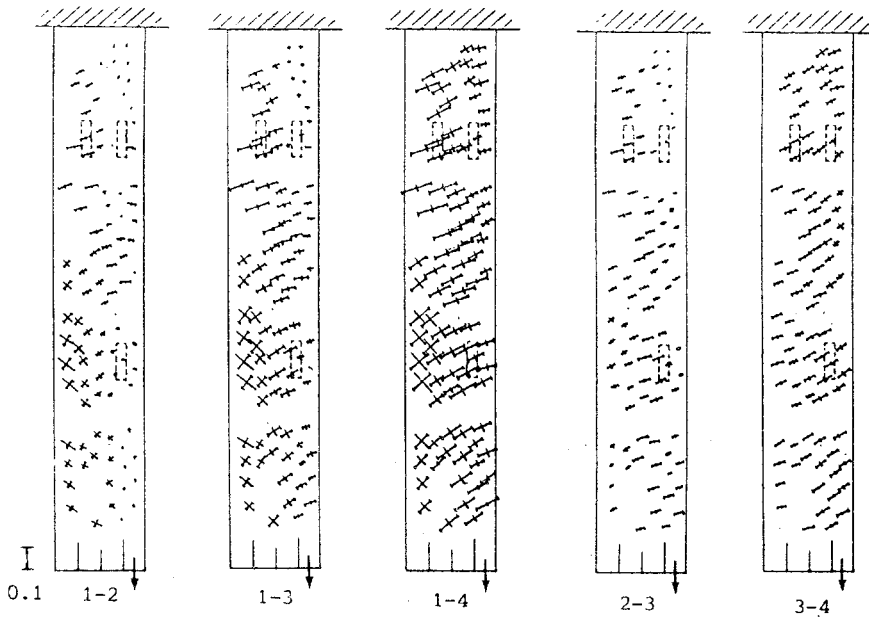


Fig. 5.3.9. Strain distribution for load case 4. The numbers indicate the reference and the deformed configurations (see text, page 5.12).

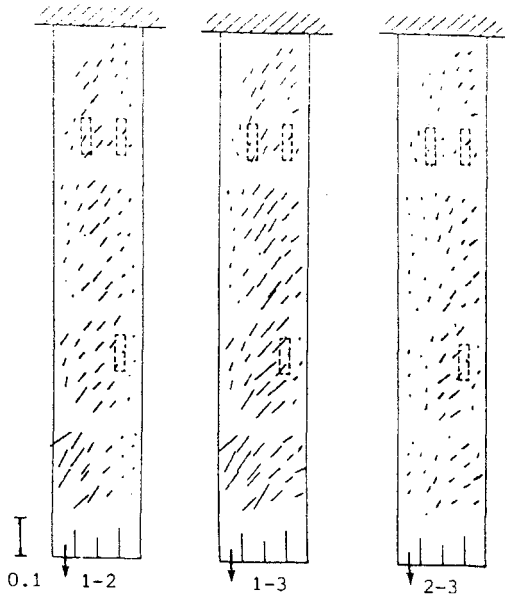


Fig. 5.3.10. Distribution of the positive principal strains for load case 1. The numbers indicate the reference and the deformed configurations (see text, page 5.12).

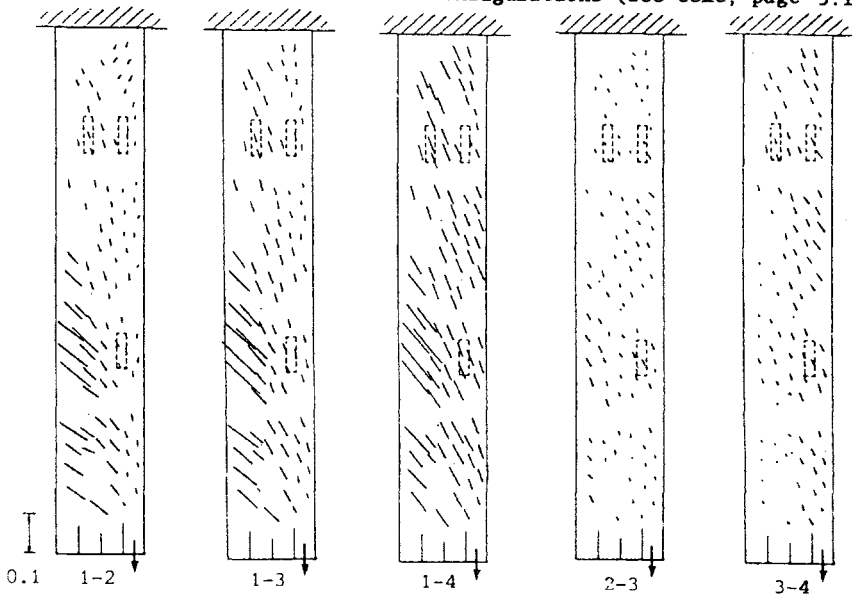


Fig. 5.3.11. Distribution of the positive principal strains for load case 4. The numbers indicate the reference and the deformed configurations (see text, page 5.12).



Strain distributions are given for both the unloaded as well as the foregoing loaded state as the reference configuration. The difference between the two loading cases is striking. Load case 1 shows a narrow band next to load strip 1 which is in pure shear ( $45^\circ$  angle !). This indicates that almost no load transfer takes place from the loaded part to the neighbouring tissue. For load case 4 the pure shear is restricted to a small area on the left lower part of the tissue. This area decreases near the upper clamp. This indicates an increasing load transfer to neighbouring tissue which is in agreement with the results obtained with the buckle transducers. The response of transducer (c) is larger for a larger eccentricity than for transducers (a) and (b) (see fig. 5.3.3). The large difference between maximal and minimal principal strains obscures the vector plots. In order to enhance the insight, also vector plots of only the positive principal strains are given (fig. 5.3.10 and fig. 5.3.11).

The difference between load cases 1 and 4 can be expressed in another way. When, as suggested, the load transfer in load case 1 is restricted to a narrow band on the left side of the specimen, the component  $E_{xx}$  (see fig. 5.3.7) of the strain tensor  $E$  must be positive for all strain groups within this small band and almost zero in the rest of the specimen. For load case 4 there must be a much broader band from the right to the left for which the strain component  $E_{xx}$  is non-zero. To check for this, the strain component  $E_{xx}$  is calculated for all strain groups and sorted by the y-coordinate (the strain group with the lowest y-coordinate is the first in the row, the one with the largest y-value the last). To exclude noise caused by measuring errors and the influence of the varying thickness in the x-direction (the sorted strain groups are randomly distributed with respect to the x-coordinate),

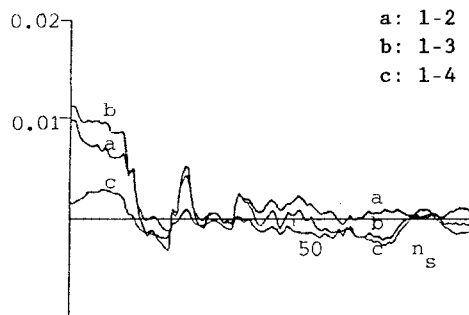


Fig. 5.3.12 The sample mean  $E_{xx}$  of a subset  $n_s$  ( $n=15$ ) of the total set of strain groups, moving along the y-coordinate (load case 1).

the mean  $\bar{E}_{xx}$  of moving subsets of the set of sorted strain components are taken, instead of the strain components themselves. The number of strain groups in one subset can be chosen arbitrarily (in this case 15). Fig. 5.3.12 and fig. 5.3.13 show the mean  $\bar{E}_{xx}$  of the moving subset for load case 1 and 4, respectively, for different load magnitudes. In fig. 5.3.12 also the result for which the first loaded state is chosen as the reference state is shown. For load case 1 the positive components  $E_{xx}$  are restricted to the narrow band on the left side of the specimen, as expected. In the remaining part of the specimen only random variations around zero are seen. For load case 4 a completely different result is obtained. The mean

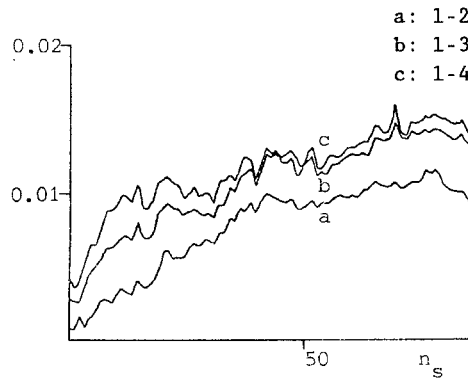


Fig. 5.3.13 The sample mean  $\bar{E}_{xx}$  of a subset  $n_s$  ( $n=15$ ) of the total set of strain groups, moving along the y-coordinate (load case 4).

component  $\bar{E}_{xx}$  is maximal at the loaded side and decreases gradually to the left, according to what is expected.

As strain groups may have markers in common, the estimated strain components can be partly dependent. However, because the strain groups within a subset are randomly distributed along the x-coordinate, the probability that they have markers in common is decreased. In this case the sample variance  $\hat{\sigma}^2(\bar{E}_{xx})$  of the subset is a good estimator for the variance  $\sigma^2(\bar{E}_{xx})$  of the real distribution of the strain components  $E_{xx}$ . This variance is constituted by four partial variances:

- measuring errors ( $\sigma_{E_{ii}}^2$  (4.2.11))
- model errors ( $\sigma_v^2$ )
- a variance caused by variations in thickness ( $\sigma_d^2$ )
- a variance caused by variations in fibre texture ( $\sigma_f^2$ )

For those areas of the specimen where no large gradients in the strain field occur, the conditions are similar as for the measurements described in the section 4.3. Hence the model error  $\sigma_v$  can be taken into account by using equation (4.3.1). From the other two partial variances, only the sample variance  $\sigma_d$  of the thickness

can be taken into account; the influence of fibre texture variations ( $\sigma_F$ ) is not understood at this juncture. Consequently a prediction of the variance  $\sigma^2(\underline{E})$  can be given to judge the value of the estimator  $\hat{\sigma}^2(\underline{E}_{xx})$ .

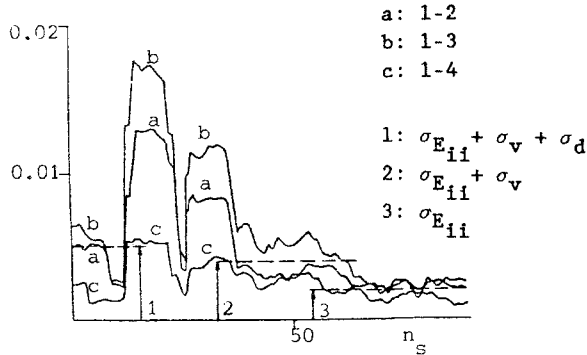


Fig. 5.3.14 The sample deviations corresponding to the sample means given in fig. 5.3.12 (load case 1). Predicted deviations are given by dash lines.

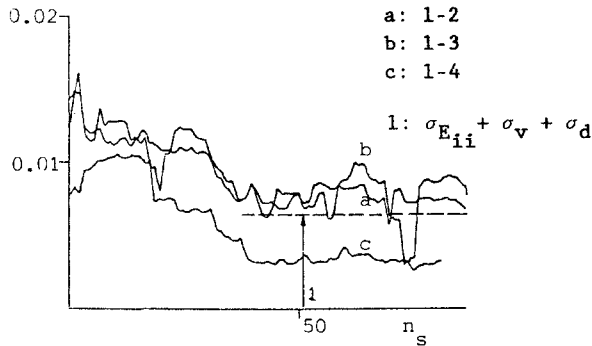


Fig. 5.3.15 The sample deviations corresponding to the sample means given in fig. 5.3.13 (load case 4). Predicted deviations are given by dash lines.

Fig 5.3.14 and 5.3.15 show the corresponding deviations  $\hat{\sigma}^2(\underline{E}_{xx})$  as well as the predicted deviations for load case 1 and 4, respectively, for different load magnitudes. The deviations for different parts of the specimen agree with the expectations. For load case 1 the band of points which are in pure shear, being an indication for a strong change in the strain field, show a maximum in the deviation. In the loaded part estimated and predicted deviations are almost equal. In the unloaded part the estimated deviation approaches the measuring

error. The nearly undeformed state at this part excludes the model errors and, of course, the influence of thickness variations.

Besides the loading cases treated above, strain field measurements were performed with the following boundary conditions:

- a distributed force, by loading the four load strips with equal forces (load case 5),
- simulation of a uniaxial tensile test by loading the four load strips in such way that the displacements of the strips are equal (load case 6).

The total loading force was applied at four levels (0,4,12,20 [N]). In fig. 5.3.16 (a and b) vector plots are given for load cases 5 and 6 for a load of 20 [N]. Plots are given for positive and negative principal strains as well as for positive principal strains only.

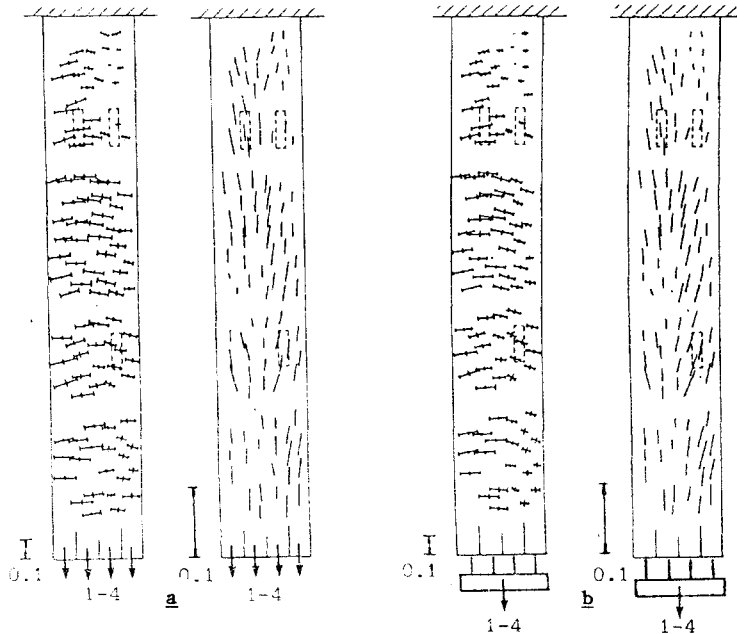


Fig. 5.3.16 The strain distribution for load case 5 (a) and load case 6 (b).

The pattern of the negative transverse strains is very regular in longitudinal direction, except in the vicinity of the clamp where the strains tend to zero. The difference of these strains in transverse direction indicates a larger transversal compliance for the left side (the thicker part ! see fig. 5.3.4) of the specimen. This agrees with the previously observed differences in load transfer in the specimen, when locally loaded.

The vector plots, which show the strain field to be inhomogeneous for both load cases, do not give a clear view on differences between the

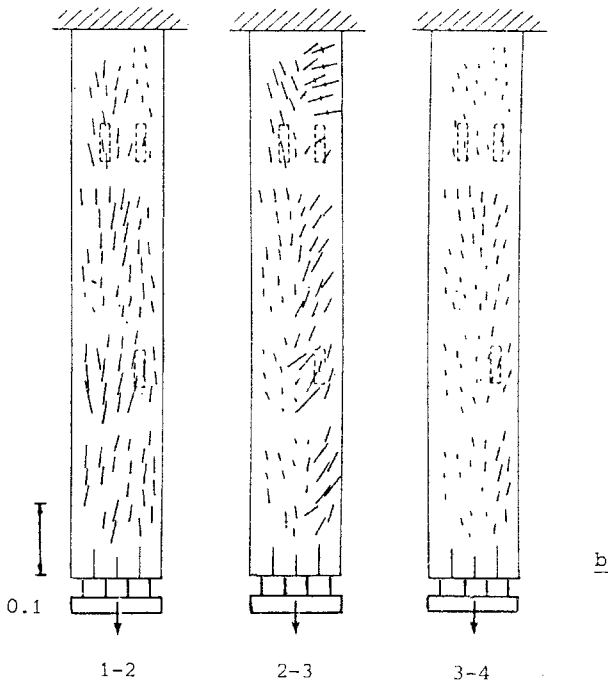
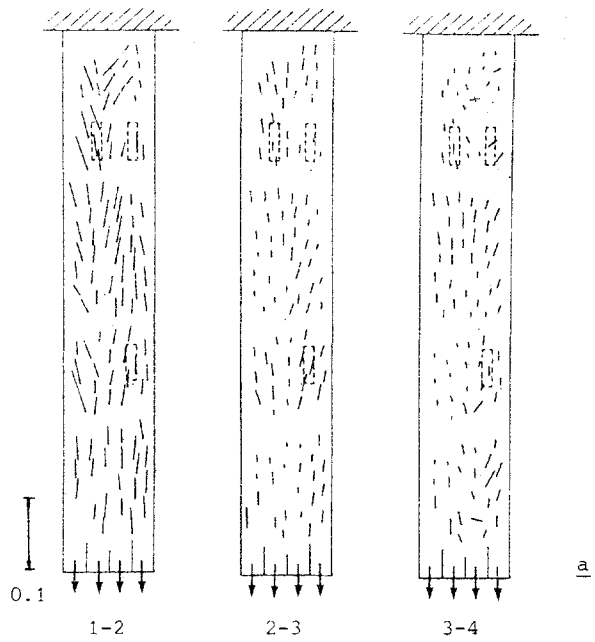


Fig. 5.3.17 The distribution of the positive principal strains for load cases 5 (a) and 6 (b) for the successive load steps.

two load cases. Differences are seen more pronounced when looking at the strain distributions (positive principal strains) for the successive load steps (thus taking the previous loaded state as the reference state). It is seen that the strain history certainly is different for both load cases (fig. 5.3.17).

Fig. 5.3.18 gives the vector plots for both load cases of the  $E_{xx}$  component of the strain tensor  $E$ . The distributions are, again, similar and inhomogeneous.

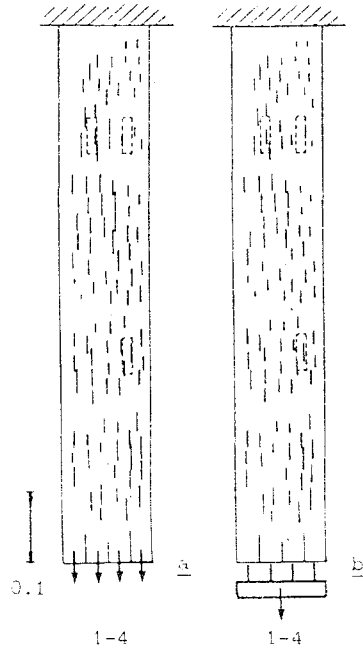


Fig. 5.3.18 The distribution of the strain component  $E_{xx}$  for load cases 5 (a) and 6 (b).

Again sample means of moving subsets of the complete set of strain components  $E_{xx}$  are calculated, at the cost of losing information on strain variations in a direction transverse to the moving direction of the subset. However, in this way trends in the set can be traced easily. First, the set of strain components is sorted by the  $y$ -coordinate (see fig. 5.3.6). Results for both loading cases are given in fig. 5.3.19. and 5.3.20.

The following is observed :

- For all load levels and for all sample means the results of load case 5 are larger than those for load case 6. This difference is rather uniform (0,0021 (0,0003)).
- The strain level is always higher at the left side of the specimen. The differences are significant ( $p < 0,05$ ) for both loading cases. Regarding the thickness of the specimen at this place, this is a

remarkable result (one may expect that for the thicker part (see fig. 5.3.4) the averaged strain components  $E_{xx}$  would be less than for the thinner part of the specimen). This trend is assigned to fibre texture. As mentioned before, due to the slight divergence few fibres end on the left side of the specimen. The maximum difference is more pronounced for load case 6 (0.0034) than for load case 5 (0.0021). This can be expected, as for a tensile test thicker parts of the specimen will carry a larger portion of the load, compared to the case with a distributed force.

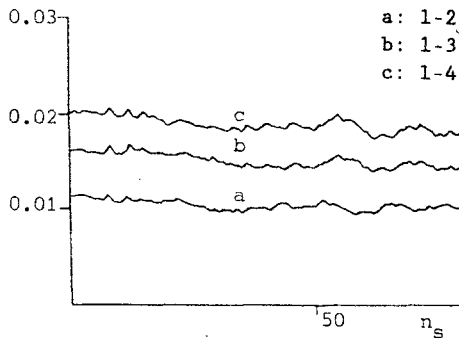


Fig. 5.3.19 The sample mean  $E_{xx}$  of a subset  $n_s$  ( $n=15$ ) of the total set of strain groups, moving along the y-coordinate (load case 5).

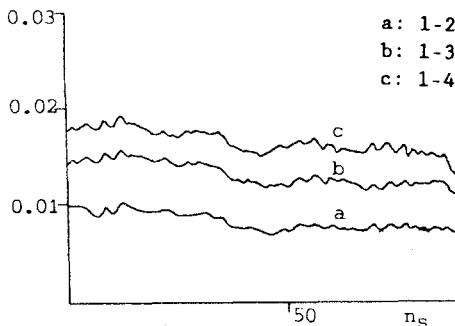


Fig. 5.3.20 The sample mean  $E_{xx}$  of a subset  $n_s$  ( $n=15$ ) of the total set of strain groups, moving along the y-coordinate (load case 6).

Next, the set of strain components was sorted by the x-coordinate (fig. 5.3.6) starting at the clamped side. Results for both load

cases are given in fig. 5.3.21 and 5.3.22. These results are very

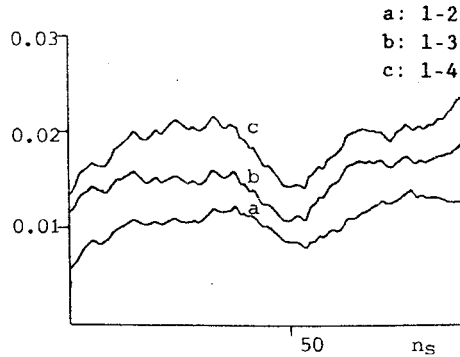


Fig. 5.3.21 The sample mean  $\bar{E}_{xx}$  of a subset  $n_s$  ( $n=15$ ) of the total set of strain groups, moving along the  $x$ -coordinate (load case 5).

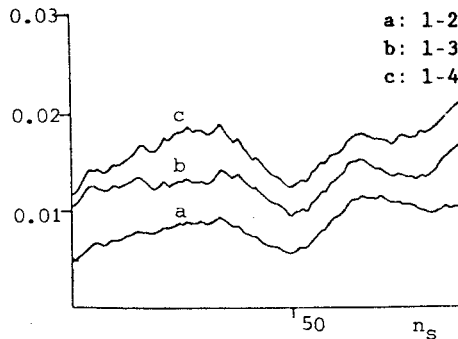


Fig. 5.3.22 The sample mean  $\bar{E}_{xx}$  of a subset  $n_s$  ( $n=15$ ) of the total set of strain groups, moving along the  $x$ -coordinate (load case 6).

remarkable. Considering the fact that these are sample means ( $n=15$ ), such a pronounced pattern was not expected. Global maxima and minima of the curves lie on the same place of the specimen, for both loading cases. Notice that the two load cases represent independent measurements, and in one load case the picture of the reference state is the only common factor for the three curves.

The strain groups, corresponding to the components  $E_{xx}$ , belonging to a subset are certainly not statistically independent as they lie close together, in contrast to the groups of subsets sorted by  $y$ -direction. Therefore, it was felt that a check on this result was necessary. For this purpose each set of markers was randomly divided in two equally sized new sets. This partition was different for both



loading cases. Within the newly created sets of markers new strain groups were defined and the procedure for the strain components  $E_{xx}$  was repeated for each of the four new sets. Results are given fig. 5.3.23 and 5.3.24. As the number of markers in one set is half the number of markers in the original set, the markers in the newly defined sets are more sparsely and irregularly distributed over the specimen. As a consequence the results will be less smooth and, moreover, the influence of the model errors will increase. The number of strain groups in a moving subset was adjusted to the larger mutual distance of the markers in the new sets. It is seen from fig. 5.3.23

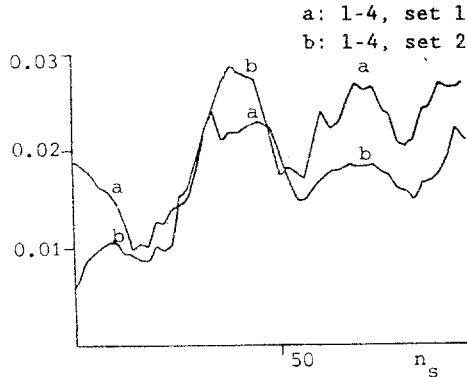


Fig. 5.3.23 The sample mean  $E_{xx}$  of a subset  $n_s$  ( $n=10$ ) moving along the  $x$ -coordinate. The set of markers is randomly divided into two new sets (a) and (b) (load case 5).

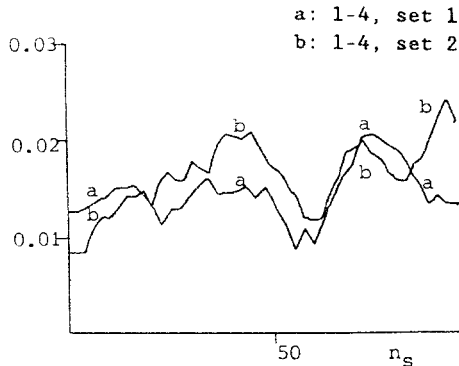


Fig. 5.3.24 The sample mean  $E_{xx}$  of a subset  $n_s$  ( $n=10$ ) moving along the  $x$ -coordinate. The set of markers is randomly divided into two new sets (a) and (b) (load case 6).

and 5.3.24 that, for both loading cases, the characteristic pattern of the curves in fig. 5.3.21 and 5.3.22 is found again. This gives strong evidence that the obtained results are correct. It is difficult to interpret these results. Again, it is brought forward that these results can be explained by local differences in the fibre texture and the amorphous matrix.

Strong influence of the fibre texture on the strain field was shown with numerical simulations of such experiments (Roddeman, 1988).

Summarizing, it is stated that the results obtained from measurements with buckle transducers agree well (in a qualitative sense) with those obtained from strain field measurements.

With this type of boundary conditions the inhomogeneous mechanical properties of a specimen can be demonstrated clearly.

It is shown that the mechanical behaviour of even simply shaped specimens, loaded with simple boundary conditions, can be very complicated. This can have far-reaching consequences. For instance, if few markers are applied, then the obtained results can be largely dependent on the position of the markers on the specimen (the ratio between the global maximum at the left and the global minimum at the right in fig. 5.3.21 is 1.43 (0.06)). The classical way of obtaining material properties fails. Detailed knowledge of the structure of the object has to be incorporated in the analyses.

Obviously, more experiments are needed to increase the understanding of the mechanical behaviour of this type of soft tissue. However, it is noted that support of and interaction with numerical simulations is of prime importance. With the aid of numerical simulations the influence of different parameters can be examined faster and in more detail (Roddeman, 1988). Besides, they may give indications where to focus on in future measurements.

### 5.3.3 Biaxial testing

The effect of biaxial testing was studied on a specimen obtained from the intermuscular septa from between the *digiti minimi* and *extensor digitorum* muscle on one side, and the *extensor carpi ulnaris* muscle on the other. Collagenous fibres were in a parallel fashion. The proximal side was clamped; on the distal side four load strips were prepared. The specimen was equipped with four buckle transducers, three groups of markers, and on both transversal sides a number of hooks (fig. 5.3.25). Because both markers and buckle transducers are applied, the number of markers is restricted. Hence statements about the strain field can not be as detailed as for the uniaxial load cases described in section 5.3.2.

Between the part of the specimen to be tested and the clamp the proximal ending of the *digiti minimi* muscle is indicated in fig. 5.32. The specimen seemed to be double layered from this point in proximal direction (the clamped side). The group of markers on the second layer was meant to check for interaction between the two layers. As the strain distributions measured with these markers were

negligible compared to those measured with the other two groups, interaction was considered to be of no importance and these markers are not taken into consideration in the following.

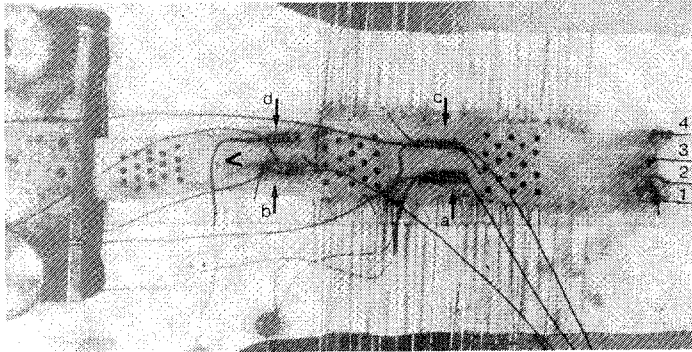


Fig. 5.3.25 The specimen for biaxial testing in the set-up. The buckle transducers are indicated with characters. The proximal ending of the *digiti minimi* muscle is indicated with (<).

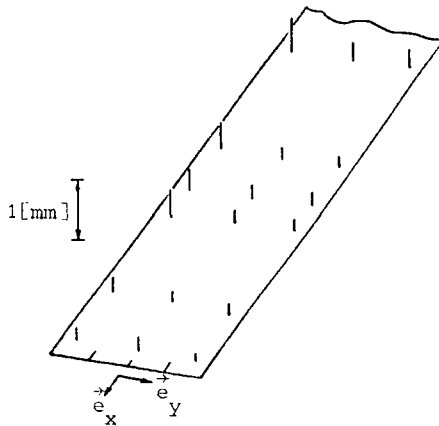


Fig. 5.3.26 Thickness chart of the specimen.

A thickness chart of the biaxially loaded part of the specimen is given in fig. 5.3.26. Transverse to the fibre direction, two types of boundary conditions have been applied:

- Loading both sides with a low, distributed, approximately constant, load ( $0.03 \text{ [N/mm]}$ ). This caused the specimen to widen about 40%. This loaded state was chosen as the reference configuration.
- Suppressed displacement.

Fig. 5.3.27 and fig. 5.3.28 show the strain distributions and the positive principal strains, respectively, for three load cases:

- Transverse as well as longitudinal, a distributed constant load (load case 1).

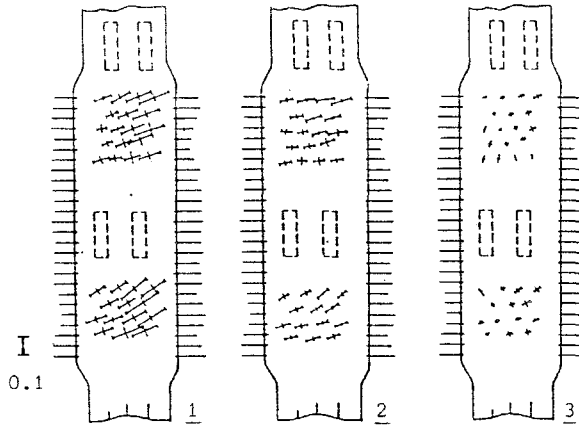


Fig. 5.3.27 The strain distribution for the three biaxial load cases 1,2 and 3, respectively (see text).

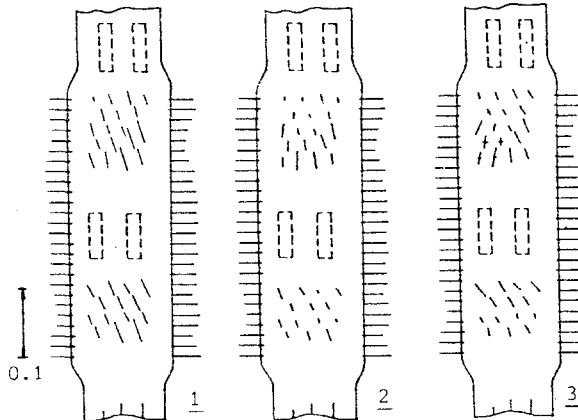


Fig. 5.3.28 The distribution of the positive principal strains for the three biaxial load cases 1,2 and 3, respectively (see text).

- Tensile test conditions with distributed, constant transverse load (load case 2).
- Tensile test conditions with suppressed transverse displacement (load case 3).

All plots refer to the maximum longitudinal load (20[N]). The following is observed:

- There is no such similarity for the strain distributions for load cases 1 and 2 as was observed for the corresponding load cases 5 and 6 for the previous experiment (section 5.3.2, fig. 5.3.16).

- Suppressed transverse displacement does not mean zero transverse strain everywhere in the specimen. On the contrary, both positive and negative transverse strains are found.

Also the mean of the measured transverse strain components turns out to be non-zero ( $p < 0.05$ ,  $\sigma(E_{yy}) = 0.005$ ). The mean transverse strains for the three load cases and for all load levels are given in table 5.1. It was checked that no tear of the tissue occurred around the hooks which might have been the cause for the measured strains.

Table 5.1

The mean transverse strains ( $n=33$ ) for three load cases (see text). All numbers in this table should be multiplied with  $10^{-3}$ .

load case	1	2	3
load[N]	Mean transverse strain		
4	-58	-21	-2
12	-95	-51	-2
20	-125	-77	-9

The results obtained with the buckle transducers showed no significant difference between load case 2 and 3 at any applied load level. As a drop of about 90% (see table 5.1) in the transverse strain gives no significant measurable changes in the load transfer, prescribing uniform displacement seems not very suitable to establish the interaction between longitudinal and transverse strains, at least for the tissue under investigation. The differences between load case 1 and load cases 2 and 3, respectively, are shown in fig. 5.3.29.

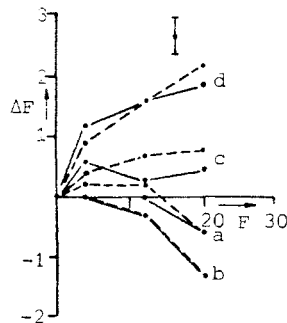


Fig. 5.3.29 Differences  $\Delta F$ [N] between the measured local forces of load case 1 and 2 (—) and load case 1 and 3 (----), respectively, as a function of the loading force  $F$ [N]. The characters indicate the transducers (see fig. 5.3.25).

The differences observed agree with measured thickness variations: the thicker part at the left side of the specimen (where also transducers a and b are installed, see fig. 5.3.25 and 5.3.26) transfers a bigger amount of the total load under tensile test conditions.

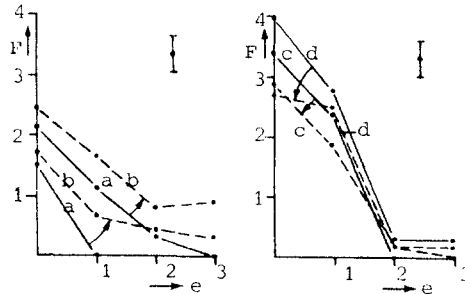


Fig. 5.3.30 Change of the measured local forces caused by suppressing the transverse displacements as a function of the eccentricity (see page 5.10). The characters indicate the transducers (see fig. 5.3.25).

The results obtained from the buckle transducers for local loading are given in fig. 5.3.30. It is important to notice that in fig. 5.3.30a and b, due to suppressing the transverse displacements, the local peak forces (transducers c and d) are decreased and thus the load is more spread over the fibres.

Biaxial loading, for a tissue with a very high transverse compliance, seems to be possible within limits. The effect of biaxial loading is best demonstrated for local loading when suppressing transverse displacements (and starting with a large prescribed transverse strain). Biaxial testing with prescribed uniform displacements as boundary conditions seems not suitable for determination of parameters that describe the interaction between longitudinal and transverse strains.

#### 5.3.4 In situ strain measurements

For the in vitro loading of tissue samples it turned out that, even for simple boundary conditions, the mechanical behaviour of the tissue is complicated. However, these measurements do not give any information on the "natural" state of loading. This raises the question if the occurring stress and strain fields are also that complicated when the connective tissue structure under investigation is loaded in vivo. That is why, as a pilot study, in situ strain measurements were performed.

It is felt that loading the structure by means of the tendons via the muscular fibres, although far from reality, is at this moment the best way to approach the in vivo loading configuration. The occurring stress and strain fields strongly depend on where muscles attach to the septa and if they are jointly or separately active. Thus, it is important to take into account a precise description of the anatomical relations between muscles and their area of attachment to the septa. With the experiments described here, the septa between the extensor digitorum muscle (E.D.M) and supinator muscle (S.M) on one side and the extensor carpi radialis brevis muscle (E.C.R.B.M) on the other, are chosen to examine these phenomena. There are reasons to assume that the E.D.M, in contrary to what its name suggests, can not be regarded as one muscle (van Mameren, 1987). Each of the four tendons of the E.D.M is related to a separate muscle and each muscle has a well defined area of attachment to the connective tissue structure. Such a description of the E.D.M can, to the best of our knowledge, not be found in literature. Therefore, the experiments have two objectives:

- to gain insight in the value of the in vitro experiments to obtain indications on how to perform these experiments, and where attention should be focused on in the future
- to test that the E.D.M has to be described in terms of four separate muscles. When this is true, by loading the tendons of these muscles separately, only a part of a septum will be loaded and this will lead to a, for each muscle specific, inhomogeneous strain field.

A right arm (male) was dissected. All muscles were removed except for:

- the extensor digitorum muscle (E.D.M)
- the extensor digiti minimi muscle (E.D.M.M)
- the extensor carpi ulnaris muscle (E.C.U.M)
- the anconeus muscle (A.M)
- the supinator muscle (S.M)

Also the hand was removed. The interosseus membrane and the retinacula at the wrist were left unimpaired. In this way two septa, between E.D.M and S.M on one side and the extensor carpi radialis brevis muscle (E.C.R.B.M) on the other, became visible. The septum overlying the S.M is not attached to that muscle (for reasons of convenience this septum is called the E.S. septum; the septum from between the E.D.M and the E.C.R.B.M is called the E.D. septum). The two septa are strongly connected to each other, their fibres become intertwined where they meet.

Markers were mounted on both septa. A picture of the dissected arm with the markers is given in fig. 5.3.31. The distal part of the humerus was cast in a stainless steel bone box with a rapidly hardening polymer (Fastacryl). The arm was placed in the experimental set-up as shown in fig. 5.3.32. In this figure also the two septa are indicated with dash lines. In fig. 5.3.33. the areas of attachment on the E.D. septum of the muscles corresponding to the tendons of the

index and middle finger are indicated. The edge of the fascia overlying the E.D.M. was drawn back with a series of hooks and threads which were "minimally loaded" ( $0.06[N]/\text{thread}$ ). This was

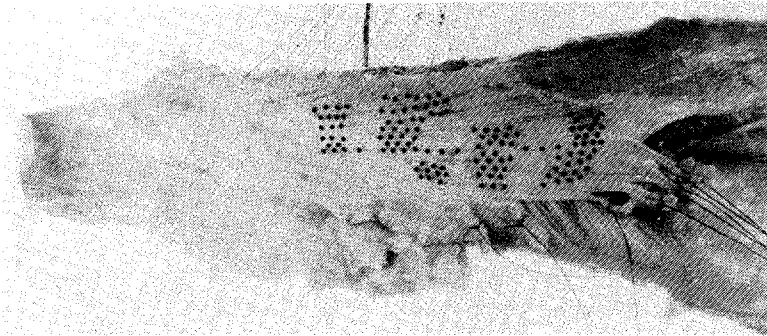


Fig. 5.3.31. A dissected right arm with markers for strain measurement

done to prevent the E.D. septum to rotate out of view or to wrinkle when loaded. This "minimal loaded state" is, in the following, called the unloaded state of the E.S. septum. To define a reference state for the loosely hanging E.S. septum, eight threads were mounted to load strips prepared on the distal side of this septum. These threads, directed such that the natural form of the E.S. septum was approached, could be minimally loaded ( $0.06[N]/\text{thread}$ ) or loaded with equal forces ( $1.5[N]/\text{thread}$ ). Radius and ulna were in maximal supination and prevented to rotate. The elbow joint was about  $45^{\circ}$  in flexion. When tendons were loaded, it was assured that they were as close to the wrist as possible.

The results presented reflect to the following load cases:

- Loading of the tendon of the index finger
- Loading of the tendon of the middle finger
- Loading of the tendons of the index and the middle finger simultaneously

They correspond to a load level of  $5[N]/\text{tendon}$ . The three load cases are performed once while the E.S. septum was unloaded and once when this septum was loaded. To facilitate comparison, strain distributions for the same load case and the E.S. septum once unloaded and once loaded are depicted two and two. These results are representative for other load levels. Problems occurred at high load levels ( $20[N]/\text{tendon}$ ) as the E.D. septum wrinkled and markers disappeared in the folds. Similar measurements were carried out for loaded tendons of the ring and middle finger. However, as no significant strains were detected in the E.D. and E.S. septa for these load cases, which is in agreement with the anatomical



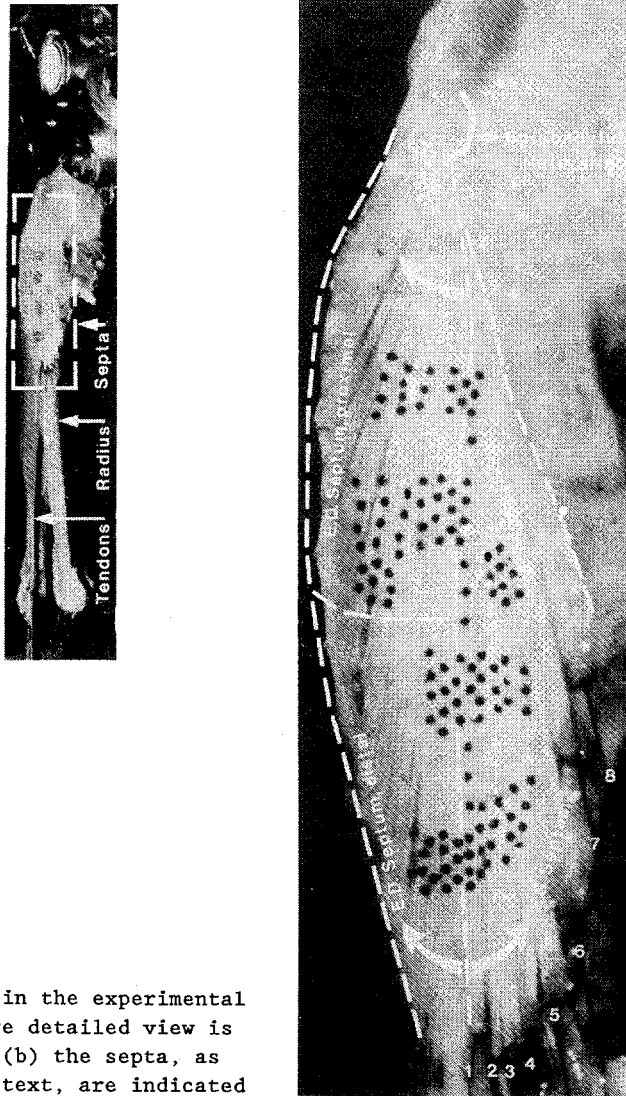


Fig. 5.3.32

The prepared arm in the experimental set-up (a). A more detailed view is given in (b). In (b) the septa, as described in the text, are indicated with dash lines.

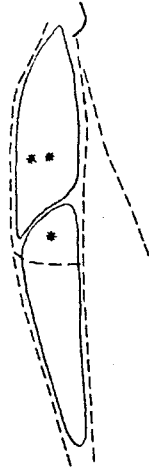


Fig. 5.3.33 The areas of attachment on the E.D. septum of the muscles corresponding to the tendons of the index finger (\*) and the middle finger (\*\*) (compare with fig. 5.3.32).

architecture of the E.D.M, the results of these measurements are omitted here. The strain distributions are shown in figs. 5.3.34-5.3.36. Fig. 5.3.37 gives the strain distribution when loading the E.S. septum while all tendons are unloaded. For the proximal part of the E.D. septum, the positive principal strains are given separately. In all figures the septa are indicated with dash lines according to fig. 5.3.32 and the fibre direction is indicated with dot and dash lines.

It is premature to draw far-reaching conclusions from these results. However, the following can be observed, when looking at the presented figures:

- Loading of the E.S. septum causes only positive strains in the E.D. septum transverse to the fibre direction (see fig 5.3.37).
- When tendons are loaded separately, the strain distributions are inhomogeneous. This indicates that also in vivo the mechanical behaviour of the structure is complicated.
- There is a strong resemblance between the strain distributions at the proximal part of the E.D. septum for the loaded and unloaded state of the E.S. septum when both index and middle finger are loaded. There is also resemblance, but not that strong, when tendons are loaded separately. For all load cases, there is a strong resemblance for the areas where small positive principal

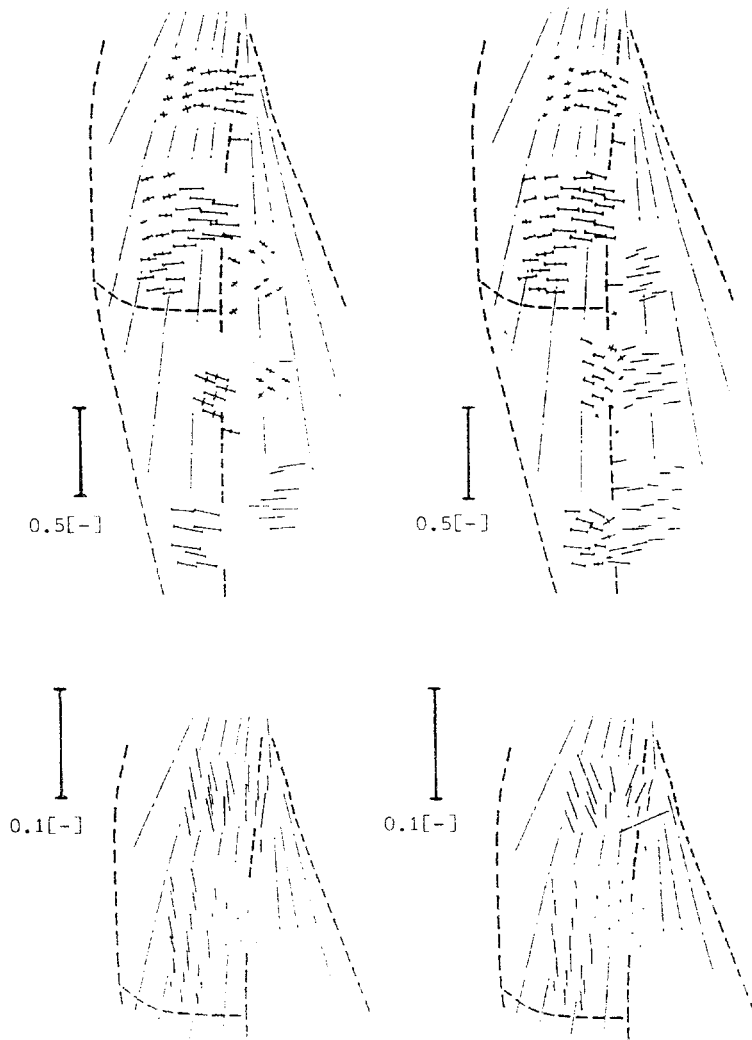


Fig. 5.3.34 The strain distributions for loading of the index finger tendon

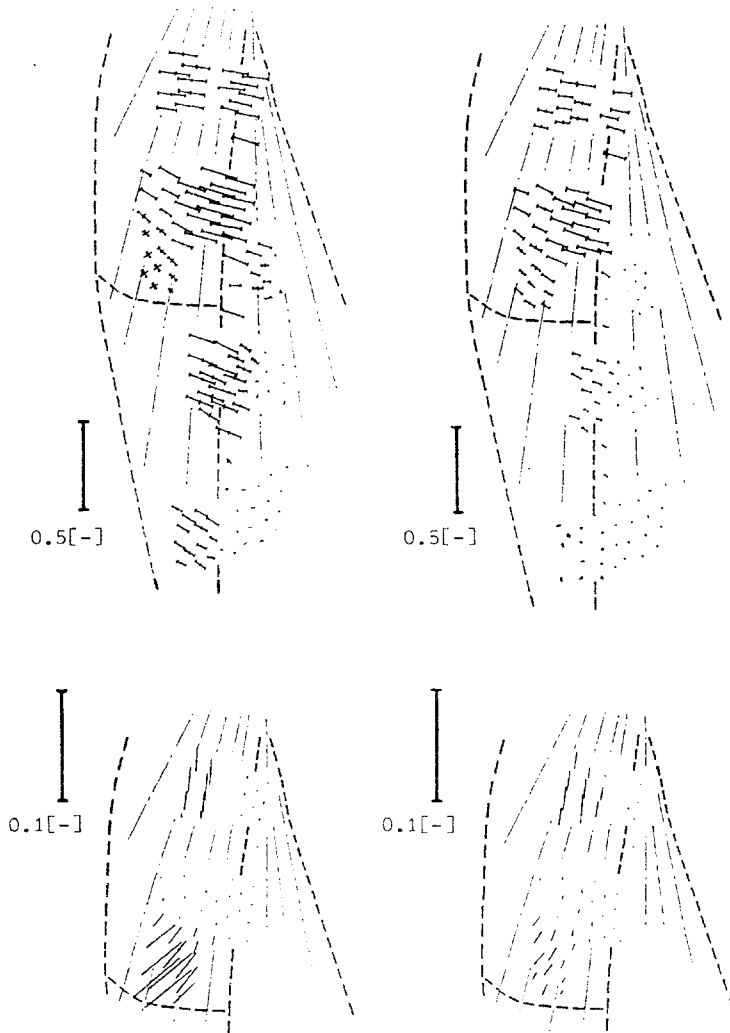


Fig. 5.3.35 The strain distributions for loading of the middle finger tendon.

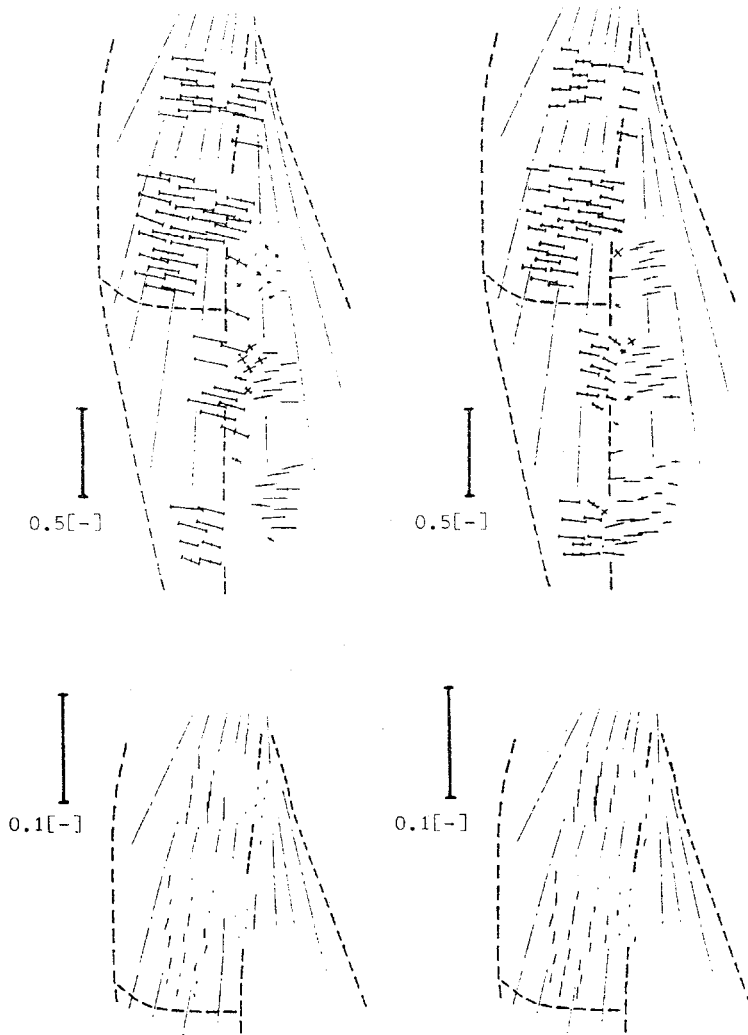


Fig. 5.3.36 The strain distributions for loading of the index and the middle finger tendon.

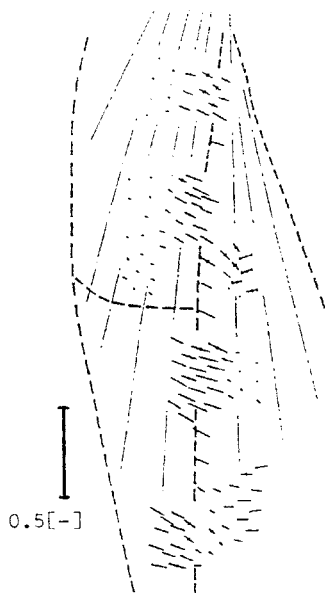


Fig. 5.3.37 The strain distribution for loading of the E.S. septum and unloaded finger tendons.

strains are found. The latter reminds of the global maxima and minima in the strain field as were observed with the experiments on inhomogeneous properties (section 5.3.2, fig. 5.3.19-5.3.22).

- The 'shift to the left' of the positive principal strains when the tendon of the middle finger is loaded, agrees with the area where the muscle fibres, corresponding to this tendon, attach to the E.D. septum. The shear in the E.D. septum (principal strains which are rotated with respect to the fibre direction) indicates, that different parts of the septum are loaded when different tendons are loaded. This affirms the anatomical description of the E.D.M in terms of four separate muscles.
- The points between the E.S. and the E.D. septum where, with respect to the fibre direction, a state of pure shear is observed, indicate little load transfer in the distal part of their interface.
- For both the state of loaded and unloaded E.S. septum, the cases for which the index and middle finger tendon are loaded simultaneously, a strain distribution is found for which the directions of the positive principal strains almost coincide with the local fibre directions.
- The most regular strain distribution is obtained when both index and middle finger tendon and the E.S. septum are loaded.

It is concluded that in situ strain distribution measurement on the 3-dimensional connective tissue structure under investigation is

feasible for those parts which can be brought in sight. However, again it is noted that a more precise and quantitative description of the fibre texture seems to be of major importance to attain more information from these types of experiments.





---

## 6. SUMMARY AND CONCLUDING REMARKS

---

In the present thesis the development and design of tools for the measurement of stress and strain fields in soft tissue are dealt with. Elaborate attention is paid to the theoretical modeling and design improvements of these tools. They are used to investigate the load transmission through collagenous connective tissue structures from the cubital regio.

For the stress measurement, the well-known principle of the buckle transducer is used (chapter 2). The application of a buckle transducer for stress measurement has the important advantage that the mechanical properties of the material need not to be known. At least, if the design and the installation of the transducer meet certain conditions. Existing designs are prevented from a successful application towards our objective by three major disadvantages:

- The large size and a wrong shape which give false input sources.
- Poor definition of the mutual position of parts of the transducer and the tissue when installed.
- Time dependence of the output signal.

Improvements with regard to these disadvantages resulted in a redesigned buckle transducer which is believed to be an improvement compared to earlier designs.

The strain field measurements (chapter 3) are based on the application of an image recording system with which the spatial coordinates of the centroids of a large number of markers, mounted on the object under investigation, are reconstructed. From the mutual displacement of the centroids, the components of the deformation tensor  $F$  for each material point, defined by a marker, are estimated. With these estimates, components of a strain tensor can be determined. Here, the Green-Lagrange strain tensor is chosen. Special attention is paid to the measurement of strain fields on curved surfaces and on the identification of markers from different object configurations.

Mathematical models which describe the different stages of the measurements are shown to be essential for design for accuracy and for a correct interpretation of the measuring results. It is shown that accuracy is not an invariable property of the measuring system but can be adapted to each individual experiment and, moreover, the accuracy depends on the real deformation field. A method to correct for systematic errors is given in section 3.5.1. The influence of random errors, mainly caused by discretization of images, on the estimated components of the deformation tensor and strain tensor is discussed in section 3.5.2.

From test measurements (chapter 4) it appeared that the obtainable accuracy for given test conditions can be predicted very well with the aid of the theoretical models.

Different types of experiments on the collagenous connective tissue from the cubital regio, with application of the tools mentioned, are discussed in chapter 5. The proportion and texture of the collagen fibres, the amorphous matrix and a precise knowledge of the boundary conditions are considered as the important mechanical parameters. The collagen contents is related to the thickness of the tissue.

Therefore, an intuitively based method for local thickness measurement is proposed which uses an indenter to exclude for the fluid-like, non load-bearing substances.

To demonstrate the mechanical properties of the tissue to their full extent and gaining a maximum of insight, experiments with uniform as well as non-uniform boundary conditions were done. Three experiments were performed on tissue samples. They concern:

- The impact of the high anisotropy caused by the fibre texture.
- The inhomogeneous properties of the tissue.
- The effects of biaxial loading.

Anisotropy causes load transfer to be restricted to the loaded fibres and the fibres in the vicinity of these. Saint-Venant's principle, important in engineering practice, is no longer valid.

The experiments on inhomogeneous mechanical properties proved that, even for simply shaped tissue samples and uniform boundary conditions, the mechanical behaviour of the tissue is complicated. The inhomogeneous properties were most clearly demonstrated when the specimen was loaded with non-uniform boundary conditions.

With biaxial testing, it was found that the effect of non-uniform boundary conditions was most clear. In terms of reducing peak stresses, the load was more efficiently distributed over the specimen when the transverse displacement was prescribed. No such effect was measured, within the measuring accuracy, for tensile test conditions. Biaxial testing with uniform boundary conditions seems not very suitable to establish the interaction between longitudinal and transverse strains for this type of tissue.

In situ strain measurements were performed to gain insight in the "natural" state of loading of the connective tissue structure. These measurements concerned the septa from between the extensor carpi radialis brevis muscle on one side and the extensor digitorum (E.D. septum) and supinator muscle (E.S. septum) on the other. A second objective of these experiments was to test if the description of the extensor digitorum muscle in terms of four separate muscles is valid. The E.D. septum was loaded by means of the finger tendons via the muscle fibres, the E.S. septum by means of threads. It was demonstrated that measured strain distributions agree with this modified anatomical description of the extensor digitorum muscle. The

strain distribution was most regular when both the tendons of index and middle finger as well as the E.S. septum were loaded. In situ strain distribution measurements on 3-dimensional soft tissue structures are shown to be feasible for those parts which can be brought in sight.

The present research may be regarded as a contribution to a further understanding of the mechanical behaviour of soft tissues. With the parameters that are considered as to determine the mechanical behaviour of the tissue under investigation, for quasi-static loading the measured phenomena can partially be interpreted in a qualitative way. However, it is felt that more measurements, detailed information on the fibre texture and further development of the thickness measurement method are indispensable to come to full understanding. Moreover, for a quantitative description of the mechanical behaviour in terms of stress and strain as function of the parameters involved, the interaction between experiments and numerical simulations of these experiments with aid of continuum mechanics is essential.



## References

- Abdel-Aziz, Y.I., Karara, H.M.: "Direct linear transformation from comparator coordinates into object space coordinates in close-range photogrammetry", Symp. on close photogrammetry, Urbana, Illinois, pp. 1-18, Jan. 26-29, 1971.
- Arms, S., Boyle, J., Johnson, R., Pope, M.: "Strain measurement in the medial collateral ligament of the human knee: An Autopsy study", J. Biomechanics, Vol. 16, No. 7, pp. 491-496, 1983.
- Barnes, G.R.G., Pinder, D.N.: "In vivo tendon tensions and bone strain measurements and correlation", Journal of biomechanics, Vol. 7, pp. 35-42, 1974.
- Barry, D., Ahmed, A.M.: "Design and performance of a modified buckle transducer for the measurement of ligament tension", J. Biomechanical Engineering, Vol. 108, May 1986.
- Bopp, H., Krauss, H.: "An orientation and calibration method for non-topographic applications", Photogrammetric Engineering and Remote Sensing, Vol. 44, No. 9, pp. 1191-1196, September 1978.
- Butler, D.L., Noyes, F.R., Grood, E.S.: "Measurement of the biomechanical properties of ligaments", CRC Handbook on Engineering and Biology, Vol 1B, Edited by Bahnuik, G. and Burstein, A., pp. 279-314, 1978.
- Butler, D.L., Grood, E.S., Noyes, F.R., Zernicke, R.F., Brackett, K.: "Effects of structure and strain measurement technique on the material properties of young human tendons and fascia", J. Biomechanics, Vol. 17, No. 8, pp. 579-596, 1984.
- Doebelin, E.O.: "Measurement systems, application and design", Third Edition, McGraw-Hill International Book Company, 1983.
- Doornbos, R.: "Statistische theorie van proefopzetten", dictaat 2222, University press, Eindhoven, 1980.
- Drukker, J., Jansen, J.C.: "Compendium anatomie", De tijdstroom, Lochum, 1975.
- Ellis, D.G.: "Cross-sectional area measurement for tendon specimens: A comparison of several methods", J. Biomechanics, Vol. 2, pp. 175-186, 1969.
- Erdman, A.G., Mayfield, J.K., Dorman, F., Wallrich, M., Dahlof, W.: "Kinematic and kinetic analysis of the human wrist by stereoscopic instrumentation", J. Biomechanical Engineering, Vol. 101, May 1979.

- Faig, W.: "Calibration of close-range photogrammetric cameras", Symp. on close photogrammetry, Urbana, Illinois, pp. 111-131, Jan. 26-29, 1971.
- Ferrigno, G., Pedotti, A.: "Elite: A digital dedicated hardware system for movement analysis via real-time TV signal processing, IEEE transactions on biomedical engineering, Vol. BME-32, No. 11, November 1985.
- Fioretti, S., Germani, A., Leo, T.: "Stereometry in very close-range stereophotogrammetry with non-metric cameras for human movement analysis", J. Biomechanics, Vol. , No. , pp. 831-842, 1985.
- Ghosh, S.K.: "Some photogrammetric considerations in the application of scanning electron micrographs", Symp. on close photogrammetric systems, Champaign, Illinois, pp. 321-334, July 28 - Aug. 1, 1975.
- Hasberry, S., Pearcy, M.J.: "Temperature dependence of the tensile properties of interspinous ligaments of sheep", J. Biomedical Engineering, 1986, Vol. 8, January.
- Hoffman, A.H., Grigg, P.: "A method for measuring strains in soft tissue", J. Biomechanics. Vol. 17, No. 10, pp. 795-800, 1984.
- Hubbard, R.P., Soutas-Little, R.W.: "Mechanical properties of human tendon and their age dependence", J. Biomechanical Engineering, Vol. 106, May 1984.
- Humphrey, J.D., Vawter, D.L., Vito, R.P.: "Quantification of strains in biaxially tested soft tissues", J. Biomechanics, Vol. 20, No. 1, pp. 59-65, 1987.
- Hunter, S.C.: "Mechanics of continuous media", second edition, John Wiley & Sons, New York, 1983.
- Karara, H.M.: "Close-Range photogrammetry: where are we and where are we heading". Photogrammetric engineering and remote sensing, Vol. 51, No. 5, pp. 537-544, May 1985.
- Kastelic, J., Baer, E.: "Deformation in tendon collagen", in: "The mechanical properties of biological materials", Symposia of the society for experimental biology, Cambridge University press, Cambridge, 1980.
- Kreyszig, R.: "Advanced engineering mathematics", fifth edition, John Wiley and sons, New York, 1983

- Lewis, J.L., Frasier, G.: "On the use of buckle transducers to measure knee ligament forces", Proceedings of the 1979 ASME Biomechanics Symposium, pp. 71-74, 1979.
- Lewis, J.L., Lew, W.D., Schmidt, J.: "A note on the application and evaluation of the buckle transducer for knee ligament force measurement", Journal of Biomechanical Engineering, Vol. 104, pp. 125-128, 1982.
- Mameren van, H., Drukker, J.: "A functional anatomical basis for injuries to the ligamentum and other soft tissues around the elbow joint: transmission of tensile and compressive loads", Int. J. Sports Med., 5, pp. 88-92, supplement, 1984.
- Mameren van, H.: Personal communications march 1987.
- Marzan, G.T., Karara, H.M.: "A computer program for direct linear transformation solution of the colinearity condition and some applications of it", Symp. on close range photogrammetric systems, Champaign, Illinois, July 28 - Aug. 1, 1975.
- Mizrahi, J., Karni, Z.: "Isotropy and anisotropy of uterine muscle during labor contraction", J. Biomechanics, Vol. 13. pp. 211-218, 1980.
- Morris : " Human anatomy: A complete systematic treatise", edited by: Anson, B.J., MacGraw-Hill, 1966
- Oomens, C.W.J.: "A mixture approach to the mechanics of skin and subcutis", Thesis, Eindhoven University of Technology, the Netherlands, 1985.
- Panjabi, M.M., Krag, M., Summers, D., Videman, T.: "Biomechanical time-tolerance of fresh cadaveric human spine specimens". J. Orthopaedic Research, Vol. 3, No. 3, 1985.
- Peters, G.W.M., Sauren, A.A.H.J., Mameren, van H.: "Redesign and development of a force transducer of the buckle type", Experimental Stress Analysis, ISBN 90-247-3346-4, Wieringa, H. (ed), pp. 141-150, 1986.
- Peters, G.W.M., Mameren, van H., Sauren, A.A.H.J.: "A force transducer of the buckle type for measuring tensile forces in collagenous structures of small size", Anat. anz., 1987, in press.
- Prinzen, T.T., Arts, T., Prinzen, F.W., Reneman, R.S.: "Mapping of epicardial deformation using a video processing technique", J. Biomechanics, Vol. 19, No. 4, pp. 263-273, 1986.

- Riemersma, D.J.: "Biomechanics of the digital tendons in the equine hindleg", Thesis University of Utrecht, the Netherlands, 1986.
- Roddeman, D.G., Drukker, J., Oomens, C.W.J., Janssen, J.D.: "The wrinkling of thin membranes: part 1 - theory", ASME Journal of applied mechanics, vol. 54, 1987.
- Roddeman, D.G., Drukker, J., Oomens, C.W.J., Janssen, J.D.: "The wrinkling of thin membranes: part 2 - numerical analysis", ASME Journal of applied mechanics, vol. 54, 1987.
- Roddeman, D.G., van Hout, M.G., Oomens, C.W.J., Janssen, J.D., Drukker, J.: "The wrinkling of thin membranes: comparison between experiments and theory", proceedings ASME biomechanics symposium, Cincinatti, 1987.
- Roddeman, D.G.: "Force transmission in wrinkeling membranes -a numerical tool to study connective tissue structures-", Thesis, Eindhoven University of Technology, the Netherlands, to be published, january, 1988.
- Ross, C., Clawson, D.K.J.: "The musculoskeletal system in health and disease", Harpor and Row publishers, 1980.
- Salmons, S.: "The 8th international conference on medical and biological engineering-meeting report, Bio-medical Engineering, Vol. 4, pp. 467-474, 1969.
- Sauren, A.A.H.J.: "The mechanical behaviour of the aortic valve", Thesis, Eindhoven University of Technology, the Netherlands, 1981.
- Scales, L.E.: "Introduction to non-linear optimization", Macmillan, London, 1985.
- Schweppe, F.C.: "Uncertain dynamical systems", Prentice Hall, Englewood Cliffs, New Jersey, 1973.
- Schwedfsky, Ackermann: "Photogrammetry", B.G. Teubner, Stuttgart, 1976.
- Seirey, A., Gray, W.: "A feasibility study for the use of a silastic gage as an in vivo muscle force transducer, J. Bioengineering Vol. 2, pp. 159-166, 1978.
- Shoemaker, P.A., Schneider, D., Lee, M.C., Fung, Y.C.: "A constitutive model for two-dimensional soft tissues and its application to experimental data. J. Biomechanics, Vol. 19, No. 9, pp 695-702, 1986.



- Stone, J.E., Madsen, N.H., Milton, J.L., Swanson, W.F., Turner, J.L.: "Developments in the design and use of liquid-metal strain gages", Exp. Mechanics, June 1983.
- Viidik, A., Vaust J.: "Biology of collagen", Academic press, New York, 1980.
- Vossoughi, J.: "Thickness measurement for soft materials". Experimental Techniques, pp. 32-33, sept. 1984.
- Walmsley, B., Hodgson, J.A., Burke, R.E.: "Force produced by medial gastronimius and soleus muscles during locomotion in freely moving cats", Journal of Neurophysiology, Vol. 41, pp. 1203-1216, 1978.
- Warwick, R., Williams, P.L.: "Gray's Anatomy", 35th edition, Longman, london, 1973.
- Woo, S.L-Y.: "Biomechanics of tendons and ligaments", in: "Frontiers in biomechanics", pp. 180-209, edited by: Schmid-Schönbein, G.W., Woo, S.L-Y., Zweifach, B.W., Springer Verlag, New York, 1986.
- Woo, S.L-Y., Orlando, C.A., Camp, J.F., Akeson, W.H.: "Effects of postmortem storage by freezing on ligament tensile behaviour", J. Biomechanics, Vol. 19, No. 5, pp. 399-404, 1986.
- Woo, S.L-Y., Orlando, C.A., Gomez, M.A., Frank, C.B., Akeson, W.H.: "Tensile properties of the Medial Collateral ligament as a function of Age", J. Orthopaedic Research, Vol. 4, No. 2, pp. 133-141, 1986.
- Wood, G.A., Marshall, R.N.: "The accuracy of DLT extrapolation in three-dimensional film analysis", J. Biomechanics, Vol. 19, No. 9, pp. 781-785, 1986.
- Zernicke, R.F., Butter, D.L., Grood, E.S., Hefzy, M.S.: "Strain topography of human tendon and fascia", J. Biomechanical Engineering, Vol. 106, May 1984.
- Zienkiewicz, A.C.: "The finite element method", third edition, McGraw-Hill, London, 1977.



## Appendix A

In this appendix a method is described for the reconstruction of the object space coordinates of markers which is based on the method of least squares.

The method described in section 3.2.2 is based on statistical considerations. The logical reason for that is the fact that image plane coordinates are observations which contain a random error. However, such an approach obliges to make assumptions about the statistical properties of these errors.

The necessity for these assumptions lapses if one starts with a more intuitive judgement on what is a good estimate  $\underline{X}$ . Therefore we rewrite (3.13) in the form:

$$\underline{A}(\underline{x}) \cdot \underline{X} + \underline{x} = 0 \quad (\text{A.1})$$

where:

$$\underline{A}(\underline{x}) = \begin{bmatrix} \frac{x_{12}}{a} & -1 & 0 \\ \frac{x_{13}}{a} & 0 & -1 \\ -1 & \frac{x_{21}}{a} & 0 \\ 0 & \frac{x_{23}}{a} & -1 \end{bmatrix} \quad (\text{A.2})$$

$$\underline{X}^T = [X_1, X_2, X_3] \quad (\text{A.3})$$

$$\underline{x}^T = [x_{12}, x_{13}, x_{21}, x_{23}] \quad (\text{A.4})$$

A set of observations  $\bar{\underline{x}}$  will, in general, not satisfy (A.1) due to the random errors contained in  $\bar{\underline{x}}$ . For that reason we write, instead of (A.1):

$$\underline{A}(\bar{\underline{x}}) \cdot \underline{X} + \underline{x} = \bar{\underline{u}} \quad (\text{A.5})$$

where  $\bar{\underline{u}}$  is a column matrix which contains the residuals of the four equations given by (A.5):

$$\bar{\underline{u}}^T = [\bar{u}_{12}, \bar{u}_{13}, \bar{u}_{21}, \bar{u}_{23}] \quad (\text{A.6})$$

We define a quadratic function  $J(\underline{X}, \underline{x})$  of  $\underline{X}$ , where  $\underline{x}$  is a given set of observations, by:

$$J(\underline{X}, \underline{x}) = (\underline{A}(\underline{x}) \cdot \underline{X} + \underline{x})^T \cdot (\underline{A}(\underline{x}) \cdot \underline{X} + \underline{x}) \quad (\text{A.7})$$

an determine the estimate  $\hat{\underline{X}}$  such that  $J(\underline{X}, \underline{x})$  is minimized; thus:

$$\underline{J}^{(1)}(\hat{\underline{x}}, \underline{x}) = \frac{\partial J(\underline{x}, \underline{x})}{\partial \underline{x}} \Big|_{\underline{x} = \hat{\underline{x}}} = 0 \quad (\text{A.8})$$

A straightforward calculation leads to:

$$\hat{\underline{x}} = - [\underline{A}^T(\underline{x}) \cdot \underline{A}(\underline{x})]^{-1} \cdot \underline{A}^T(\underline{x}) \cdot \underline{x} \quad (\text{A.9})$$

Expression (A.9) is an explicit function for the estimate  $\hat{\underline{x}}$  which is rather simple compared to (3.24); it can be worked out analytically. This makes the determination of  $\hat{\underline{x}}$  very efficient as concerned to computing time. From (A.2) it follows:

$$\underline{A}^T(\underline{x}) \cdot \underline{A}(\underline{x}) = \begin{bmatrix} \frac{x_{12}^2}{a^2} + \frac{x_{13}^2}{a^2} + 1 & - \left( \frac{x_{12}}{a} + \frac{x_{21}}{a} \right) & - \frac{x_{13}}{a} \\ \text{symm.} & \frac{x_{21}^2}{a^2} + \frac{x_{23}^2}{a^2} + 1 & - \frac{x_{23}}{a} \\ & & 2 \end{bmatrix} \quad (\text{A.10})$$

And from (A.2) and (A.4)

$$\underline{A}^T(\underline{x}) \cdot \underline{x} = a \begin{bmatrix} \frac{x_{12}^2}{a^2} + \frac{x_{13}^2}{a^2} - \frac{x_{21}}{a} \\ \frac{x_{21}^2}{a^2} + \frac{x_{23}^2}{a^2} - \frac{x_{12}}{a} \\ - \left( \frac{x_{13}}{a} + \frac{x_{13}}{a} \right) \end{bmatrix} \quad (\text{A.11})$$

With  $\underline{A}^T(\underline{x}) \cdot \underline{A}(\underline{x}) \cdot \hat{\underline{x}} = - \underline{A}^T(\underline{x}) \cdot \underline{x}$  one can easily derive:

$$\hat{x}_3 = \frac{1}{2} [x_{13} (1 + \frac{\hat{x}_1}{a}) + x_{23} (1 + \frac{\hat{x}_2}{a})] \quad (\text{A.12})$$

and:

$$\begin{bmatrix} \frac{x_{12}^2}{a^2} + \frac{x_{21}^2}{a^2} + 1 & - \left( \frac{x_{12}}{a} + \frac{x_{21}}{a} \right) \\ - \left( \frac{x_{12}}{a} + \frac{x_{21}}{a} \right) & \frac{x_{21}^2}{a^2} + \frac{x_{23}^2}{a^2} + 1 \end{bmatrix} \cdot \begin{bmatrix} \hat{x}_1 \\ \hat{x}_2 \end{bmatrix} = - a \begin{bmatrix} \frac{x_{12}^2}{a^2} + \frac{x_{13}^2}{a^2} - \frac{x_{21}}{a} \\ \frac{x_{21}^2}{a^2} + \frac{x_{23}^2}{a^2} - \frac{x_{12}}{a} \end{bmatrix} + \hat{x}_3 \begin{bmatrix} \frac{x_{13}}{a} \\ \frac{x_{23}}{a} \end{bmatrix} \quad (\text{A.13})$$

Substitution of (A.12) into (A.13) gives, after some manipulations:

$$\begin{matrix} \hat{X}_1 \\ \hat{X}_2 \end{matrix} = -\frac{a}{Q} \begin{bmatrix} a_{11} & a_{12} \\ a_{21} & a_{22} \end{bmatrix} \cdot \begin{bmatrix} b_1 \\ b_2 \end{bmatrix} \quad (\text{A.14})$$

where:

$$a_{11} = \left(\frac{x_{21}}{a}\right)^2 + \frac{1}{2} \left(\frac{x_{23}}{a}\right)^2 + 1 \quad (\text{A.15})$$

$$a_{22} = \left(\frac{x_{12}}{a}\right)^2 + \frac{1}{2} \left(\frac{x_{13}}{a}\right)^2 + 1 \quad (\text{A.16})$$

$$a_{12} = a_{21} = \frac{x_{12}}{a} + \frac{x_{21}}{a} + \frac{1}{2} \frac{x_{13}x_{23}}{a^2} \quad (\text{A.17})$$

$$Q = \left(\left(\frac{x_{12}}{a}\right)^2 + \frac{1}{2} \left(\frac{x_{13}}{a}\right)^2 + 1\right) \left(\left(\frac{x_{21}}{a}\right)^2 + \frac{1}{2} \left(\frac{x_{23}}{a}\right)^2 + 1\right) - \left(\frac{x_{12}}{a} + \frac{x_{21}}{a} + \frac{1}{2} \frac{x_{13}x_{23}}{a^2}\right)^2 \quad (\text{A.18})$$

$$b_1 = \left(\frac{x_{12}}{a}\right)^2 + \frac{1}{2} \left(\frac{x_{13}}{a}\right)^2 - \frac{1}{2} \frac{x_{13}x_{23}}{a^2} - \frac{x_{21}}{a} \quad (\text{A.19})$$

$$b_2 = \left(\frac{x_{21}}{a}\right)^2 + \frac{1}{2} \left(\frac{x_{23}}{a}\right)^2 - \frac{1}{2} \frac{x_{13}x_{23}}{a^2} - \frac{x_{12}}{a} \quad (\text{A.20})$$

After calculation of  $\hat{X}_1$  and  $\hat{X}_2$  by means of (A.14) one can calculate  $\hat{X}_3$  with (A.12).

Appendix B

In this appendix expressions are derived for the estimates  $\hat{\vec{v}}$  and  $\hat{\mathbf{F}}$  by means of variation of the scalar function J, defined by (3.3.20), with respect to the vector  $\vec{v}$  and the tensor F respectively.

Expression (3.3.20) can easily be rewritten to

$$J = \frac{1}{n} \sum_{i=1}^n (\Delta \vec{x}_{1i} \cdot \Delta \vec{x}_{1i} - 2\mathbf{F} : \Delta \vec{x}_{0i} \Delta \vec{x}_{1i} - 2\Delta \vec{x}_{1i} \cdot \vec{v} + 2\mathbf{F} : \Delta \vec{x}_{0i} \vec{v} + \mathbf{F}^c \cdot \mathbf{F} : \Delta \vec{x}_{0i} \Delta \vec{x}_{0i} + \vec{v} \cdot \vec{v}) \quad (\text{B.1})$$

Variation of J with respect to  $\vec{v}$  yields:

$$\delta J_{\vec{v}} = \frac{1}{n} \sum_{i=1}^n (-2\Delta \vec{x}_{1i} + 2\mathbf{F} \cdot \Delta \vec{x}_{0i} + 2\vec{v}) \cdot \delta \vec{v} \quad (\text{B.2})$$

Introducing the mean vectors:

$$\Delta \vec{x}_0 = \frac{1}{n} \sum_{i=1}^n \Delta \vec{x}_{0i} \quad (\text{B.3})$$

$$\Delta \vec{x}_1 = \frac{1}{n} \sum_{i=1}^n \Delta \vec{x}_{1i} \quad (\text{B.4})$$

and the requirement  $\delta J_{\vec{v}} = 0$  for each  $\delta \vec{v}$  we obtain:

$$\hat{\vec{v}} = \Delta \vec{x}_1 - \hat{\mathbf{F}} \cdot \Delta \vec{x}_0 \quad (\text{B.5})$$

Variation of J with respect to F yields:

$$\delta J_{\mathbf{F}} = \frac{1}{n} \sum_{i=1}^n (-2\Delta \vec{x}_{0i} \Delta \vec{x}_{1i} + 2\Delta \vec{x}_{0i} \vec{v} + 2\mathbf{F} \cdot \Delta \vec{x}_{0i} \Delta \vec{x}_{0i}) : \delta \mathbf{F} \quad (\text{B.6})$$

Substitution of (B.5) into (B.6) and requiring  $\delta J_{\mathbf{F}} = 0$  for each  $\delta \mathbf{F}$  gives after some manipulations:

$$\frac{1}{n} \sum_{i=1}^n (\Delta \vec{x}_{0i} \Delta \vec{x}_{1i} - \Delta \vec{x}_0 \Delta \vec{x}_1 - \Delta \vec{x}_0 \Delta \vec{x}_0 \cdot \hat{\mathbf{F}}^c + \frac{1}{n} \sum_{i=1}^n \Delta \vec{x}_{0i} \Delta \vec{x}_{0i} \cdot \hat{\mathbf{F}}^c) = 0 \quad (\text{B.7})$$

With the distribution tensors

$$X_{00} = \frac{1}{n} \sum_{i=1}^n \Delta \vec{x}_{0i} \Delta \vec{x}_{0i} - \Delta \vec{x}_0 \Delta \vec{x}_0 \quad (\text{B.8})$$

$$X_{01} = \frac{1}{n} \sum_{i=1}^n \Delta \vec{x}_{0i} \Delta \vec{x}_{1i} - \Delta \vec{x}_0 \Delta \vec{x}_1 \quad (\text{B.9})$$

(B.7) can be written as:

$$\hat{\mathbf{F}} \cdot X_{00} = X_{01}^c \quad (\text{B.10})$$

## B.2

As for all practical 3-D situations  $X_{00}$  is positive definite and thus a regular tensor we may write:

$$\hat{F} = X_{01}^c \cdot X_{00}^{-1} \quad (\text{B.11})$$

A special case is the strain distribution on curved outer surfaces which is essentially a 2-D problem described in 3-D object space. This is the subject of section 3.3.2.

Appendix C

In this appendix a relation between systematic errors in the image plane coordinates and deviations of the desired image plane position and orientation is derived. This relation will be expressed in terms of the regarded image plane coordinates itself.

First equation (3.2.1) is written in a shorthand notation as:

$$\underline{x}_N = R \cdot \underline{X}_N \quad (C.1)$$

where:

$$\underline{x}_N = \frac{\underline{x} - \underline{x}_0}{\|\underline{x} - \underline{x}_0\|} \quad (C.2)$$

$$\underline{X}_N = \frac{\underline{X} - \underline{X}_0}{\|\underline{X} - \underline{X}_0\|} \quad (C.3)$$

Consider the transformation described by (C.1) and a second transformation different from the first one for which we write:

$$\underline{x}_N + \delta \underline{x}_N = (R + \delta R) \cdot (\underline{X}_N + \delta \underline{X}_N) \quad (C.4)$$

Suppose this second transformation differs only a little from the first one, i.e. for a certain norm it holds:

$$\|\delta \underline{x}_N\| \ll \|\underline{x}_N\| \quad (C.5)$$

$$\|\delta \underline{X}_N\| \ll \|\underline{X}_N\| \quad (C.6)$$

$$\|\delta R\| \ll \|R\| \quad (C.7)$$

than it is permitted to neglect quadratic and higher order terms in (C.4) and so, using (C.1), we may write:

$$\delta \underline{x}_N = R \cdot \delta \underline{X}_N + \delta R \cdot \underline{X}_N \quad (C.8)$$

For the chosen image plane orientations  $R = I$  and so from (C.1) it follows that  $\underline{x}_N = \underline{X}_N$ . With this (C.8) changes to:

$$\delta \underline{x}_N = \delta \underline{X}_N + \delta R \cdot \underline{X}_N \quad (C.9)$$

The different terms of (C.9) are considered separately. The left term of (C.9) is first expressed in  $\delta \underline{x}$ , the difference between the image plane vectors of the two close transformation. For that purpose we expand (C.2) in a Taylor series around  $\underline{x}$  and  $\underline{x}_0$  whereby, taking into account (C.5), the quadratic and higher order terms are neglected:



$$\delta \underline{x}_N = \frac{\partial \underline{x}_N}{\partial \underline{x}} \cdot \delta \underline{x} + \frac{\partial \underline{x}_N}{\partial \underline{x}_0} \cdot \delta \underline{x}_0 \quad (C.10)$$

which, after a straight forward calculation, may be rewritten to:

$$\delta \underline{x}_N = \frac{1}{\|\underline{x} - \underline{x}_0\|} (\mathbf{I} - \underline{x}_N \underline{x}_N) \cdot (\delta \underline{x} - \delta \underline{x}_0) \quad (C.11)$$

In a similar way one can derive for  $\delta \underline{x}_N$ , noting that  $\delta \underline{x} = \underline{0}$ :

$$\delta \underline{x}_N = - \frac{1}{\|\underline{x} - \underline{x}_0\|} (\mathbf{I} - \underline{x}_N \underline{x}_N) \cdot (\delta \underline{x}_0) \quad (C.12)$$

The expression of (C.12) in terms of  $\underline{x}$  comes up for discussion at a later stage where this can be done much easier. For working-out the second term of the right-part of (C.9) it is first noted that for each proper orthonormal transformation tensor R we may write

$$R^c \cdot R = \mathbf{I} \quad (C.13)$$

and thus, also:

$$(R + \delta R)^c \cdot (R + \delta R) = \mathbf{I} \quad (C.14)$$

Taking into account (C.7), and therefore neglecting quadratic terms one can easily derive:

$$\delta R = - \delta R^c \quad (C.15)$$

and so  $\delta R$  is a skew-symmetric. Hence there exists a vector  $\delta \vec{\omega}$ , the so-called axial vector of  $\delta R$ , such that for each vector  $\vec{v}$  holds:

$$\delta R \cdot \underline{v} = \delta \omega * \underline{v} \quad (C.16)$$

The components  $\delta \omega_i$ ;  $i \in \{1, 2, 3\}$ , are small rotations around the corresponding base vectors  $\vec{e}_i$ . Substitution of (C.11), (C.12) and (C.16) into (C.9) yields:

$$\begin{aligned} (\mathbf{I} - \underline{x}_N \underline{x}_N) \cdot \delta \underline{x} &= (\mathbf{I} - \underline{x}_N \underline{x}_N) \cdot \delta \underline{x}_0 + \\ &- \frac{\|\underline{x} - \underline{x}_0\|}{\|\underline{x} - \underline{x}_0\|} (\mathbf{I} - \underline{x}_N \underline{x}_N) \cdot \delta \underline{x}_0 - \|\underline{x} - \underline{x}_0\| \underline{x}_N * \delta \omega \end{aligned} \quad (C.17)$$

Using  $R = \mathbf{I}$ ,  $\underline{x}_N = \underline{x}_N$  and from (3.2.6):

$$\frac{\|\underline{x} - \underline{x}_0\|}{\|\underline{x} - \underline{x}_0\|} = \frac{c}{X_j + a} \quad (C.18)$$

(C.17) can be rewritten to:

$$(I - \mathbf{x}_N \mathbf{x}_N^T) \cdot \delta \mathbf{x} = (I - \mathbf{x}_N \mathbf{x}_N^T) \cdot \left( \delta \mathbf{x}_0 \frac{c}{X_j + a} - \delta X_0 \right) - \mathbf{x} * \delta \omega \quad (C.19)$$

Remembering that the component  $x_j$ , corresponding to the base vector  $\vec{e}_j$ , which is perpendicular to the image plane has a constant value (the camera constant  $c$ ) it follows that  $\delta x_j = 0$ . Here we choose  $\vec{e}_3$  as the concerning base vector. The relations which are derived hereafter are direct applicable to the two image planes defined in (3.2.8) section 3.2.2 by substitution of the corresponding indices. It follows from (C.19) that:

$$\begin{aligned} & \begin{bmatrix} (x_2^2 + x_3^2) - x_1 x_2 \\ -x_1 x_2 & (x_1^2 + x_3^2) \end{bmatrix} \cdot \begin{bmatrix} \delta x_1 \\ \delta x_2 \end{bmatrix} = \\ & \begin{bmatrix} (x_2^2 + x_3^2) - x_1 x_2 & -x_1 x_3 \\ -x_1 x_2 & (x_1^2 + x_3^2) - x_2 x_3 \end{bmatrix} \cdot \begin{bmatrix} \delta x_{01} \\ \delta x_{02} \\ \delta x_{03} \end{bmatrix} - \frac{c}{X_3 + a} \begin{bmatrix} \delta X_{01} \\ \delta X_{02} \\ \delta X_{03} \end{bmatrix} + \\ & - (x_1^2 + x_2^2 + x_3^2) \begin{bmatrix} 0 & -x_3 & x_2 \\ x_3 & 0 & -x_1 \end{bmatrix} \cdot \begin{bmatrix} \delta \omega_1 \\ \delta \omega_2 \\ \delta \omega_3 \end{bmatrix} \quad (C.20) \end{aligned}$$

After a straightforward calculation, and using  $x_3 = c$ , this can be rewritten to:

$$\begin{bmatrix} \delta x_1 \\ \delta x_2 \end{bmatrix} = \begin{bmatrix} 1 & 0 & -\frac{x_1}{c} - \frac{c}{\bar{x}_3 + a} & 0 & \frac{x_1}{\bar{x}_3 + a} \\ 0 & 1 & -\frac{x_2}{c} & 0 & -\frac{c}{\bar{x}_3 + a} \frac{x_2}{\bar{x}_3 + a} \end{bmatrix}$$

$$\begin{bmatrix} \frac{x_1 x_2}{c} - c(1 + (\frac{x_1}{c})^2) & x_2 \\ c(1 + (\frac{x_2}{c})^2) & -\frac{x_1 x_2}{c} - x_1 \end{bmatrix} \begin{bmatrix} \delta x_{01} \\ \delta x_{02} \\ \delta x_{03} \\ \delta X_{01} \\ \delta X_{02} \\ \delta X_{03} \\ \delta \omega_1 \\ \delta \omega_2 \\ \delta \omega_3 \end{bmatrix} \quad (C.21)$$

Expression (C.21) is the desired relation between the position and orientation deviations and the resulting systematic errors in the image plane coordinates. It is simple to rewrite (C.21) in a form for which the image plane coordinate errors are polynomial functions of the image plane coordinates itself:

$$\begin{bmatrix} \delta x_1 \\ \delta x_2 \end{bmatrix} = \begin{bmatrix} \delta x_{01} - \frac{c}{\bar{x}_3 + a} \delta X_{01} - c \delta \omega_2 \\ \delta x_{02} - \frac{c}{\bar{x}_3 + a} \delta X_{02} + c \delta \omega_1 \end{bmatrix} +$$

$$\begin{bmatrix} -\frac{1}{c} \delta x_{03} + \frac{1}{\bar{x}_3 + a} \delta X_{03} & \delta \omega_3 & \frac{1}{c} \delta \omega_1 & -\frac{1}{c} \delta \omega_2 & 0 \\ -\delta \omega_3 & -\frac{1}{c} \delta x_{03} + \frac{1}{\bar{x}_3 + a} \delta X_{03} & \frac{1}{c} \delta \omega_2 & 0 & \frac{1}{c} \delta \omega_1 \end{bmatrix} \begin{bmatrix} x_1 \\ x_2 \\ x_1^2 \\ x_2^2 \end{bmatrix} \quad (C.22)$$

Appendix D

In this appendix the influence of focusing on another than the control plane is investigated.

In fig. D1 the two situations whereby once the camera is focussed on the control plane and once on an arbitrary plane behind the controlplane. The distances between the two centres of projection  $O$  and  $O'$  and the planes of focussing are denoted as  $X_0$  and  $X'_0$  respectively. In the ideal case  $a=X_0$ .

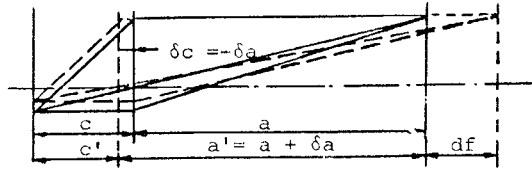


Fig. D1. Two situations whereby once the image is focussed on the control plane (—) and once on an arbitrary different plane (---).

By focusing on another than the control plane the centre of projection is shifted with respect to the image plane; hence the camera constant  $c$  changes. From fig. D1. it is immediately seen that:

$$\delta a = -\delta c = c' - c \quad (D.1)$$

Further, from the lens formula it follows:

$$X_0 = \left(\frac{1}{f} - \frac{1}{c}\right)^{-1} \quad (D.2)$$

and a first-order approach for  $\delta X_0$  can be derived from (D.2):

$$\delta X_0 = -\left(\frac{c}{f} - 1\right)^{-2} \delta c \quad (D.3)$$

With  $\delta X_0 = \delta c + d_f$  it follows from (D.1) and (D.3):

$$\delta a = \frac{\left(\frac{c}{f} - 1\right)^2}{1 + \left(\frac{c}{f} - 1\right)^2} d_f \quad (D.4)$$

which for  $c/f \approx 1$  may be rewritten as:

$$\delta a = \left(\frac{c}{f} - 1\right)^2 d_f \quad (D.5)$$

Appendix E

In this appendix an expression is derived for the unexplained variation  $V_u$  in terms of the marker distribution tensors  $X_{00}$  and  $X_{11}$  and the estimated deformation gradient tensor  $F$ .

The unexplained variation is defined as (3.5.18):

$$V_u = \sum_{i=1}^n (\Delta \vec{x}_{1i} - \hat{\Delta \vec{x}}_{1i}) \cdot (\Delta \vec{x}_{1i} - \hat{\Delta \vec{x}}_{1i}) \quad (E.1)$$

which is easily rewritten to:

$$\frac{1}{n} V_u = \frac{1}{n} \sum_{i=1}^n \Delta \vec{x}_{1i} \cdot \Delta \vec{x}_{1i} - 2 \frac{1}{n} \sum_{i=1}^n \Delta \vec{x}_{1i} \cdot \hat{\Delta \vec{x}}_{1i} + \frac{1}{n} \sum_{i=1}^n \hat{\Delta \vec{x}}_{1i} \cdot \hat{\Delta \vec{x}}_{1i} \quad (E.2)$$

With  $\hat{\Delta \vec{x}}_{1i} = \hat{F} \cdot \Delta \vec{x}_{0i} + \hat{\vec{v}}$  it follows for the second term on the right hand side of (E.2):

$$\frac{1}{n} \sum_{i=1}^n \Delta \vec{x}_{1i} \cdot \hat{\Delta \vec{x}}_{1i} = \hat{F} : \frac{1}{n} \sum_{i=1}^n \Delta \vec{x}_{0i} \Delta \vec{x}_{1i} + \Delta \vec{x}_1 \cdot \hat{\vec{v}} \quad (E.3)$$

and substitution of  $\hat{\vec{v}} = \Delta \vec{x}_1 - \hat{F} \cdot \Delta \vec{x}_0$  (3.3.21) yields:

$$\begin{aligned} \frac{1}{n} \sum_{i=1}^n \Delta \vec{x}_{1i} \cdot \hat{\Delta \vec{x}}_{1i} &= \hat{F} : X_{01} + \Delta \vec{x}_1 \cdot \Delta \vec{x}_1 \\ &= \hat{F}^c \cdot \hat{F} \cdot \hat{F}^{-1} \cdot X_{01}^c + \Delta \vec{x}_1 \cdot \Delta \vec{x}_1 \\ &= \hat{F}^c \cdot \hat{F} : X_{00} + \Delta \vec{x}_1 \cdot \Delta \vec{x}_1 \end{aligned} \quad (E.4)$$

The third term on the right hand side of (E.2), with  $\hat{\Delta \vec{x}}_{1i} = \hat{F} \cdot \Delta \vec{x}_{0i} + \hat{\vec{v}}$  yields:

$$\frac{1}{n} \sum_{i=1}^n \hat{\Delta \vec{x}}_{1i} \cdot \hat{\Delta \vec{x}}_{1i} = \hat{F}^c \cdot \hat{F} : \frac{1}{n} \sum_{i=1}^n \Delta \vec{x}_{0i} \Delta \vec{x}_{0i} + 2 \hat{F} : \Delta \vec{x}_0 \hat{\vec{v}} + \hat{\vec{v}} \cdot \hat{\vec{v}} \quad (E.5)$$

Substitution of  $\hat{\vec{v}} = \Delta \vec{x}_1 - \hat{F} \cdot \Delta \vec{x}_0$  into (E.5) yields:

$$\frac{1}{n} \sum_{i=1}^n \hat{\Delta \vec{x}}_{1i} \cdot \hat{\Delta \vec{x}}_{1i} = \hat{F}^c \cdot \hat{F} : X_{00} + \Delta \vec{x}_1 \cdot \Delta \vec{x}_1 \quad (E.6)$$

With (E.4), (E.6) we finally obtain for the unexplained variation (E.1):

$$\frac{1}{n} V_u = \frac{1}{n} \sum_{i=1}^n \Delta \vec{x}_{1i} \cdot \Delta \vec{x}_{1i} - \Delta \vec{x}_1 \cdot \Delta \vec{x}_1 - \hat{F}^c \cdot \hat{F} : X_{00} \quad (E.7)$$

With:

$$X_{11} = \frac{1}{n} \sum_{i=1}^n \Delta \vec{x}_{1i} \Delta \vec{x}_{1i} - \Delta \vec{x}_1 \Delta \vec{x}_1 \quad (E.8)$$

E.2

(E.8) is rewritten to:

$$V_u = n(I: X_{11} - \hat{F}^c \cdot \hat{F}: X_{00}) \quad (\text{E.9})$$

Appendix F

In this appendix the variance-covariance tensor  ${}^4C$  of  $\hat{F}$  is expressed in terms of the measured marker data.

The definition of  ${}^4C$  is given by (3.5.22):

$${}^4C = E[(\hat{F}^C - F^C)(\hat{F} - F)] \quad (F.1)$$

With:

$$\hat{F} = \bar{x}_{01}^C \cdot x_{00}^{-1} \quad (F.2)$$

$$\bar{x}_{01} = \frac{1}{n} \sum_{i=1}^n \Delta \vec{x}_{0i} \Delta \vec{x}_{1i} - \Delta \vec{x}_0 \Delta \vec{x}_1 \quad (F.3)$$

$$\Delta \vec{x}_{1i} = F \cdot \Delta \vec{x}_{0i} + \vec{v} + \vec{u}_i \quad (F.4)$$

it follows

$$\hat{F} = F + \left( \frac{1}{n} \sum_{i=1}^n \Delta \vec{x}_{0i} \vec{u}_i - \frac{1}{n} \sum_{i=1}^n \Delta \vec{x}_0 \vec{u}_i \right) \cdot x_{00}^{-1} \quad (F.5)$$

Substitution of (F.5) in to (F.1) gives:

$$\begin{aligned} {}^4C = x_{00}^{-1} \cdot & \left[ \frac{1}{n^2} \sum_{i=1}^n \sum_{j=1}^n \Delta \vec{x}_{0i} E(\vec{u}_i \vec{u}_j) \Delta \vec{x}_{0j} \right) + \\ & \frac{1}{n^2} \sum_{i=1}^n \sum_{j=1}^n (\Delta \vec{x}_{0i} E(\vec{u}_i \vec{u}_j) \Delta \vec{x}_0) + \\ & \frac{1}{n^2} \sum_{i=1}^n \sum_{j=1}^n (\Delta \vec{x}_0 E(\vec{u}_i \vec{u}_j) \Delta \vec{x}_{0j}) + \\ & \left. \frac{1}{n^2} \sum_{i=1}^n \sum_{j=1}^n (\Delta \vec{x}_0 E(\vec{u}_i \vec{u}_j) \Delta \vec{x}_0) \right] \cdot x_{00}^{-1} \quad (F.6) \end{aligned}$$

And with the aid of (3.3.17):

$$E(\vec{u}_i \vec{u}_j) = \delta_{ij} \sigma^2 I \quad (F.7)$$

(F.6) is easily rewritten to:

$${}^4C = \frac{\sigma^2}{n} x_{00}^{-1} \cdot \left( \frac{1}{n} \sum_{i=1}^n \Delta \vec{x}_{0i} I \Delta \vec{x}_{0i} - \Delta \vec{x}_0 I \Delta \vec{x}_0 \right) \cdot x_{00}^{-1} \quad (F.8)$$

Appendix G

In this appendix an approximation of the variance-covariance tensor  ${}^4L$  of  $\hat{\mathbf{E}}$  is derived and expressed in its components.

The variance-covariance tensor  ${}^4L$  is defined by (3.5.34):

$${}^4L = E[(\hat{\mathbf{E}} - \mathbf{E})(\hat{\mathbf{E}} - \mathbf{E})] \quad (\text{G.1})$$

With

$$\hat{\mathbf{E}} = \frac{1}{2}(\hat{\mathbf{F}}^c \cdot \hat{\mathbf{F}} - \mathbf{I}) \quad (\text{G.2})$$

one can easily obtain:

$${}^4L = \frac{1}{4} E[(\hat{\mathbf{F}}^c \cdot \hat{\mathbf{F}} - \mathbf{F}^c \cdot \mathbf{F})(\hat{\mathbf{F}}^c \cdot \hat{\mathbf{F}} - \mathbf{F}^c \cdot \mathbf{F})] \quad (\text{G.3})$$

Using (F.5) and the shorthand notation:

$$\bar{\mathbf{A}} = \frac{1}{n} \sum_{i=1}^n \Delta \vec{x}_{0i} \vec{u}_i - \frac{1}{n} \sum_{i=1}^n \Delta \vec{x}_{0i} \vec{u}_i \quad (\text{G.4})$$

it follows that:

$$\begin{aligned} \hat{\mathbf{F}}^c \cdot \hat{\mathbf{F}} &= \mathbf{F}^c \cdot \mathbf{F} + \mathbf{F}^c \cdot \bar{\mathbf{A}}^c \cdot \mathbf{X}_{00}^{-1} + \\ &\quad \mathbf{X}_{00}^{-1} \cdot \bar{\mathbf{A}} \cdot \mathbf{F} + \mathbf{X}_{00}^{-1} \cdot \bar{\mathbf{A}}^c \cdot \bar{\mathbf{A}} \cdot \mathbf{X}_{00}^{-1} \end{aligned} \quad (\text{G.5})$$

With (G.5), and neglecting higher order terms of  $\bar{\mathbf{A}}$ , expression (G.3) is rewritten to:

$$\begin{aligned} {}^4L &= \frac{1}{4} E[ (\mathbf{F}^c \cdot \bar{\mathbf{A}}^c \cdot \mathbf{X}_{00}^{-1})(\mathbf{F}^c \cdot \bar{\mathbf{A}}^c \cdot \mathbf{X}_{00}^{-1}) + \\ &\quad + (\mathbf{F}^c \cdot \bar{\mathbf{A}}^c \cdot \mathbf{X}_{00}^{-1})(\mathbf{X}_{00}^{-1} \cdot \bar{\mathbf{A}} \cdot \mathbf{F}) + \\ &\quad + (\mathbf{X}_{00}^{-1} \cdot \bar{\mathbf{A}} \cdot \mathbf{F})(\mathbf{F}^c \cdot \bar{\mathbf{A}}^c \cdot \mathbf{X}_{00}^{-1}) + \\ &\quad + (\mathbf{X}_{00}^{-1} \cdot \bar{\mathbf{A}} \cdot \mathbf{F})(\mathbf{X}_{00}^{-1} \cdot \bar{\mathbf{A}} \cdot \mathbf{F}) ] \end{aligned} \quad (\text{G.6})$$

Writing out the first term of (G.6) with the aid of (G.4) gives:

$$\begin{aligned} E[(\mathbf{F}^c \cdot \bar{\mathbf{A}}^c \cdot \mathbf{X}_{00}^{-1})(\mathbf{F}^c \cdot \bar{\mathbf{A}}^c \cdot \mathbf{X}_{00}^{-1})] &= \\ E[\frac{1}{n^2} (\mathbf{F}^c \cdot (\sum_{i=1}^n \vec{u}_i \Delta \vec{x}_{0i}) \cdot \mathbf{X}_{00}^{-1} \mathbf{F}^c \cdot (\sum_{j=1}^n \vec{u}_j \Delta \vec{x}_{0j}) \cdot \mathbf{X}_{00}^{-1} - \\ &\quad + \mathbf{F}^c \cdot (\sum_{i=1}^n \vec{u}_i \Delta \vec{x}_{0i}) \cdot \mathbf{X}_{00}^{-1} \mathbf{F}^c \cdot (\sum_{j=1}^n \vec{u}_j \Delta \vec{x}_{0j}) \cdot \mathbf{X}_{00}^{-1} - \\ &\quad + \mathbf{F}^c \cdot (\sum_{i=1}^n \vec{u}_i \Delta \vec{x}_{0i}) \cdot \mathbf{X}_{00}^{-1} \mathbf{F}^c \cdot (\sum_{j=1}^n \vec{u}_j \Delta \vec{x}_{0j}) \cdot \mathbf{X}_{00}^{-1} + \end{aligned}$$



$$+ F^C \cdot \left( \sum_{i=1}^n \vec{u}_i \Delta \vec{x}_0 \right) \cdot X_{00}^{-1} F^C \cdot \left( \sum_{j=1}^n \vec{u}_j \Delta \vec{x}_0 \right) \cdot X_{00}^{-1} \quad (G.7)$$

The components of the first term of (G.7) with respect to an orthogonal base  $\vec{e}_i$ ;  $i \in \{1, 2, 3\}$  can be obtained using the definition:

$$B_{klmn} = \langle \langle \langle \langle {}^4B \cdot \vec{e}_n \rangle \cdot \vec{e}_m \rangle \cdot \vec{e}_l \rangle \cdot \vec{e}_k \rangle \quad (G.8)$$

Where  ${}^4B$  is an arbitrary fourth-order tensor.  
It follows:

$$\begin{aligned} E \left[ \frac{1}{n^2} \langle F^C \cdot \left( \sum_{i=1}^n \vec{u}_i \Delta \vec{x}_{0i} \right) \cdot X_{00}^{-1} F^C \cdot \left( \sum_{j=1}^n \vec{u}_j \Delta \vec{x}_{0j} \right) \cdot X_{00}^{-1} \rangle_{klmn} \right] = \\ E \left[ \frac{1}{n^2} \langle F_{pk} F_{qm} \langle X_{00}^{-1} \rangle_{r1} \langle X_{00}^{-1} \rangle_{sn} \sum_{i=1}^n \sum_{j=1}^n \langle \Delta x_{0i} \rangle_s \langle \vec{u}_i \rangle_p \langle \vec{u}_j \rangle_q \rangle \right] \quad (G.9) \end{aligned}$$

Writing (3.3.17) as:

$$E \langle \langle \vec{u}_i \vec{u}_j \rangle \rangle = \delta_{ij} \sigma^2 \sum_{k=1}^3 \vec{e}_k \vec{e}_k \quad (G.10)$$

it follows for the components

$$E \langle \langle \langle \vec{u}_i \vec{u}_j \rangle_{pq} \rangle \rangle = \delta_{ij} \delta_{pq} \sigma^2 \quad (G.11)$$

Using (G.11), (G.9) is rewritten to

$$\begin{aligned} E \left[ \frac{1}{n^2} \langle F^C \cdot \left( \sum_{i=1}^n \vec{u}_i \Delta \vec{x}_{0i} \right) \cdot X_{00}^{-1} F^C \cdot \left( \sum_{j=1}^n \vec{u}_j \Delta \vec{x}_{0j} \right) \cdot X_{00}^{-1} \rangle_{klmn} \right] = \\ \frac{\sigma^2}{n^2} F_{pk} F_{pm} \langle X_{00}^{-1} \rangle_{r1} \langle X_{00}^{-1} \rangle_{sn} \sum_{i=1}^n \sum_{j=1}^n \langle \Delta x_{0i} \rangle_r \langle \Delta x_{0j} \rangle_s \quad (G.12) \end{aligned}$$

On the same way we obtain for the second term of (G.7):

$$\begin{aligned} E \left[ \frac{1}{n^2} \langle F^C \cdot \left( \sum_{i=1}^n \vec{u}_i \Delta \vec{x}_{0i} \right) \cdot X_{00}^{-1} F^C \cdot \left( \sum_{j=1}^n \vec{u}_j \Delta \vec{x}_0 \right) \cdot X_{00}^{-1} \rangle_{klmn} \right] = \\ \frac{\sigma^2}{n^2} F_{pk} F_{pm} \langle X_{00}^{-1} \rangle_{r1} \langle X_{00}^{-1} \rangle_{sn} \langle \Delta \underline{x}_0 \rangle_r \langle \Delta \underline{x}_0 \rangle_s \quad (G.13) \end{aligned}$$

The third and fourth term of (G.7) give the same result as (G.13) and now we may write for the components of (G.7):

$$\begin{aligned} E \left[ \langle \langle \langle \langle F^C \cdot A^C \cdot X_{00}^{-1} \rangle \rangle \rangle \rangle_{klmn} \right] = \\ \frac{\sigma^2}{n} F_{pk} F_{pm} \langle X_{00}^{-1} \rangle_{r1} \langle X_{00}^{-1} \rangle_{sn} \left[ \frac{1}{n} \sum_{i=1}^n \langle \Delta x_{0i} \rangle_r \langle \Delta x_{0i} \rangle_s - \right. \\ \left. \langle \Delta \underline{x}_0 \rangle_r \langle \Delta \underline{x}_0 \rangle_s \right] \quad (G.14) \end{aligned}$$

Noting that:

$$\langle X_{00} \rangle_{rs} = \frac{1}{n} \sum_{i=1}^n \langle \Delta x_{0i} \rangle_r \langle \Delta x_0 \rangle_s - \langle \Delta \bar{x}_0 \rangle_r \langle \Delta \bar{x}_0 \rangle_s \quad (G.15)$$

and:

$$\langle X_{00}^{-1} \rangle_{r1} \langle X_{00} \rangle_{rs} = \delta_{1s} \quad (G.16)$$

we finally obtain:

$$\begin{aligned} E[\langle (F^c \cdot A^c \cdot X_{00}^{-1}) \rangle \langle (F^c \cdot A^c \cdot X_{00}^{-1}) \rangle_{klmn}] = \\ \frac{\sigma^2}{n} F_{pk} F_{pm} \langle X_{00}^{-1} \rangle_{ln} \end{aligned} \quad (G.17)$$

The other three terms of (G.6) are treated the same way as the first one and this yields:

$$\begin{aligned} L_{klmn} = \frac{\sigma^2}{4n} [F_{pk} F_{pm} \langle X_{00}^{-1} \rangle_{ln} + F_{pk} P_{pn} \langle X_{00}^{-1} \rangle_{ml} + \\ F_{pl} F_{pn} \langle X_{00}^{-1} \rangle_{km} + F_{pl} P_{pm} \langle X_{00}^{-1} \rangle_{kn}] \end{aligned} \quad (G.18)$$

## Appendix H

In chapter 4 the design requirements and restrictions imposed upon the set-up for the measurement of strain distributions are given. In this appendix the important properties of the set-up are quantified based on these requirements and restrictions. For this the theoretical results derived in chapter 3 are frequently used.

From the specified maximum object size (60 x 20 [mm]) and the experience from previous experiments it was concluded that a measuring volume of 70 x 50 x 50 [mm] will satisfy. The definition of the measuring volume is given in fig. H.1.

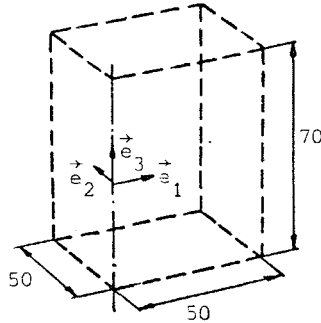


Fig. H.1 Definition of the measuring volume.

To obtain design specifications with respect to accuracy, a standard strain group is defined in chapter 4 for which a standard deviation of 0.001 for the principal strains of a 2-dimensional strainfield is required. Consider  $E_{ii}$  the components of  $E$  according to a base determined by the principle strain directions. The standard deviations  $\sigma_{E_{ii}}$  are given by (see 3.5.35)

$$\sigma_{E_{ii}}^2 = L_{iiii} = \frac{\sigma^2}{n} F_{ji} F_{ji} (X_{00}^{-1})_{ii} \quad (H.1)$$

With (see 3.3.30):

$$F_{ji} F_{ji} = 2 E_{ii} + 1 \quad (H.2)$$

and assuming that  $E_{ii} \ll 1$ , (H.2) is rewritten to:

$$\sigma_{E_{ii}}^2 = \frac{\sigma^2}{n} (X_{00}^{-1})_{ii} \quad (H.3)$$

For the standard strain group it follows from (3.3.30):

$$X_{00} = 3 I \quad (H.4)$$

## H.2

Notice that, for the standard strain group,  $X_{00}$  does not depend on the choice of the vector base. For the required standard deviation  $\sigma_{E_{ii}} = 0.001$  it is found for the scan resolution  $p$  that, using (H.3), (H.4) and (see appendix I, (I.19)):

$$p \geq \left( \frac{2 \cdot 10^6}{5.5 \cdot 8 \cdot 3} \right)^{1/3} = 25 \text{ [pix/mm]} \quad (\text{H.5})$$

Recalling the dimensions of the measuring volume, it follows that a scanning system, for discretization of the pictures, with a resolution of  $1750 \times 2500$  [pix] is needed to fulfil the required accuracy of the standard strain group.

Besides random errors, systematic errors occur. A method to correct systematic errors is described in section 3.5. How well these kind of errors are corrected depends on the number, the size and the distribution of the control markers. Based on experience from previous measurements and results reported in literature (Faig 1971, Ghosh 1975, Ferrigno and Pedotti 1985) twelve control markers for each of the two control planes, distributed as shown in fig. H.2., are chosen. Control markers are grouped on the edges of the measuring

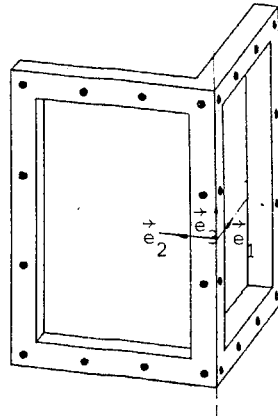


Fig. H.2. The distribution of the control markers over the two control planes.

volume because they are not allowed to be in sight of object markers. The black control markers are placed on a white frame, the control frame.

The shape functions  $N_i(\xi, \eta)$  (see 3.5.6) for this arrangement of the control markers are given by (Zienkiewicz, 1977):

$$N_i = \frac{1}{32} (1+\xi_0)(1+\eta_0)[-10 + 9(\xi^2 + \eta^2)] \quad (\text{H.6})$$

for the corner markers and as:

$$N_i = \frac{9}{32} (1+\xi_0)(1-\eta^2)(1+9\eta_0) \quad ; \quad \xi_i = \pm 1, \quad \eta_i = \pm \frac{1}{3} \quad (\text{H.7})$$

$$N_i = \frac{9}{32} (1+\eta_0)(1-\xi^2)(1+9\xi_0) \quad ; \quad \eta_i = \pm 1, \quad \xi_i = \pm \frac{1}{3} \quad (\text{H.8})$$

for the mid-side markers where  $\xi_0 = \xi$ ,  $\xi_i$ ;  $\eta_0 = \eta$ ,  $\eta_i$ .

As has been discussed already in section (3.5), page 3.38, one partial systematic error has not been corrected. This partial error is given by:

$$\delta x_{ij}^* = \frac{X_i}{a} \delta X_{0j} \quad (\text{H.9})$$

As we are dealing with strain measurement, not the real values of  $\delta x_{ij}^*$  are of interest but rather the change of the difference of these errors of neighbouring markers, that is, markers belonging to a strain group. This difference, for two markers which are labeled K and L, noted as  $\Delta_{KL}$  is given by:

$$\begin{aligned} \Delta_{KL} &= (\delta x_{ij}^*)_K - (\delta x_{ij}^*)_L \\ &= \frac{(X_i)_K - (X_i)_L}{a} \delta X_{0j} \\ &= \frac{(\Delta X_i)_{KL}}{a} \delta X_{0j} \end{aligned} \quad (\text{H.10})$$

It is immediately seen from (H.10) that a translation of the object under investigation does not change the difference  $\Delta_{KL}$  as  $(\Delta X_i)_{KL}$  does not change. For a rotation of the object  $(\Delta X_i)_{KL}$  does change. To examine the influence of this change upon the accuracy and for the establishment of the conditions by which an indicated maximum admissible error is not exceeded we look at the situation outlined in fig. H.3. Consider the two configurations  $C_0$  and  $C_1$ . Marker K keeps

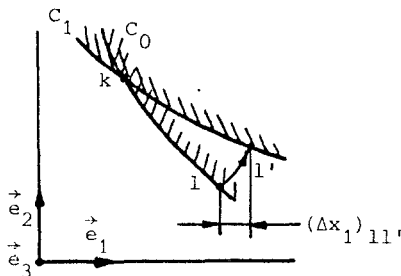


Fig. H.3. The rotation of an object as a source for systematic errors.

its position, marker L is transposed to  $L'$ . If the markers belong to the same strain group a reasonable measure for the maximum value of  $(\Delta X_i)_{LL'}$ , taking into account the dimensions of the standard strain

group (fig. 4.1.1), is 1.5 [mm]. Further, the maximum position error  $\delta X_{0j}$  is assumed to be 0.5 [mm] which is rather large.

A meaningful choice for the maximum admissible change of  $\Delta_{KL}$  should refer to the unavoidable random errors due to discretization of the pictures. For that we will base ourselves again on the already defined standard strain group. In appendix I it is derived (I.19) that the standard deviation of the measured marker centroid coordinates (the expected value of the random error due to discretization is zero) is given by:

$$\sigma_x = \left( \frac{1}{22 d p^3} \right)^{1/2} \quad (\text{H.11})$$

Requiring that:

$$\langle \Delta x_{ij}^* \rangle_{L'} - \langle \delta x_{ij}^* \rangle_L = \frac{\langle \Delta X_i \rangle_{LL'}}{a} \delta X_{0j} \leq 0.5 \sigma_x \quad (\text{H.12})$$

it follows, with  $d = 1$  [mm] and  $p = 25$  [pix/mm], for the camera distance:

$$a \geq 880 \text{ [mm]} \quad (\text{H.13})$$

Appendix I

In this appendix the random error of the position vector of the centroid of a marker due to discretization of an image is examined. The position vector of the centroid of a marker is defined by:

$$\vec{x} = \frac{1}{A_m} \int_{A_m} \vec{x} \, dA \quad (\text{I.1})$$

where  $A_m$  is the area of the marker. A marker which is divided in  $k$  strips of equal width (the width of an image line; fig. I.1) is considered.

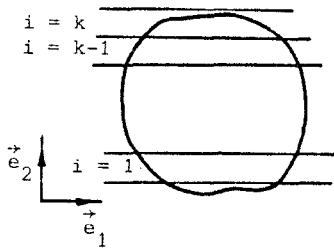


Fig. I.1 Division of a marker into strips of equal width.

A local coordinate system is chosen such that the basevector  $\vec{e}_1$  is parallel to the strips. The following is restricted to the coordinates corresponding to  $\vec{e}_1$ . The same results can be obtained with respect to the other base vector.

Each strip is replaced by a rectangular strip with the same area and centroid as the original strip (fig. I.2). The coordinates of the short sides of the rectangular strip are denoted as

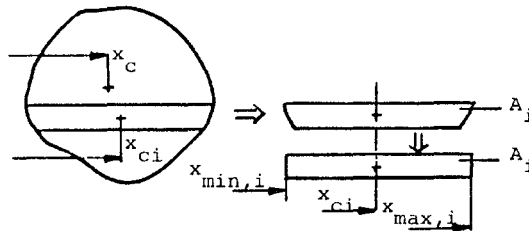


Fig. I.2 The replacement of a marker strip by a rectangular strip.

$x_{\min,i}$  and  $x_{\max,i}$ . The coordinate  $x$  of the centroid of the marker is given by:

$$x = \frac{1}{2 \sum_{i=1}^k (x_{\max,i} - x_{\min,i})} \sum_{i=1}^k (x_{\max,i}^2 - x_{\min,i}^2) \quad (\text{I.2})$$

Note that this result is still exact. If the coordinates  $x_{\max,i}$  and  $x_{\min,i}$  in (I.2) are replaced by the coordinates  $\hat{x}_{\max,i}$  and  $\hat{x}_{\min,i}$ , obtained from the discretization of the image, an estimate  $\hat{x}$  is obtained. The error  $\delta x$  defined by:

$$\delta x = \hat{x} - x \quad (\text{I.3})$$

is caused by the errors  $\delta x_{\max,i}$  and  $\delta x_{\min,i}$  which are defined by:

$$\delta x_{\max,i} = \hat{x}_{\max,i} - x_{\max,i} \quad (\text{I.4})$$

$$\delta x_{\min,i} = \hat{x}_{\min,i} - x_{\min,i} \quad (\text{I.5})$$

The coordinate  $x$  is a non-linear function of  $x_{\max}$  and  $x_{\min}$  (see (I.2)). A good approximation of the error  $\delta x$  is obtained by expansion of (I.2) as a Taylor series. Neglecting higher order terms this leads to:

$$\delta x = \sum_{i=1}^k \left( \frac{\partial x}{\partial x_{\max,i}} \delta x_{\max,i} + \frac{\partial x}{\partial x_{\min,i}} \delta x_{\min,i} \right) \quad (\text{I.6})$$

where

$$\frac{\partial x}{\partial x_{\max,i}} = \frac{x_{\max,i} - x}{\sum_{i=1}^k (x_{\max,i} - x_{\min,i})} \quad (\text{I.7})$$

$$\frac{\partial x}{\partial x_{\min,i}} = \frac{x - x_{\min,i}}{\sum_{i=1}^k (x_{\max,i} - x_{\min,i})} \quad (\text{I.8})$$

The errors  $\delta x_{\max,i}$  and  $\delta x_{\min,i}$  are random variables. It is assumed that they are uniformly distributed, which means:

$$E(\delta \bar{x}_{\max,i}) = E(\delta \bar{x}_{\min,i}) = 0 \quad (\text{I.9})$$

$$E(\delta \bar{x}_{\max,i} \delta \bar{x}_{\min,j}) = 0 \quad (\text{I.10})$$

$$E(\delta \bar{x}_{\max,i}^2) = E(\delta \bar{x}_{\min,i}^2) = \sigma_{\delta x}^2 = \frac{b^2}{12} \quad (\text{I.11})$$

where  $b$  is the width of a pixel. With these assumptions and (I.6) it is easily obtained that:



$$E(\delta\bar{x}) = 0$$

$$E(\delta\bar{x}^2) = \sigma_x^2$$

$$= \frac{\sigma_{\delta x}^2}{\left(\sum_{i=1}^k (x_{\max,i} - x_{\min,i})\right)^2} \sum_{i=1}^k [(x_{\max,i} - x)^2 + (x - x_{\min,i})^2] \quad (\text{I.12})$$

Because the true values of  $x_{\max,i}$  and  $x_{\min,i}$  are not known this estimate cannot be evaluated exactly. However, it is sufficiently accurate to evaluate the estimate by using the estimates  $\hat{x}_{\max,i}$  and  $\hat{x}_{\min,i}$  in (I.12). For almost symmetric markers it holds:

$$(x_{\max,i} - x) \approx (x - x_{\min,i}) \approx \frac{1}{2}(x_{\max,i} - x_{\min,i}) \quad (\text{I.13})$$

and thus:

$$(x_{\max,i} - x)^2 + (x - x_{\min,i})^2 \approx \frac{1}{2} (x_{\max,i} - x_{\min,i})^2 \quad (\text{I.14})$$

Using this result in (I.12) leads to:

$$\sigma_x^2 \approx \frac{\sigma_{\delta x}^2}{2 \left(\sum_{i=1}^k (x_{\max,i} - x_{\min,i})\right)^2} \sum_{i=1}^k (x_{\max,i} - x_{\min,i})^2 \quad (\text{I.15})$$

For a circular marker, existing of a large number of pixels we can write:

$$h \sum_{i=1}^k (x_{\max,i} - x_{\min,i}) \approx \frac{\pi}{4} d^2 \quad (\text{I.16})$$

and also, in a straight forward way:

$$h \sum_{i=1}^k (x_{\max,i} - x_{\min,i})^2 \approx \frac{2}{3} d^3 \quad (\text{I.17})$$

Substitution of (I.16) and (I.17) into (I.15) and using (I.11) leads to:

$$\sigma_x^2 \approx \frac{b^2 h}{22d} \quad (\text{I.18})$$

For square pixels ( $b=h$ ) (I.21) becomes

$$\sigma_x^2 = \frac{1}{22p^3 d} \quad (\text{I.19})$$

where  $p = 1/b$ , the scan resolution, is the number of pixels per millimetre. It is easily proved that (I.19) is a sufficiently accurate approximation for non-circular markers such as rectangular

and elliptical ones. Based on the central limit theorem it is assumed that  $\delta\vec{x}$  is normally distributed. As for the coordinates corresponding with  $\vec{e}_2$  (see fig. I.2) the same results can be obtained it follows for a random vector  $\delta\vec{x}_i$  given by:

$$\delta\vec{x}_i = \sum_{k=1}^2 \delta\bar{x}_{ik} \vec{e}_k \quad (\text{I.20})$$

that:

$$E(\delta\vec{x}_i) = \vec{0} \quad (\text{I.21})$$

$$E(\delta\vec{x}_i \delta\vec{x}_j) = \delta_{ij} \sigma_x^2 \mathbf{I} \quad (\text{I.22})$$

The results derived so far, are related to image plane coordinates. An approximation of the random errors in object space coordinates is derived with the aid of (3.29). From the four non-trivial equations given by (3.29) it follows:

$$\delta\bar{x}_{ij} = \frac{a}{X_i + a} \delta X_j - \frac{X_j}{(X_i + a)^2} \delta X_i \quad (\text{I.23})$$

For  $a \gg X_i, X_j$  this rewritten to:

$$\delta\bar{x}_{ij} \approx \delta X_j \quad ; \quad i \in \{1, 2\} \quad j \in \{2, 3\} \text{ or } \{1, 3\} \quad (\text{I.24})$$

which is a fairly good approximation, at least for design purposes. From (I.24) it follows that the expected value  $E(\delta X_3^2)$  is different from those of  $\delta X_1^2$  and  $\delta X_2^2$ . However, for reasons of simplicity this difference is not taking into account and it is written:

$$E(\delta\vec{X}_i \delta\vec{X}_j) = \delta_{ij} \sigma_x^2 \mathbf{I} \quad (\text{I.25})$$

Finally, the contribution of the random errors due to discretization to the variance defined by (3.3.17) and given here again:

$$E(\vec{u}_i \vec{u}_j) = \delta_{ij} \sigma^2 \mathbf{I} \quad (\text{I.26})$$

is examined. As the model error  $\vec{v}_i$  is not taken into account here it follows from (3.3.12) and (3.3.14) that:

$$\Delta\vec{x}_{1i} - F \cdot \Delta\vec{x}_{0i} = \vec{u}_1 \quad (\text{I.27})$$

With:

$$\sigma_{\Delta x}^2 = 2 \sigma_x^2 \quad (\text{I.28})$$

a straightforward calculation leads to:

$$E(\vec{u}_i \vec{u}_j) = \frac{2}{3} \text{tr}(F^C \cdot F + I) \delta_{ij} \sigma_x^2 I \quad (\text{I.29})$$

Noting that:

$$\text{tr}(F^C \cdot F + I) \approx 6 \quad (\text{I.30})$$

a good approximation for  $\sigma^2$  is given by

$$\sigma^2 = 4 \sigma_x^2 = \frac{1}{5.5 p^3 d} \quad (\text{I.31})$$



---

## SAMENVATTING

---

Om een beter inzicht te verwerven in het mechanisch gedrag van zachte biologische weefsels, in het bijzonder collageen bindweefsels, zijn gereedschappen ontwikkeld voor het meten van inhomogene spanningen en rek velden. De gereedschappen zijn gebruikt bij experimenten aan delen van de collageen bindweefselstructuur van de laterale zijde van het elleboog gewricht. Deze structuur is gekozen als onderzoeksobject omdat er een uitgebreide anatomische beschrijving van beschikbaar was.

Voor het statisch meten van spanningen is een verbeterde versie van de zogenaamde gesp (buckle transducer) gebruikt. De verbeteringen betreffen aanpassingen ten aanzien van afmetingen en vorm, de installatie-voorwaarden en de hysteresis van de weefsel-opnemer eenheid. Bovendien worden twee methoden gegeven voor het calibreren van deze krachtopnemer. Bij het ontwerp is gebruik gemaakt van een mechanisch model dat een goed inzicht geeft in het gedrag van de gesp.

Voor rekmetingen is gebruik gemaakt van een beeldverwerkingssysteem. De coördinaten van markeringspunten op het te onderzoeken object worden gereconstrueerd uit twee verschillende beelden van het object. Dit gebeurt voor verschillende deformatietoestanden. Vervolgens worden voor ieder markeringspunt schattingen voor de componenten van de deformatietensor  $F$  bepaald met behulp van de coördinaten van de markeringspunten in de directe omgeving van het beschouwde punt. Met deze schattingen worden de componenten van de Green-Lagrange rektensor  $E$  berekend.

Theoretische modellen, die de verschillende stappen van de rekmeting beschrijven, blijken van essentieel belang te zijn voor het optimaliseren van de nauwkeurigheid en voor een juiste interpretatie van de meetresultaten. Speciale aandacht is besteed aan het meten van rek velden op gekromde oppervlakken en aan de identificatie van markeringspunten in verschillende deformatietoestanden.

Verschiedende soorten metingen zijn uitgevoerd aan delen van de bindweefsel structuur. Een experiment is uitgevoerd aan de bindweefsel structuur in situ. Doel van het onderzoek was om na te gaan welke fenomenen en parameters als belangrijk moeten worden beschouwd voor de karakterisering van het mechanische gedrag. Het blijkt dat het mechanisch gedrag van het weefsel gecompliceerd is. Met de parameters die in beschouwing zijn genomen (dikte van het weefsel, de globale ligging van de collageen vezels en de randvoorwaarden) kunnen de gevonden fenomenen gedeeltelijk worden verklaard.

Bij verder onderzoek is het van het grootste belang meer gedetailleerde informatie over de ligging van de vezels te verkrijgen en de waarde van de gebruikte methode voor het meten van de lokale weefseldikte te controleren. Bovendien is voor een kwantitatieve beschrijving van het mechanisch gedrag van de onderzochte structuur en voor het vastleggen van materiaalparameters de interactie tussen experimenten en numerieke simulatie van deze experimenten van essentieel belang.

## CURRICULUM VITAE

- 3 maart 1953 Geboren te Veghel.
- 1965 - 1966 H.B.S. te Veghel.
- 1966 - 1969 L.T.S. te Veghel, afdeling fijnmetaalbewerken.
- 1969 - 1971 M.T.S. te 's Hertogenbosch, afdeling werktuigbouwkunde.
- 1971 - 1972 Voorbereidend jaar H.T.S. te 's hertogenbosch.
- 1972 - 1976 H.T.S. te 's Hertogenbosch, afdeling werktuigbouwkunde.
- 1976 - 1983 Technische Universiteit Eindhoven, faculteit  
werktuigbouwkunde.
- 1977 - 1978 Militaire dienst.
- 1983 - 1987 Wetenschappelijk assistent aan de Technische  
Universiteit Eindhoven (1<sup>e</sup> jaar) en aan de  
Rijksuniversiteit Limburg (2<sup>e</sup>- 4<sup>e</sup> jaar). Werkzaamheden,  
welke vielen binnen het kader van een  
samenwerkingsverband, werden op beide universiteiten  
uitgevoerd.
- 1987 - In dienst getreden van de Technische Universiteit  
Eindhoven

Ieder die medewerking verleende aan het werk gedurende dit onderzoek en aan de totstandkoming van dit proefschrift wordt bij deze hartelijk bedankt.



## STELLINGEN

behorende bij het proefschrift

### TOOLS FOR THE MEASUREMENT OF STRESS AND STRAIN FIELDS IN SOFT TISSUES

- 1 De noodzaak om bij het gebruik van de "buckle transducer-tissue unity" van Barry en Ahmed te preconditioneren berust op een gebrekkige analyse van de werking van het apparaat.

  - Barry, D., and Ahmed, A.M.: "Design of a modified buckle transducer for the measurement of ligament tension", J. Biomechanical engineering, vol. 108, mei 1986.
  - Dit proefschrift, hoofdstuk 2.
- 2 Experimentele bepaling van rekvelen met behulp van markeringspunten op een object vraagt om een strategie voor de keuze van de onderlinge positie van die punten. Deze strategie kan kwantitatief worden onderbouwd.

  - Dit proefschrift, hoofdstuk 4.
- 3 Het is onjuist om te spreken van de nauwkeurigheid van een rek-meetsysteem gebaseerd op beeldverwerking. Het optredende rekvel beïnvloedt de nauwkeurigheid essentieel.

  - Dit proefschrift, hoofdstuk 3 en 4.
- 4 Het achterwege laten van correcties van de meetdata voor beeldfouten en dergelijke is, bij rekmetingen met behulp van een beeldverwerkingssysteem, een belangrijke oorzaak voor de teleurstellende nauwkeurigheid die wordt bereikt.

  - Zernicke, R.F., Butter, D.L., Grood, E.S., Hefzy, M.S.: "Strain topography of human tendon and fascia", J. Biomechanical Engineering, Vol. 106, May 1984.
  - Shoemaker, P.A., Schneider, D., Lee, M.C., Fung, Y.C.: "A constitutive model for two-dimensional soft tissues and its application to experimental data. J. Biomechanics, Vol. 19, No. 9, pp 695-702, 1986.
  - Dit proefschrift, hoofdstuk 3.
- 5 Het is zinloos om de afhankelijkheid van mechanische grootheden van zaken als donorleeftijd, bewaringsmethode en dergelijke te onderzoeken wanneer die mechanische grootheden zelf niet goed kunnen worden gemeten.
- 6 Een oordeel over het belang van de optredende afschuiving in biologisch weefsel moet worden voorafgegaan door een criterium waarop deze beoordeling berust.

  - Humphrey, J.D., Vawter, D.L., Vito, R.P.: "Quantification of strains in biaxially tested soft tissues", J. Biomechanics, Vol. 20, No. 1, pp. 59-65, 1987.

- 7 Voorbeelden van constructies met composieten op basis van een stijve vezel vindt men bij de gewrichten in het menselijk lichaam. De werktuigbouwkundig ontwerper kan van de functionele analyse van deze structuren veel leren.
- Mameren van, H., Drukker, J.: "A functional anatomical basis for injuries to the ligamentum and other soft tissues around the elbow joint: transmission of tensile and compressive loads", Int. J. Sports Med., 5, pp. 88-92, supplement, 1984.
  - Dit proefschrift, hoofdstuk 1.
- 8 De bewering van Humphrey et al. is onjuist dat een proefstrookje relatief vrij van afschuiving wanneer de door hun gehanteerde correlatie coëfficiënt nagenoeg gelijk aan één is.
- Humphrey, J.D., Vawter, D.L., Vito, R.P.: "Quantification of strains in biaxially tested soft tissues", J. Biomechanics, Vol. 20, No. 1, pp. 59-65, 1987.
- 9 De vanzelfsprekendheid waarmee in de literatuur over experimenteel mechanisch onderzoek aan zachte biologische weefsels over begrippen als "spanning" en "E-modulus" wordt gesproken, is niet in overeenstemming met het ontbreken van een goede methode voor het meten van de weefseldikte. Het ontbreken van zo'n methode komt voort uit het slecht gedefinieerd zijn van de weefsel dikte.
- 10 De toenemende kwaliteit van de presentatie van meetresultaten, ten gevolge van de integratie van de computer in het meetproces, doet vaak vergeten wat de kwaliteit van de meetresultaten zelf is.
- 11 In hoge mate geautomatiseerde meetopstellingen bieden de mogelijkheid om meer aan scholing in experimenteren te doen. Een belangrijk voordeel hierbij is het kunnen simuleren en random aanbieden van allerlei praktische problemen die zich normaal voordoen tijdens het meten.
- 12 Vanwege het universele karakter zal de rol van beeldverwerkings-systemen bij experimenteel onderzoek in de toekomst steeds belangrijker worden.
- 13 De E-modulus van collageen bindweefsels zal in de toekomst toenemen.
- Butler, D.L., Grood, E.S., Noyes, F.R., Zernicke, R.F., Brackett, K.: "Effects of structure and strain measurement technique on the material properties of young human tendons and fascia", J. Biomechanics, Vol. 17, No. 8, pp. 579-596, 1984.